DIELECTRIC PROPERTIES OF JOVIAN SATELLITE ICE ANALOGS FOR SUBSURFACE RADAR EXPLORATION: A REVIEW

Elena Pettinelli[1]*, Barbara Cosciotti[1], Federico Di Paolo[1], Sebastian Emanuel Lauro[1], Elisabetta Mattei[2], Roberto Orosei[3] and Giuliano Vannaroni[1]

*Corresponding author:pettinelli@fis.uniroma3.it

1 Dipartimento di Matematica e Fisica, Università degli Studi Roma Tre, Via della Vasca Navale, 00146 Roma, Italy

2 Dipartimento di Scienze Ecologiche e Biologiche, Università della Tuscia, Largo dell'Università (snc), 01100 Viterbo, Italy

3 Istituto di Radioastronomia, Istituto Nazionale di Astrofisica (INAF), Via Piero Gobetti, 101 40129, Bologna, Italy

Accepted Article

This article has been accepted for publication and undergone full peer review but has not been through the copyediting, typesetting, pagination and proofreading process which may lead to differences between this version and the Version of Record. Please cite this article as doi: 10.1002/2014RG000463

© 2015 American Geophysical Union. All rights reserved.

ABSTRACT

The first European mission dedicated to the exploration of Jupiter and its icy moons (JUpiter ICy moons Explorer - JUICE) will be launched in 2022 and will reach its final destination in 2030. The main goals of this mission are to understand the internal structure of the icy crusts of three Galilean satellites (Europa, Ganymede and Callisto) and, ultimately, to detect Europa's subsurface ocean, which is believed to be the closest to the surface amongst those hypothesized to exist on these moons. JUICE will be equipped with the 9 MHz subsurface penetrating radar RIME (Radar for Icy Moon Exploration), which is designed to image the ice down to a depth of 9 km. A parallel mission, Europa Clipper, equipped with 9 MHz and 60 MHz radar antennas, is also currently under study by NASA. The success of these experiments strongly relies on the accurate prediction of the radar performance and on the optimal processing and interpretation of radar echoes that, in turn, depend on the dielectric properties of the materials composing the icy satellite crusts. In the present review we report a complete range of potential ice types that may occur on these icy satellites to understand how they may affect the results of the proposed missions. First we discuss the experimental results on pure and doped water ice in the framework of the Jaccard theory, highlighting the critical aspects in terms of a lack of standard laboratory procedures and inconsistency in data interpretation. We then describe the dielectric behavior of extra-terrestrial ice analogs like hydrates and icy mixtures, carbon dioxide ice and ammonia ice. Building on this review we have selected the most suitable data to compute dielectric attenuation, velocity, vertical resolution, and reflection coefficients for such icy moon environments, with the final goal being to estimate the potential capabilities of the radar missions as a function of the frequency and temperature ranges of interest for the subsurface sounders. We present the different subsurface scenarios and associated radar signal attenuation models that have been proposed so far to simulate the structure of the crust of Europa, and discuss the physical and geological nature of various dielectric targets potentially detectable with RIME. Finally, we briefly highlight several unresolved issues that should be addressed, in near future, to improve our capability to produce realistic electromagnetic models of icy moon crusts. The present review is of interest for the geophysical exploration of all solar system bodies, including the Earth, where ice can be present at the surface or at relatively shallow depths.

Accepted Article

© 2015 American Geophysical Union. All rights reserved.

Key Points:

- not all terrestrial water ices are representative of solar system ices
- dielectric measurements of extraterrestrial ice analogs are challenging
- ice types on Jovian icy satellites will influence radar penetration depth

Index terms: 3914, 6218, 5422, 6964, 5194

Keywords: ice dielectric properties, Jovian satellites, ground penetrating radar, terrestrial and extra-terrestrial ices, planetary exploration, radio wave propagation

Accepted Article

© 2015 American Geophysical Union. All rights reserved.

Accepted Article

I. INTRODUCTION

The exploration of the internal structure of a planet has been a formidable challenge since the early developments of pure and applied geophysics. The first attempts to apply physical concepts and measuring techniques to investigate the terrestrial subsurface date between the end of the 19th century and the beginning of the 20th [*Dobrin*, 1960; *Telford and Sheriff*, 1990]. A revolution in exploration geophysics started in the 1960s with the development of a new generation of high-speed digital computers. This resulted in a rapid improvement of all basic techniques (gravity, magnetic, electrical, electromagnetic and seismic) and the introduction of new ones, which consolidated the basis of modern geophysical exploration methods. The transparency of ice and snow to high frequency radio waves (MHz range) was observed in Antarctica as early as 1933 [*Waite and Schmidt*, 1962 and references therein], even though the proof of such physical phenomenon was given in the 1950s when U.S. Air Force pilots, landing on the Greenland Ice Sheets, systematically reported errors in aircraft altitude estimated by radar altimetry. This accidental observation led *Waite and Schmidt* [1962] to demonstrate that a radar altimeter (the SCR 718 operating at 440 MHz) could measure the thickness of the polar glaciers, thus starting the era of Radio Echo Sounding (RES) [*Annan*, 2002]. A few years earlier, *El Said* [1956] had attempted to determine the depth to the water table in a desert soil using the interference between direct air-transmitted signals and signals reflected from the top of the water table, showing that radio waves can also penetrate dry geological materials. It is now known that the radio wave absorption characteristics of ice and dry sand are more the exception than the rule, as the presence of water (especially when rich in electrolytes) in rock and soil pores can greatly enhance radio wave absorption [*Stillman and Grimm*, 2011].

On Earth, deep penetration of high frequency radio waves, i.e., on the order of a few km, has been extensively reported only through the Greenland and Antarctic ice sheets [e.g., *Gudmandsen, 1971; Dowdeswell and Evans*, 2004; *Siegert et al*., 2005]. Similarly, dry and cold geological materials forming the outer shells of rocky and icy planets (and satellites) are also favorable environments for deep radio wave propagation, as first shown by the dielectric measurements performed on lunar rock and soil samples collected during the Apollo program [*Strangway et al.*, 1969]. Moreover, early studies on subsurface radio wave propagation

© 2015 American Geophysical Union. All rights reserved.

determined that this technique could be implemented to image buried geological structures without requiring a physical contact between antenna and soil. Thus, Ground Penetrating Radar (GPR) became a suitable geophysical technique for planetary exploration.

Two different experiments involving subsurface radio wave propagation were tested during the Apollo 17 mission: the Surface Electrical Properties (SEP) experiment onboard the Lunar Roving Vehicle [*Simmons et al*., 1973] and the Apollo Lunar Sounder Experiment (ALSE) onboard the Apollo spacecraft [*Porcello et al*., 1974]. SEP, based on the technique developed by *El Said* [1956], was devoted to examine the electrical properties of the upper portion of the lunar subsurface (about 2 km) and showed that the investigated layer behaves like a dielectric insulator. ALSE, instead, was a coherent surface penetrating radar operating at three different frequencies (5-5.5, 15-16.5 and 150-166 MHz) that imaged the bottom of various buried craters and detected several subsurface geological units, like those in Mare Crisium, up to a depth of about 1000-1400 m [*Maxwell and Phillips*, 1978]. After this first attempt, more than twenty years passed before a new planetary mission devoted to subsurface geophysical investigations was planned. In the 1990s and early 2000s, Mars became the main focus of the NASA and ESA planetary exploration programs, and several payload proposals included a GPR as the most suitable subsurface sounder [e.g., *Barbin et al*., 1995; *Ori and Ogliani*, 1996; *Okada and Ono*, 1998; *Olhoeft*, 1998; *Picardi et al*., 1999; *Berthelier et al*., 2000]. The first successful mission was the ESA spacecraft Mars Express, launched in 2003 [*Chicarro et al.*, 2004], which was equipped with a multi-frequency (1.8, 3, 4 and 5 MHz) coherent orbiting GPR known as MARSIS (Mars Advanced Radar for Subsurface and Ionosphere Sounding) [*Picardi et al*., 2005]. MARSIS, which is still in operation, has been able to penetrate almost 4 km of the martian surface in the south polar region, detecting the interface between the bottom of the polar deposits and the bedrock [*Plaut et al*., 2007] (Figure 1). In 2005 the NASA mission MRO (Mars Reconnaissance Orbiter) carried SHARAD (SHAllow RADar) [*Seu et al*., 2007], a higher frequency (20 MHz) GPR. So far this radar has produced thousands of high resolution images of the martian subsurface detecting, among other discoveries, the detailed internal stratified structures of the martian polar caps [*Phillips et al*., 2008]. In 2007 the Japan Aerospace Exploration Agency (JAXA) launched its first mission to the Moon. The spacecraft (SELENE) was equipped with a 5 MHz GPR (the Lunar Radar Sounder - LRS), which operated for 2363 hours performing extensive subsurface exploration of the lunar crust [*Ono et al*., 2010]. A surface penetrating radar was also incorporated in the ESA mission Rosetta, which was launched in 2004 and reached its final destination, Comet 67P/Churyumov-Gerasimenko, in the summer of 2014.

Accepted Article

© 2015 American Geophysical Union. All rights reserved.

CONSERT (Comet Nucleus Sounding Experiment by Radiowave Transmission) is a 90 MHz bi-static radar with the transmitter unit located on the lander (named Philae) and the receiver unit onboard the orbiting Rosetta spacecraft [*Kofman et al*., 2007]. The radar will investigate the internal structure of the comet nucleus through the measure of the time delay between transmitted and received signals. Finally, on May 2012, ESA selected the JUpiter ICy moons Explorer (JUICE) as the first large mission within its Cosmic Vision Program 2015-2025. The goal of the JUICE mission is to "perform detailed investigations of Jupiter and its system in all their inter-relations and complexity with particular emphasis on Ganymede as a planetary body and potential habitat. The investigations of the neighboring moons, Europa and Callisto, will complete a comparative picture of the Galilean moons and their potential habitability" [*Grasset et al*., 2013]. The interest in these satellites is rooted in the discoveries made during the Galileo spacecraft mission. Magnetic fields interpreted as being induced by Jupiter [*Khurana et al*., 1998; *Kivelson et al.*, 2000, 2002], surface features reminiscent of pack ice on Earth [*Greeley et al*., 2004; *Pappalardo et al*.,2004] and the results of thermal modeling of the moons' evolution [*Spohn and Schubert*, 2003], strongly support the presence of liquid water oceans below the icy crusts of these moons. For the JUICE mission, the 9 MHz GPR RIME (Radar for Icy Moon Exploration) [*Bruzzone et al*., 2011; *Bruzzone et al*., 2013] has been chosen as the main geophysical instrument to sound Ganymede, Europa and Callisto down to a depth of 9 km. The goal of this radar is to provide unique data on the geology and geophysics of the moons and possibly to detect Europa's subsurface ocean, which is deemed to be the closest to the surface [*Schmidt et al*., 2011; *Roth et al*., 2014]. A further mission to explore the jovian icy moons is currently under formulation by NASA, named Europa Clipper, which will host a subsurface sounder operating at 9 and 60 MHz [*Grima et al*., 2013; *Phillips and Pappalardo*, 2014].

The present review summarizes and discusses the dielectric properties of the materials that are hypothesized to form the Jupiter icy satellite crusts. The knowledge of these properties is fundamental to accurately predict radar performance and to correctly process and interpret radar data. To understand the dielectric behavior of exotic icy materials like those detected or expected on Europa, Ganymede and Callisto, we must start from what we know about terrestrial ices [*Kofman et al*., 2010]. Despite the difference in thermodynamic conditions and origin, the similarity between terrestrial and solar system water ice is quite remarkable; for example, water ice is mainly present in its hexagonal form (ice Ih) on both Earth and the icy Galilean moons. The literature on the dielectric behavior of laboratory-grown and natural water ice is rather extensive, going back as early as the 1930s, and the topic is still an area of

© 2015 American Geophysical Union. All rights reserved.

Accepted Article

active research today. In all these years, theoretical considerations and experimental evidence have generated various disputes; over time some controversies were resolved but others are still an open issue.

Both terrestrial and extraterrestrial ices are often contaminated by chemical impurities (acids, bases and salts) [*Dalton et al*., 2010]; the effects of some of these impurities on the dielectric behavior of water ice are known due to their abundance in terrestrial ices (e.g. $Na_2SO_4 \cdot 10H_2O$ in sea ice). However, several ices formed by other volatiles such as hydrocarbons can only exist in the outer part of the solar system; they are very difficult to reproduce in the laboratory and their dielectric properties are usually unknown. Nevertheless, this review also includes published data on the dielectric behavior of predicted ices that have been studied so far. Theoretical and experimental studies on the various types of ices represent a solid methodological basis for a more in-depth understanding of the dielectric behavior of pure and impure water and non-water ices and can be considered as a valuable guide for future work.

The paper is organized into ten sections and one appendix. Section 2 describes the composition of the upper crust of the Jupiter icy moons, integrating the information collected by the Near-Infrared Mapping Spectrometer (NIMS) onboard the Galileo probe with predictions based on models and experiments. Section 3 introduces the various types of terrestrial and non-terrestrial water ices. Section 4 is a summary of dielectric properties and radio-wave propagation parameters, including a discussion on the effect of temperature on the dielectric behavior of materials. In section 5 the dielectric properties of pure water ice are summarized, based on theoretical considerations and experimental results, and the properties of amorphous ice and the effect of anisotropy, density and dopants on crystalline ice are discussed. Section 6 summarizes the dielectric behavior of terrestrial water ices (i.e., meteoric, sea and marine ices), section 7 describes the dielectric behavior of clathrate hydrates, sulfate hydrates and icy mixtures, and section 8 discusses the dielectric properties of non-water ices like carbon dioxide and ammonia. In section 9 the literature data reviewed in the previous sections are used to compute both radio wave parameters (attenuation, velocity and vertical resolution) and subsurface properties (target reflectivity). Moreover, this section describes the various subsurface scenarios proposed so far, to simulate the structure of the crust of Europa and summarizes the relevant radar signal attenuation models. It also describes the physical and geological nature of the various dielectric targets that are potentially detectable with radar. Section 10 provides some final remarks. Finally, the appendix (section 11) describes, and highlights some of the limitations, of the techniques used to measure artificial and natural ice dielectric properties.

© 2015 American Geophysical Union. All rights reserved.

Accepted Article

II. COMPOSITION OF THE UPPER LAYERS OF THE ICY GALILEAN SATELLITES

Since the early spectroscopic measurements from Earth it has been known that the surfaces of Europa, Ganymede and Callisto are predominantly composed of water ice. The phase diagram of water ice in Figure 2 shows that their surface conditions (with a mean temperature of 110 K) favor the presence of ice Ih. At polar latitudes, i.e., below 72 K, it could transform to ice XI by proton ordering, however this type of ice has not yet been detected. Figure 2 illustrates that ice Ih could also transform to other phases as a function of pressure, although these transitions should occur at depths much larger than those expected to be sounded by RIME (about 9 km). On jovian satellites water ice can also exist in an amorphous state, as inferred by *Hansen and McCord* [2004] and experimentally confirmed by spectroscopic data [*Hansen and Mc Cord*, 2004; *Dalton et al.*, 2010]. The detailed evidence of the presence and nature of other chemical species has been obtained only recently, with the Galileo mission. Such compounds may originate within the satellite itself or be introduced by exogenic processes. Endogenic species may in turn have been in place since the original formation of the satellite, or they may have been created by chemical processing in the interior and subsequently emplaced at the surface by endogenic processes such as cryovolcanism or extensional tectonics [*Tobie et al.*, 2010].

Exogenic species include charged particles within Jupiter's magnetosphere and implanted on the surfaces of all four Galilean satellites. Additional material may be brought by comets, meteorites or micrometeorites, while Europa also receives matter ejected from Io. The exchange of surface and sub-surface material also takes place on Io and Europa, while the current internal activity of Ganymede seems to be limited and that of Callisto is practically absent [*Sohl et al.*, 2010]. The main sources of energy driving the internal activity of the Galilean moons are radiogenic heat release and, especially, the tidal forces caused by their resonating orbits. Tidal heating decreases with increasing distance from Jupiter, and thus is most important for Io and Europa, much less important for Ganymede, and unimportant for Callisto. Overall this results in unceasing volcanic activity on the innermost satellite, Io, and in an increasing ice crust thickness moving from Europa to Ganymede to Callisto. The dissipation of tidal energy heating the Galilean moons, along with radiogenic heat release, results not only in a global geological activity, but also drives the chemical processes that

© 2015 American Geophysical Union. All rights reserved.

Accepted Article

create the numerous compounds detected and mapped by recent spacecraft missions.

On Europa, spectra collected by the NIMS experiment have been interpreted as being indicative of the presence of hydrate compounds, concentrated in visually dark and reddish regions. Some authors [e.g., *McCord et al.*, 1998, 1999; *Dalton*, 2003; *Dalton et al.*, 2005] hypothesize that such material is made of hydrate salt minerals enriched in Mg and Na sulfates, formed by the crystallization of brines erupted from the subsurface ocean. Alternatively, it has been proposed that contaminants of the mostly water ice surface consist of sulfuric acid hydrate ($H_2SO_4 \cdot nH_2O$), formed by the radiolysis of water and a sulfur-bearing species, or by the decomposition of sulfate salts [*Carlson et al.*, 1999]. More recently, *Orlando et al*. [2005] and *Dalton* [2007] found a better match for europan spectra in mixtures of sulfuric acid hydrates together with hydrated salts, while *Brown and Hand* [2013] have presented evidence for epsomite ($MgSO_4 \cdot 7H_2O$) in particular. Other non-water-ice species, like CO_2 and H_2O_2, were also detected in the leading hemisphere at equatorial to mid-latitudes.

On Ganymede, the composition of the non-water-ice material ranges from heavily hydrated compounds at high latitudes, similar to those on Europa, to only slightly hydrated ones [*McCord et al.*, 2001]. Galileo data and ground-based spectra have allowed the identification of carbon dioxide, sulfur dioxide, molecular oxygen, ozone and possibly cyanogen, hydrogen sulfide and various organic species [e.g., *McCord et al.*, 1998]. The organic material could be formed in situ as a co-product of radiolysis and chemical reactions within the contaminated icy crust and/or from exogenic material falling onto Ganymede's surface. The surface composition of Callisto is thought to be broadly similar to its bulk composition, because of its less-evolved state compared to the other Galilean moons. Non-water-ice compounds include Mg- and Fe-bearing hydrated silicates, CO_2, SO_2, and possibly ammonia and various organic compounds [*Moore et al.*, 2004; *Showman and Malhotra*, 1999], with abundances greater than those reported on Ganymede and Europa.

Other chemical species are predicted to be present because of models or experiments on the formation and evolution of these satellites. These species include aliphatic hydrocarbons, heavily hydrated and/or hydroxylated minerals and tholins [*Dalton et al.*, 2010]. Table 1, adapted from *Dalton* [2010], summarizes the chemical compounds detected and expected to be present on the icy satellite surfaces.

Finally, it should be noted that several volatile chemical species (e.g., SO_2, CO_2, O_2, CH_4, H_2S, O_2) could also exist at depth as clathrate hydrates in the jovian icy crusts even though,

© 2015 American Geophysical Union. All rights reserved.

Accepted Article

due to their thermodynamic instability on the planetary surfaces, they cannot be directly detected by conventional spectroscopic techniques [see e.g., *Kargel and Lunine*, 1998; *Prieto-Ballesteros et al.*, 2005; *Hand et al.*, 2006; *Choukroun et al.*, 2013 and references therein].

III AN OVERVIEW ON TERRESTRIAL AND NON-TERRESTRIAL WATER ICE

Before discussing the dielectric properties of ice, we briefly describe the different types of water ices present on Earth or expected to exist in the icy crusts of the Galilean satellites. Extensive reviews on the topic can be found in *Schmitt et al*. [1998], *Cuffey and Paterson* [2010], *Eicken et al*. [2009], *Thomas and Dieckmann* [2009], *Singh et al*. [2011], *Bartels-Rausch et al*. [2012] and *Gudipati and Castillo-Rogez* [2013].

Laboratory-grown and ordinary natural polycrystalline ice is made of crystals or grains having a hexagonal symmetry (named ice Ih) (Figure 2, right panel). This polycrystalline structure is fully solid only when it lies a few tens of degrees below the bulk melting temperature, especially, but not exclusively, if the ice contains chemical impurities (freezing-point depression). When the ice approaches its bulk melting temperature, pre-melting liquid layers (i.e., thermodynamically stable disordered structures) start to form at crystal interfaces, creating a network of planar structures inside the polycrystalline ice [*Brox et al.*, 2015]. The planar structure between two single grains is called the grain boundary, the intersection of three grains generates a liquid vein, and where four or more grains join a liquid node is formed (for details see e.g., *Dash et al.* [2006] and *Bartels-Rausch et al.* [2012]). It has been recognized that the melting of ice, as for any other solid, starts at the grain boundaries [*Wettlaufer and Worster*, 2006].

All terrestrial ices are formed by polycrystalline hexagonal ice; they constitute various ice bodies which differ in origin, location and extension. As schematically depicted in Figure 3, ice sheets are ice masses of continental size consisting of ice and snow accumulated on land, whereas ice shelves, which are fed by the outflow from an adjacent ice sheet, float on the ocean while remaining attached to grounded ice. Extensive land-based masses of ice, covering smaller areas than those of the ice sheets, are named ice caps, and smaller ice masses constrained by topographical features are termed glaciers. On land, ice can also

© 2015 American Geophysical Union. All rights reserved.

Accepted Article

directly form on lakes and rivers. The nature of land ice (including ice shelves and icebergs) is meteoric and it forms by the metamorphic transformation of snow into solid ice [*Cuffey and Paterson*, 2010], although the presence of the ice freezing from the bottom of grounded ice sheets [e.g., *Bell et al*., 2011] or from subglacial lake water [e.g., *Bell et al*., 2002] has recently been highlighted. On the sea, natural ice is produced in two different ways (see Figure 3): i) as sea ice, which forms from freezing of seawater at the ocean surface [*Thomas and Dieckmann*, 2009], and ii) as marine ice, which forms under an ice shelf from seawater diluted with glacial melt-water [*Oerter et al.*, 1992]. Meteoric, sea and marine ice are different in terms of structure (both at the micro and macro scale) and impurity content (see below). In particular, the bulk salinity of marine ice (as low as $0.03‰$) is an order of magnitude higher than that of meteoric ice, but 2 orders of magnitude lower than that observed in granular sea ice [*Tison et al.*, 2001].

In the following, we briefly describe the structure and origin of all three types of ice for completeness, even though we are well aware that they are not fully representative of the type of water ice present in the jovian satellite crusts. Meteoric ice is a peculiarity of the terrestrial environment, where a dense and active atmosphere is present. In the Galilean icy satellites ice formation and metamorphism occurs under very different chemical-physical conditions [e.g., *Eluszkiewicz et al*., 1998], thus meteoric ice cannot be considered a realistic analog. Conversely, some authors [*Moore*, 2000; *Blankenship and Morse*, 2004] have suggested that marine ice could be a good analogue of the ice present at the ice/ocean interface on Europa, and speculations have also been made on the possible presence of shallow, partially molten salty ice, conceptually similar to sea ice, beneath the chaotic Europa terrains [*Head et al.*, 1999; *Walker and Schmidt*, 2015].

3.1 Meteoric ice

Meteoric ice is formed by the progressive densification of snow, which is a porous medium made of air, ice crystals and small amounts of chemical impurities. Such impurities travel through the atmosphere and are deposited on the ice sheet surface attached to snowflakes (wet deposition) or as independent aerosols (dry deposition). Primary aerosols, mainly continental dust (e.g., silicate minerals, $CaCO_3$, $CaSO_4$) and sea spray (Na^+, Mg^{2+}, K^+, Cl^-, Ca^{2+} and SO_4^{2-}), are transported by winds, whereas secondary aerosols (e.g., H_2SO_4) form directly in the atmosphere from gases. Moreover, the ice directly absorbs several

© 2015 American Geophysical Union. All rights reserved.

soluble atmospheric gases such as HCl, NH_3, HNO_3 and H_2O_2 (Figure 4). The presence and concentration of these impurities are site specific and fluctuate in time, as a result of the variations in atmospheric chemical composition and climate conditions at the time when the snow was deposited. An in-depth description of meteoric ice impurities and their distribution in the polar areas can be found in *Legrand and Mayewski* [1997].

The densification process, produced by gravity and snow accumulation, transforms snow into firn (compacted snow underlying fresh snow) and eventually into ice. The compaction progressively increases the firn density up to a point (about 830 kg m^{-3}) where interconnecting air- or water-filled passageways between the ice grains are sealed off, producing a polycrystalline ice which contains only individual bubbles (pore close-off). This process also affects the size of the ice crystals that get larger with time and depth [*Singh et al*., 2011]. In glacier ice, the bubbles are present usually up to a depth of 500-1000 m, and may be filled with liquid water, if the temperature is close to the melting point, or with atmospheric gases. Below this depth the high pressure starts to strongly affect bubble size, up to the point (dissociation pressure) where the gas progressively diffuses into the ice cage to form clathrate hydrates [*Miller*, 1969] and the bubbles disappear completely.

3.2 Sea ice

Sea ice genesis, formation and evolution are rather different from those of meteoric ice (for a detailed description see e.g., *Thomas and Dieckmann* [2009]). Sea ice originates as frozen ocean water and it is characterized by a multiphase structure that, in addition to hexagonal ice crystals, includes gas, liquid brines, solid salts and other impurities (mushy layer). Sea ice starts to form in supercooled water (usually in rough water conditions) where small ice crystals, known as frazil ice, develop in the form of needles, spicules or platelets. On the ocean surface the accumulation of frazil ice creates a thick congealing layer named grease ice because of its oily appearance. In shallow basins and turbulent conditions, frazil ice can also accumulate on the sea floor as anchor ice. Under wave action, frazil ice can be compressed to form so-called pancake ice, made of round pieces of ice with diameters ranging from 30 cm to 3 m, which solidifies and thickens mechanically by rafting on top of each other to form floes [*Bartels-Rausch et al.,* 2012 and literature therein]. In contrast, under calm water conditions the ice growth below the frazil ice layer is regular and the ice crystals tend to align with the *c*-axis in the horizontal plane to form a uniform columnar ice (congelation ice). In this regular and strongly anisotropic ice structure, brine inclusions are arranged as thread-like

© 2015 American Geophysical Union. All rights reserved.

Accepted Article

cells arranged in thin, vertically oriented layers. In time the brine pockets tend to migrate downward, expand into a drainage network and eventually, in much part, to flow into the underlying water column. The high salinity of sea ice (up to $12-15‰$) is due to the presence of brine inclusions, as sea ice is pure Ih ice which actively segregates the majority of the ions present in sea water. Only fluorine, chlorine and ammonium ions can be incorporated in the ice crystal in appreciable quantities (cf. section 5.5). Among the total mass of salts dissolved in sea water, Na^+ and Cl^- ions account for roughly 85%, SO_4^{2-} ions for 8% and Ca^{2+}, Mg^{2+} and K^+ for another 6%. Therefore, mirabilite ($Na_2SO_4 \cdot 10H_2O$) and hydrohalite ($NaCl \cdot 2H_2O$) are by far the most common solid salts present in sea ice. The temperature regulates the amount of liquid fraction in the ice: mirabilite starts to precipitate at -8.2°C and hydrohalite at -22.9°C. At -30°C the fraction of brine drops below 8%, however even at the lowest temperatures typically encountered in sea ice (around -40°C), a small but non-negligible liquid fraction remains [*Thomas and Dieckmann*, 2009].

3.3 Marine ice

The existence of a third type of natural ice was first observed in an ice core collected on Amery Ice Shelf (Antarctica). There, below the typical ice shelf faces constituted by snow accumulated on ice that flowed from inland, an ice was found to have a much lower $\delta^{18}O$ than glacier ice (close to ocean water value) and melt-water conductivity 100 times higher than the upper layers [*Morgan*, 1972]. The existence of this "anomalous" ice layer below other ice shelves has been the cause of the lack of ice shelf/ocean boundary detection [*Neal*, 1979] or misinterpretation of such boundary [*Robin et al*., 1983] in RES data. *Thyssen* [1988] first recognized that the strong reflection often detected in RES cross sections was caused by the interface between meteoric and salty ice rather than by ice and sea water. In more recent years, it has been extensively demonstrated that this type of ice is radio wave opaque and, when present at the base of the meteoric ice, it prevents direct estimation of the total thickness of the ice shelve using RES (see e.g., *Fricker et al*. [2001], *Holland et al*. [2009], *Jansen et al*. [2013]). This type of ice, which originates from sea water according to a different formation process with respect to sea ice, was named marine shelf ice by *Oerter et al*. [1992].

Thermo-haline circulation in the water filled cavity beneath an ice shelf (ice pump) [*Lewis and Perkin*, 1986] is the driving mechanism of marine ice formation. The water melting near the grounding zone produces low salinity and low density water that rises and flows outward

© 2015 American Geophysical Union. All rights reserved.

Accepted Article

along the shelf bottom. The pressure-dependent freezing point rises, generating supercooled water in which ice platelets form (frazil ice); these accumulate at the ice-shelf bottom and eventually compact to generate marine ice (see Figure 3). In practice, the ice accretes as a top-down sedimentation with progressive accumulation of the platelets creating a process similar to firn densification. As a consequence, the oldest ice, which usually has small grains [*Eicken et al*., 1994], is located at the top of the layer [*Treverrow et al*., 2010].

Marine ice is a mushy layer made up of ice platelets, trapped seawater cells and debris of both biogenic and lithogenic origin [*Oerter et al*., 1992; *Eicken et al*., 1994; *Moore et al*., 1994b; *Craven et al*., 2005]. In particular, the newly formed marine ice is characterized by anisotropic Crystal Orientation Fabric (COF) and a significant concentration of brines and insoluble particle inclusions. The size and concentration of brine pockets increase with depth and, in the lower part of the marine ice layer, tend to assume the form of interconnected vertical or sub-vertical channels and pores. Such brines can sometimes also be present at grain boundaries [*Eicken et al*., 1994]. Recent boreholes studies [*Craven et al*., 2004; *Craven et al*., 2005; *Craven et al*., 2009; *Hubbard et al*., 2012] have shown that marine ice has a specific arrangement. The upper part is characterized by an air-bubble free structure, distinct debris layers and brine pockets, and is impermeable but has brine pores incorporated within it. In contrast the lower part, which is hydraulically connected with the ocean water, is highly porous with brine drainage channels (honeycomb ice). In marine ice the salinity distribution with depth and its value with respect to sea ice salinity is in some way puzzling. Both *Craven et al*. [2009] and *Hubbard et al*. [2012] have found an increase in salinity with depth, whereas previous works [*Eicken et al*., 1994; *Moore et al*., 1994b; *Khazendar et al*., 2001] have found an opposite trend, even though the low salinity value near the meteoric/marine interface found by *Craven et al*. [2009] is similar to values from the upper portions of the marine ice found by *Eicken et al*. [1994]. Table 2 shows the salinity range for marine ice melt-water measured by several authors in various ice shelves and, for comparison, for multi-year sea ice melt-water. These elevated values explain the above mentioned high radio wave attenuation experienced in RES measurements collected on marine ice. Finally, it is worth noting that the lower values of marine ice salinity compared to that of sea ice cannot be explained by the normal desalination processes occurring in sea ice [*Eicken et al*., 1994] and a more complex process should be evoked [see e.g., *Tabraham*, 1998; *Tison et al*., 2001].

Accepted Article

© 2015 American Geophysical Union. All rights reserved.

3.4 Amorphous ice

On Earth, there is no evidence of natural amorphous ice, as the extreme temperature and pressure conditions required to produce it are never reached. Conversely, in the jovian satellites and in outer solar system bodies the presence of this type of ice has been extensively detected [e.g., *Bartels-Rausch et al*., 2012; *Hansen and Mc Cord*, 2004]. Amorphous ice is a metastable state of water ice (glassy solid), which can exist at low temperatures (below about 140 K) in various distinct forms. The most common are Low Density Amorphous ice (LDA, $\rho = 0.94 \pm 0.02$ g/cm^3) which can form from vapor deposition [*Hobbs*, 1974 and reference therein; *Johari et al.*, 1991] or hyperquenching [*Mayer and Bruggeller*, 1982; *Hallbrucker et al*., 1989], and High Density Amorphous ice (HDA, $\rho = 1.1 \pm 0.1$ g/cm^3) that can be produced by pressure-induced amorphization of ice Ih or high pressure compression of LDA [*Poole et al*., 1993]. An in depth discussion on amorphous ice formation can be found in, amongst others, *Mastrapa et al.* [2013]. The main processes evoked for amorphous ice formation on the Galilean icy satellite crusts are condensation of vapor at temperatures below 100 K or flash freezing of cryovolcanic liquids [e.g., *Cooper et al.*, 2001; *Mastrapa et al*., 2013]. However, amorphous ice can also be generated by disruption of surficial crystalline ice due to corpuscular radiation. In particular, the transition to amorphous ice occurs when crystalline ice is exposed to UV radiation [*Kouchi and Kuroda*, 1990], electron beams [*Dubochet and Lepault*, 1984], *He*-ions bombardment [*Baratta et al.*, 1991] or proton irradiation [*Famà et al*., 2010]. The transition process between amorphous and crystalline phases is in competition with thermal re-crystallization, which occurs at temperatures above 100 K [*Schmitt et al*., 1989]. *Hansen and McCord* [2004] hypothesized a balance between thermal kinetic crystallization and radiolytic disruption that favors the presence of amorphous ice on Europa, crystalline ice on Callisto and both types on Ganymede. This distribution is in agreement with spectroscopic data collected by the NIMS experiment [*Hansen and Mc Cord*, 2004; *Dalton et al.*, 2010]. It is worth noting, however, that amorphous ice is present only on the very surface, as below 1mm the ice is predominantly in its crystalline state [*Dalton et al*., 2010].

3.5 Clathrate hydrates

Clathrate hydrates are abundant on Earth in ice sheets, permafrost and sediments of the ocean floor [*Miller*, 1969; *Buffet*, 2000; *Sloan and Koh*, 2008] and have been long recognized to play an important role in the chemistry of the solar system [e.g., *Miller*, 1961; *Kargel and*

© 2015 American Geophysical Union. All rights reserved.

Accepted Article

Lunine, 1998; *Choukroun et al*., 2013]. In the specific case of the Galilean icy satellites, the stability domains of clathrate hydrates are compatible with the thermodynamic conditions present at shallow depths, where the temperature is well below 273 K and the pressure is about 1 MPa, as well as with those present at greater depths, as discussed in detail by several authors and summarized, amongst others, by *Kargel and Lunine* [1998] and *Choukroun et al*. [2013].

Clathrate hydrates are ice-like crystalline solids made of water and gas. The water molecules form a cage (host) and the gas molecules (guest) are entrapped in the cage cavities. Such hydrates can be considered a solid solution of gas molecules in a metastable lattice of water molecules. The presence of the gas stabilizes the entire structure as each gas molecule (which occupies a single cage) interacts with the surrounding water molecules through weak van der Waals forces. Indeed, the hydrogen bonds sustain the icy skeleton and the repulsive van der Waals interactions between the trapped gas molecules and the skeleton sustain the cage structure. The structure becomes stable when a sufficient number of cavities (not necessary all) are filled with gas; for this reason gas hydrates are nonstoichiometric compounds and can vary in composition. The degree of cavity saturation depends on temperature, pressure and concentration of the guest molecule. Due to the lack of chemical bonding between the guest and host molecules, the guest molecules are free to rotate inside the cages, and such rotation affects the dielectric properties of the hydrate if the guest molecule is polar (see section 7.1).

The formation of clathrate hydrates depends on the temperature and pressure environment, and on the properties of the guest molecule [*Sloan*, 1998]. The most common types of hydrates are type I and type II; also a third type of hydrate, named type H, can be encountered, but it is far less common in nature and will not be discussed here. Both types I and II have cubic structures but differ in the form of the cage. Type I hydrate consists of 46 water molecules and has the simplest structure formed by a dodecahedral cage (small cage) and a tetrakaidecahedral cage (large cage). Type II hydrate consists of 136 molecules of water and has the same small cage as type I hydrate (dodecahedral cage) but a larger cage that is hexakaidecahedral. A comprehensive description of the chemical-physical properties of clathrate hydrates is beyond the scope of this review and can be found in *Sloan and Koh* [2008].

Common guest molecules of type I hydrates are CH_4, C_2H_6, CO_2, and H_2S. Whereas C_2H_6 can only occupy the large cages, all other gases can occupy both cages. Other type I hydrate guests are SO_2, Cl_2, Xe and CO. Common type II guests are N_2, O_2, Ar, and Kr, which occupy both the large and small cages, and propane and isobutene which only occupy the

© 2015 American Geophysical Union. All rights reserved.

Accepted Article

large cages. Moreover, it has been recently reported that H_2 can also form a type II hydrate at high pressures (200-300 MPa) and low temperatures (240-249 K) [*Carroll*, 2014]. A complete list of guest molecules in type I and type II hydrates can be found in *Sloan and Koh* [2008].

IV ELECTROMAGNETIC PROPERTIES OF MATERIALS: THEORETICAL BACKGROUND

4.1 Dielectric properties

RIME, as any other GPR, uses radio waves to create an electromagnetic image of sub-surface structures; such an image is the result of the interaction between the waves and the different materials present at depth. The variability in the physical-chemical properties of rocks, soils, liquids and ices control their constitutive parameters (i.e., the complex dielectric permittivity and the complex magnetic permeability), which in turn define their different electromagnetic behaviors. For non-magnetic materials, as those expected in the crust of the jovian icy satellites, the dominant parameter is the dielectric permittivity, which describes both polarization and conduction phenomena. The polarization arises when an external electric field is applied to a material, producing a local redistribution of bound charges to new equilibrium positions and generating both storage and dissipation of energy. The second effect is the electric conduction, which also produces energy dissipation, and manifests itself only when free charges are present.

To quantify these phenomena we can consider the total density current J_T induced in a material when it is exposed to an external electric field $J_T = J_c + J_d = \sigma_s E + \frac{\partial D}{\partial t}$, where J_c is the conduction current density, J_d the displacement current density, E the applied electric field, σ_s the static conductivity, $D = \varepsilon_0 E + P = \varepsilon_0 \varepsilon E$ the dielectric displacement, P the polarization, $\varepsilon_0 = 8.85 \times 10^{-12}$ F m^{-1} the permittivity of the vacuum and ε the relative permittivity, which is in general a complex quantity $\varepsilon = \varepsilon' - j\varepsilon''$. If a harmonic electric field having angular frequency $\omega = 2\pi\nu$ (ν is the frequency) is applied, the total density current in the frequency domain can be written as

$$J_T = \sigma_s E + j\omega\varepsilon_0\varepsilon\, E = (\sigma_s + \omega\varepsilon_0\varepsilon'')E + j\omega\varepsilon_0\varepsilon' E = \sigma E + j\omega\varepsilon_0\varepsilon' E \quad (1)$$

© 2015 American Geophysical Union. All rights reserved.

Accepted Article

The quantity $\sigma = \sigma_s + \omega\varepsilon_0\varepsilon''$ is the effective conductivity [*Balanis*, 1989] and is given by two terms that describe the loss phenomena in the material. The first term, σ_s, which accounts for the inelastic scattering of free charge carriers during their migration in the material, is present at all frequencies (also at $\omega = 0$). In contrast, the second term, $\omega\varepsilon_0\varepsilon''$, which is due to friction in the polarization process, increases linearly with ω and vanishes at $\omega = 0$. Moreover, the term $j\omega\varepsilon_0\varepsilon'$ accounts for the displacement current and is directly linked to the polarization of the material.

Considering the conductivity term, we can re-define the complex dielectric permittivity as follows

$$\varepsilon = \varepsilon' - j(\varepsilon'' + \frac{\sigma_s}{\omega\varepsilon_0}) = \varepsilon' - j\frac{\sigma}{\omega\varepsilon_0} \quad (2)$$

It is also useful to define the loss tangent $\tan\delta = \frac{\varepsilon'' + \sigma_s/\omega\varepsilon_0}{\varepsilon'}$, which describes the energy dissipation process in a dielectric material.

Polarization may be due to several distinct processes: i) the displacement of bound negative and positive charges in atoms and molecules (atomic or ionic polarization); ii) the orientation of existing dipoles towards the direction of the applied field (orientational polarization); and iii) the separation of mobile charge carriers at interfaces (space charge polarization) or other defect boundaries (hopping polarization). In general, the time required for electronic and molecular polarization and depolarization is very short ($<10^{-12}$ s). This deformational polarization process is also referred to as the resonance process because it involves vibrating modes. On the other hand, the time required for orientational, hopping, or space charge polarization and depolarization is relatively long and varies over a wide range, depending on the dielectric system. Such polarization phenomena are sometimes referred to as relaxation processes because they involve a relaxation time τ_{rel}. A relaxation phenomenon occurs when a restoring action tends to bring the excited system back to its original equilibrium state. Figure 5 qualitatively illustrates the time response, in a generic dielectric, of the various polarization processes when a step function excitation field E is applied.

In the frequency domain, the relaxation phenomena translate into a dispersive behavior of the dielectric parameters. The most common theoretical model used to describe the spectral behavior of a wide range of geo-materials is the Debye equation [*Debye*, 1929], which for a single relaxation process can be written as

© 2015 American Geophysical Union. All rights reserved.

Accepted Article

$$\varepsilon(\omega) = \varepsilon_\infty + \frac{(\varepsilon_s - \varepsilon_\infty)}{1 + j\,\omega/\omega_{rel}} - j\frac{\sigma_s}{\omega\varepsilon_0}$$
$$\varepsilon'(\omega) = \varepsilon_\infty + \frac{(\varepsilon_s - \varepsilon_\infty)}{1 + (\omega/\omega_{rel})^2} \qquad (3)$$
$$\varepsilon''(\omega) = \frac{(\varepsilon_s - \varepsilon_\infty)\omega}{\omega_{rel}\left[1 + (\omega/\omega_{rel})^2\right]} + \frac{\sigma_s}{\omega\varepsilon_0}$$

Where $\omega_{rel} = 1/\tau_{rel}$ is the relaxation angular frequency, and ε_s and ε_∞ are the static and the high frequency permittivities, respectively. Note however that some experimental data can be better fitted by Cole-Cole, Cole-Davidson or Havriliak-Negami models [*Jonscher,* 1983]. With some algebraic manipulations the effective conductivity can be written (using the Debye parameters ε_s, ε_∞ and ω_{rel}), as $\sigma = \sigma_s + (\sigma_\infty - \sigma_s)\frac{\omega^2}{\omega^2 + \omega_{rel}^2}$, where σ_∞ is the high frequency conductivity $\sigma_\infty = \sigma_s + \varepsilon_0(\varepsilon_s - \varepsilon_\infty)\omega_{rel}$. Figure 6 qualitatively shows the behavior of the real and imaginary parts of permittivity and effective conductivity versus frequency. We can note that, at high frequencies (i.e., for $\omega \gg \omega_{rel}$) the effective conductivity approaches σ_∞ and the real and imaginary parts approach ε_∞ and $\sigma_\infty/\omega\varepsilon_0$, respectively.

The dielectric parameters (i.e., ε', ε'' and σ) are temperature dependent [*von Hippel*, 1954], as qualitatively shown in Figure 7. In particular, the relaxation angular frequency follows the Arrhenius equation

$$\omega_{rel} = \omega_0 \exp\left(-E_{\omega_{rel}}/k_B T\right) \qquad (4)$$

where ω_0 is a proportional coefficient, $E_{\omega_{rel}}$ is a quantity having the dimension of energy (often called the activation energy), k_B is the Boltzmann constant and T is the temperature in kelvin. The difference between static and high-frequency-limit permittivity is also temperature dependent and it is given by

$$\varepsilon_s - \varepsilon_\infty = \frac{a}{T} \qquad (5)$$

where a is a constant.

Accepted Article

© 2015 American Geophysical Union. All rights reserved.

4.2 Wave propagation

The electromagnetic waves emitted by a GPR antenna can be locally approximated by plane waves, whose electric component can be expressed as $E(t,z) = E_0 e^{j\omega t} e^{-\gamma z}$, where $\gamma = j(\omega/c)\sqrt{\varepsilon} = \alpha + j\beta$ is the propagation constant (for non-magnetic materials), E_0 is the amplitude, z is the direction of propagation, c is the speed of light in vacuum, and t is the time. The real part of the propagation constant is the attenuation factor which determines the maximum penetration depth of the radar waves and is given by

$$\alpha = \frac{\omega}{c\sqrt{2}}\left[\sqrt{\varepsilon'^2 + \varepsilon''^2} - \varepsilon'\right]^{1/2} \approx \frac{\sigma}{2c\varepsilon_0\sqrt{\varepsilon'}} \qquad (6)$$

The approximation in Equation 6 is valid for $\sigma \ll \varepsilon'\varepsilon_0\omega$, i.e., for low conductive materials like ice. The parameter $\beta = \omega/\mathrm{v}$ is the phase constant accounting for the phase velocity

$$\mathrm{v} = \frac{c\sqrt{2}}{\left[\sqrt{\varepsilon'^2 + \varepsilon''^2} + \varepsilon'\right]^{1/2}} \approx \frac{c}{\sqrt{\varepsilon'}} \qquad (7)$$

which allows the conversion from travel time to depth. Furthermore, knowing the velocity, it is possible to estimate the range resolution as follows

$$\Delta z = \frac{\mathrm{v}}{\Delta\nu} \qquad (8)$$

where $\Delta\nu$ is the radar signal bandwidth.

The electromagnetic image is the result of radar signal reflections from any dielectric contrast present in the subsurface. For normally incident plane waves and perfectly flat interfaces, the amplitude of the reflected signal is proportional to the Fresnel reflection coefficient

$$R = \frac{\sqrt{\varepsilon_1} - \sqrt{\varepsilon_2}}{\sqrt{\varepsilon_1} + \sqrt{\varepsilon_2}} \qquad (9)$$

where the subscripts refer to adjacent layers.

Accepted Article

© 2015 American Geophysical Union. All rights reserved.

V AN OVERVIEW OF WATER ICE DIELECTRIC PROPERTIES

5.1 Theoretical background

The Debye relaxation model given in Equation 3 is well suited to describe the dielectric behavior of pure water ice up to several hundreds of MHz [*Johari*, 1981], even if below 250 K a Cole-Cole model [*Cole and Cole*, 1941] is more suitable (*von Hippel et al*, 1971; *Popov et al*., 2015). Such behavior, essentially due to proton hopping polarization, has been extensively studied by several authors, with major contributions from *Bjerrum* [1952], *Granicher et al*. [1957], *Jaccard* [1959], *Onsager and Dupuis* [1960], *Jaccard* [1964], *Nagle* [1979], and *Bilgram and Granicher* [1974]. In this section we outline the basic principles and main results of the Jaccard theory for pure water ice Ih [*Jaccard*, 1959; *Jaccard* 1964]. This theory is the most generally accepted amongst the scientific community, although its theoretical basis was strongly criticized in a series of papers published by von Hippel and co-workers [*von Hippel et al.*, 1971, *von Hippel*, 1971; *Maidique et al.*, 1971; *von Hippel*, 1988]. Jaccard theory is based on the presence of protonic point defects (intrinsic defects) in the ice lattice whose motion has the effect of reorienting the molecules along the so-called protonic motion path. Two different types of protonic point defects can occur inside the ice lattice structure: a first type associated with the rotation of H_2O molecules and a second one due to proton transfer between adjacent molecules. The rotation of the H_2O molecule inside the lattice produces a Bjerrum defect pair (L and D) generating a proton-deficient site, known as a Bjerrum L-defect, and a site with two facing protons, known as a Bjerrum D-defect (Figure 8a). In addition, the motion of the proton along the bond transfers the ionization state between adjacent H_2O molecules, generating a pair of ionic defects, H_3O^+ and OH^- (Figure 8b).

The protonic hopping results in a unique dielectric behavior of pure water ice, since the dielectric permittivity and the electrical conductivity are strongly coupled. As pointed out by *Petrenko and Whitworth* [1999]: "In most materials the process of dielectric polarization and electrical conductivity are totally distinct and can be analyzed independently. This is not the case for ice, where both are properties of the protonic subsystem and arise from motions of the two pairs of protonic point defects". As a consequence, the application of an electrical field produces a motion of the defects along the ice lattice, giving rise to both polarization and conduction phenomena.

For each type of defect we can define the partial conductivity as

© 2015 American Geophysical Union. All rights reserved.

Accepted Article

$$\sigma_i = n_i \mu_i |e_i| \qquad (10)$$

where the subscript i indicates the type of defect, n_i represents the defect volumetric concentration, μ_i the mobility and e_i the effective charge. Some of these parameters have been experimentally estimated and are summarized in Table 3 [*Petrenko*, 1993; *Petrenko and Whitworth*, 1999 and reference therein]; however, these values should be taken with caution as they have been estimated

from measurements performed on pure and doped ice, often following different experimental procedures (see section 5.2 and section 5.5).

Indeed, such values are sometimes incompatible and affected by large uncertainties [*Petrenko and Whitworth*, 1999]: the effective charge uncertainty is on the order of $0.01e$, the relative error on the mobility is about 50% and on the activation energy is less than 25%.

To keep the mathematical approach simple, it is convenient to group the different contributions into ionic conductivity $\sigma_{\pm} = \sigma_{H_3O^+} + \sigma_{OH^-}$ and Bjerrum conductivity $\sigma_{DL} = \sigma_L + \sigma_D$. The way these terms combine into the equation of the pure water ice conductivity depends on frequency. Well above the relaxation frequency ($\nu \gg \nu_{rel}$, e.g., $\nu_{rel} \approx 1\,\text{kHz}$ @ 250K) each defect moves independently from the others and the high frequency conductivity is given by

$$\sigma_\infty = \sigma_{\pm} + \sigma_{DL} \qquad (11)$$

The static conductivity can be retrieved from the following equation

$$\frac{e^2}{\sigma_S} = \frac{e_{\pm}^{\ 2}}{\sigma_{\pm}} + \frac{e_{DL}^{\ 2}}{\sigma_{DL}} \qquad (12)$$

where $\sigma_s \neq 0$ only if both types of defect are present.

In any case, regardless of the predominant type of defect (ionic or Bjerrum), the high frequency conductivity σ_∞ is dominated by the majority carriers (i.e., the defects for which the product "concentration × mobility" is the largest), whereas the low frequency conductivity σ_s is mainly due to the minority carriers. Depending on the temperature, some defects dominate over the others (see Table 3): for example, above about 230 K, the majority carriers are the Bjerrum defects and the minority carriers the ionic defects. It follows that $\sigma_{DL} \gg \sigma_{\pm}$, thus $\sigma_\infty \approx \sigma_{DL}$ and $\sigma_s \approx \sigma_{\pm}\left(e^2/e_{\pm}^2\right)$ [*Petrenko and Whitworth*, 1999].

According to the Jaccard theory, the pure water ice Debye parameters can be expressed in terms of intrinsic defects [*Jaccard*, 1964; *Petrenko and Whitworth*, 1999]

© 2015 American Geophysical Union. All rights reserved.

$$\omega_{rel} = \Phi\left(\frac{\sigma_{DL}}{e_{DL}^{\ 2}} + \frac{\sigma_{\pm}}{e_{\pm}^{\ 2}}\right) \qquad (13)$$

$$\varepsilon_s = \varepsilon_\infty + \frac{\left(\sigma_{\pm}/e_{\pm} - \sigma_{DL}/e_{DL}\right)^2}{\varepsilon_0 \Phi\left(\sigma_{\pm}/e_{\pm}^{\ 2} + \sigma_{DL}/e_{DL}^{\ 2}\right)^2} \qquad (14)$$

where $\Phi = \frac{8}{3} r_{O-O} k_B T$ is the polarizability constant, which depends on the ice temperature and the distance r_{O-O} between adjacent oxygen atoms. In water ice the term ε_∞ is due to both electronic polarization and molecule distortions, is slightly dependent on temperature, and assumes values of between 3.1-3.2 (3.16 at 253 K decreasing to 3.09 at 2 K) [*Gough*, 1972].

The partial conductivities defined in Equation 10 depend on defect volumetric concentration and mobility, which are both temperature dependent. More specifically, the volumetric concentration of the intrinsic defects is given by $n_i = N_i \exp\left(-E_i^F / 2k_B T\right)$, where E_i^F are the energies of formation of defect pairs, $N_i = \frac{2}{3} N$ for ionic defects and $N_i = N$ for Bjerrum defects (with N being the number of H_2O molecules per unit volume). The mobility μ_i follows the Arrhenius equation $\mu_i = M_i \frac{1}{T} \exp\left(-E_i^M / k_B T\right)$, where M_i is a normalization coefficient and E_i^M is the activation energy for motion. Considering also the set of Equations 11-14, it follows that the Debye parameters are temperature dependent. For example, if only one type of defect dominates, as in the case of L-defects above about 230 K (see Table 3), the conductivity becomes

$$\sigma_\infty - \sigma_s \propto \frac{1}{T} \exp\left(-\frac{E_{\sigma_\infty}}{k_B T}\right) \qquad (15)$$

where $E_{\sigma_\infty} = 1/2 E_L^F + E_L^M$. In this specific case, the relaxation angular frequency ω_{rel}, expressed in Equation (13), assumes the form of Equation 4 where $E_{\omega_{rel}} = E_{\sigma_\infty}$ and Equation 14 assumes the form of Equation 5.

5.2 Experimental data

Pure water ice has been studied in the laboratory over a wide range of temperatures and frequencies, even though not all frequency bands have been uniformly explored [for reviews on the subject see e.g., *Franks*, 1972; *Hobbs*, 1974; *Johari*, 1981; *Warren*, 1984; *Petrenko*,

Accepted Article

© 2015 American Geophysical Union. All rights reserved.

1993; *Tonkonogov*, 1998; *Petrenko and Whitworth*, 1999; *Fujita et al*., 2000; *Warren and Brandt*, 2008]. In general, measurements confirm that the dielectric behavior of pure water ice follows the Debye model at relatively high temperatures (above 230 K), as illustrated in Figure 9.

However, despite intensive research conducted over almost 70 years, several aspects regarding pure water ice permittivity and conductivity still remain unclear, as the results of various studies have been sometimes conflicting or even incompatible. After the pioneering work of *Auty and Cole* [1952], the scientific community quickly became aware that the dielectric measurements on pure water ice are difficult to perform and to reproduce. The lack of a standard procedure in sample preparation and measuring methodology raises some questions about the reliability of the experimental data, as clearly highlighted by the following quote: "Only very pure single crystals in proper crystallographic orientation, measured with the proper electrode arrangement over wide frequency and temperature ranges as a function of time, prehistory, and field strength can provide unobjectionable results" [*von Hippel et al.*, 1971]. In particular, the different experimental procedures employed to form and grow ice, including sample history and aging [e.g., *Maidique et al*., 1971; *Taubenbergber*, 1973; *Johari and Jones*, 1976], can introduce microscopic and macroscopic differences, such as: specific crystal orientations [e.g., *Worz and Cole*, 1969; *Kawada*, 1978]; dislocations [*Itagaki*, 1978]; cracks and fractures [e.g., *Auty and Cole*, 1952; *Worz and Cole*, 1969; *Davidson*, 1973]; gas bubbles and inclusions [e.g., *Takei*, 2007]; chemical impurities [e.g., *Ida et al*., 1966; *Gough and Davidson*, 1970; *Kawada*, 1978]; and vacancies and other lattice imperfections [*Takei*, 2007]. Moreover, the ice growth process and the cooling procedure can affect, often in a non-controllable way, the ice/electrode contact (introducing gaps of air or cracks), as the materials have different thermal expansion coefficients [e.g., *Auty and Cole*, 1952; *Worz and Cole*, 1969; *Itagaki*, 1978]. All these aspects can significantly modify the characteristic Debye behavior expected for pure water ice, as they can introduce additional relaxations [*von Hippel et al*., 1971], shorten the relaxation time [*Gough and Davidson*, 1970], widen the characteristic bell-shape curve [*Auty and Cole*, 1952] or affect the $\nu_{rel} - 1/T$ trend [*Kawada*, 1978].

Table 4 gives an idea of the variability in sample characteristics and measuring parameters reported in several studies devoted to the estimation of pure water ice dielectric properties, performed over a wide frequency band (from few millihertz to few megahertz). Aside from the measuring technique, which typically involves the measurement of the impedance of a

© 2015 American Geophysical Union. All rights reserved.

capacitor filled with the test material (see Appendix I), the sample type, the temperature range and the frequency band are quite different. Moreover, the measurements reported in Table 4 show a variety of critical aspects which make it difficult to compare the experimental data.

The discrepancies amongst the results are evident when data extracted from different experiments are plotted together in Figure 10, where the Debye parameters (ε_s and ν_{rel}) are graphed as a function of temperature. Figure 10 (left panel) illustrates how the different samples (single-crystal or polycrystalline) follow Equation (5) but with different slopes. Figure 10 (right panel) shows that the various data are in general agreement and follow Equation (4) with similar activation energies only in the 273-230 K temperature interval, and that this agreement holds even if the samples have different structures (single-crystal or polycrystalline). However, below about 230 K two effects are visible: a change in the slope of each curve (excluding *Auty and Cole* [1952]) and a remarkable divergence between the curves. This behavior has been attributed to the presence of impurities [*Gough and Davidson*, 1970; *Kawada*, 1978] or to the interchange in the role of the majority and minority carriers [*Bilgram and Granicher*, 1974; *Popov et al*., 2015], and is still a matter of intense debate.

At higher frequencies, i.e., the MHz range, the experimental data indicate that the real part of permittivity (ε_∞ in the Debye model) is approximately constant with temperature and frequency, and that its value can also be extended up to the THz range [*Johari*, 1981; *Bohleber et al*., 2012]. On the other hand, the measurement of the imaginary part of pure water ice in this frequency range is challenging, especially at low temperatures, due to the sensitivity limit of the instruments (see Appendix 1), as demonstrated by the very sparse data present in the literature [*Johari and Charette*, 1975; *Johari*, 1976; *Johari*, 1981]. To fill this gap, several authors [*Matzler and Wegmuller*, 1987; *Koh*, 1992; *Surdyk and Fujita*, 1995; *Matsuoka et al*., 1996a; *Matsuoka et al*., 1997; *Fujita* et al., 2000; *Warren and Brandt*, 2008] have attempted to estimate the dissipative behavior of pure water ice in the MHz-GHz range by interpolating low frequency and microwave data. The most common equation used to fit the experimental data is given by

$$\varepsilon'' = \frac{\mathrm{A}}{\nu} + \mathrm{B}\,\nu^{\mathrm{C}} \qquad (16)$$

where the frequency ν is expressed in GHz. The first term of Equation 16 accounts for the right-tail of the Debye relaxation and the second term is due to the lattice vibration resonance in the far-infrared region [*Matzler and Wegmuller*, 1987; *Matsuoka et al*., 1996a; *Fujita et*

© 2015 American Geophysical Union. All rights reserved.

Accepted Article

al., 2000;]. Table 5 summaries the values of *A*, *B* and *C* coefficients estimated by *Matsuoka et al*. [1996a] and integrated by *Fujita et al*. [2000].

5.3 Effect of anisotropy and density

Anisotropy and density variation are important physical parameters in a water icy layer, as they can generate a detectable permittivity contrast. Anisotropy describes the change in permittivity associated with the orientation of the ice crystals with respect to the wave propagation path. A single Ih ice crystal exhibits uniaxial symmetry, with the optical axis coinciding with the crystallographic c-axis, therefore its complex permittivity is expressed as a tensor

$$\varepsilon = \begin{bmatrix} \varepsilon_{\perp c} & 0 & 0 \\ 0 & \varepsilon_{\perp c} & 0 \\ 0 & 0 & \varepsilon_{\| c} \end{bmatrix} \qquad (17)$$

where $\varepsilon_{\perp c}$ and $\varepsilon_{\| c}$ are the components when the electrical field vector is perpendicular and parallel to the c-axis, respectively [*Humbel et al*., 1953; *Kawada*, 1978; *Fujita*, 2000].

The effect of anisotropy on the real part of permittivity is strongly frequency dependent. At low frequencies the real part (static permittivity ε_s) exhibits a 15% variation between $\varepsilon'_{\| c}$ and $\varepsilon'_{\perp c}$ (see Figure 10, left panel) [*von Hippel*, 1954; *Kawada*, 1978; *Takei and Maeno*, 1987], and a value of about 100 for $\varepsilon'_{\| c}$ [*Kawada*, 1978] which is always larger than $\varepsilon'_{\perp c}$. At high frequencies (above 1 MHz) such variation (i.e., in ε_∞) is on the order of 1% [*Matsuoka et al*., 1997], with a value of about 3.17 for $\varepsilon'_{\| c}$. Moreover, anisotropy is weakly dependent on temperature at these frequencies, according to the relationship $\varepsilon'_{\| c} - \varepsilon'_{\perp c} = 0.0256 \pm 0.001 + 3.6 \times 10^{-5} T$ [*Fujita*, 2000]. The imaginary part of permittivity is anisotropic only at low frequencies (below 1 MHz) [*Worz and Cole*; 1969; *Kawada*, 1978; *Matsuoka et al*., 1997] where $\varepsilon''_{\| c}$ is larger than $\varepsilon''_{\perp c}$ by about 20%, whereas at higher frequencies no anisotropy has been observed [*Fujita*, 2000; *Matsuoka et al*., 1997]. It is worth noting that in isotropic polycrystalline ice (i.e., when the c-axis is randomly distributed), the bulk permittivity is given by a simple combination of parallel and perpendicular permittivities $\varepsilon = \left(2\varepsilon_{\perp c} + \varepsilon_{\| c}\right)/3$ [*Fujita et al*., 2000].

© 2015 American Geophysical Union. All rights reserved.

As mentioned above, the other physical parameter affecting the water ice permittivity is density. This parameter is mainly influenced by the air content (bubbles) and is substantially independent of the presence of chemical impurities, thus what is found for natural ice can be extended to pure water ice. Experimental work conducted in the polar regions has shown that density influences the ε' value of both firn and natural polycrystalline ice [*Robin et al*., 1969; *Glenn and Paren*, 1975; *Kovacs et al*., 1995]. *Robin et al*. [1969], using radar interferometry data acquired in Greenland, were the first to find an empirical equation which relates ε' to density $\varepsilon' = (1 + 0.851\rho)^2$, where ρ is expressed in g cm^{-3}. Several authors have proposed slightly different versions of the *Robin et al.* [1969] equation which, for brevity, are not reported here, but can be found in *Kovacs et al*. [1995] and, more recently, in *Dowdeswell and Evans* [2004]. Finally, experimental data seem to suggest that also the imaginary part of permittivity is affected by an increase in density, as shown by *Tiuri et al*. [1984] for dry snow, by *Glenn and Paren* [1975], *Reynolds* [1985] and *Barnes et al*. [2002] for firn, and by *Barnes et al*. [2002] for doped ices.

5.4 Amorphous ice

The laboratory procedure used to obtain amorphous ice is complex and the physical properties of the ice obtained in this manner depend on the temperature profile and pressure rate of the transition process [*Mishima et al.*, 1985; *Johari and Anderson*, 2007a, b and reference therein]. Very few data have been published on the dielectric properties of amorphous ice and the procedures used to prepare these samples can be found in *Johari et al.* [1991], *Johari and Andersson* [2007a], and *Andersson* [2008].

The dielectric measurements performed in the kHz range on Amorphous Solid Water (ASW) grown from vapor deposition (i.e., at low pressures) [*Johari et al.*, 1991], gave an indicative value of 2.9 ± 0.3 for the real part of permittivity at 80 K. On the other hand, the measurement of high pressure samples grown from a crystalline phase seem to indicate that the real part of permittivity at high frequency (ε_∞) is higher than that of ice Ih. *Andersson* [2007; 2008] determined dielectric properties of both HDA and LDA, measuring the complex permittivity of samples at different temperatures and pressures in the frequency range 1 mHz – 10 kHz. The author analyzed the dielectric spectra using the Cole-Cole model and found a relaxation time $\tau_{rel} \approx 2$ s ($\nu_{rel} \approx 0.1$ Hz) for HDA ice at 133 K. Moreover, *Andersson* [2008] experimentally confirmed that expected from theoretical considerations, i.e., the dependence

© 2015 American Geophysical Union. All rights reserved.

of ε_∞ on density, finding $\varepsilon_\infty \approx 5$ for HDA [*Andersson and Inaba,* 2006] and $\varepsilon_\infty = 6.4$ for very High Density Amorphous ice [*Andersson, 2005*]. The evaluation of the LDA relaxation time was more complex, as the investigations were carried out at frequencies higher than that of LDA relaxation. In any case, the author concluded that the relaxation time τ_{rel} at 130 K falls between 100s and 1000s (i.e., $0.16 \le \nu_{rel} \le 1.6$ mHz) [*Andersson,* 2007; 2008].

5.5 Effect of dopants

The measurements performed on pure water ice do not allow one to fully discriminate the role of each defect on the ice dielectric properties. For this reason it has been common, since the early days of ice electrical measurements, to use chemical dopants to enhance the effect of specific defects. However, water ice is known to be extremely efficient in expelling chemical impurities, and thus when these impurities are present they are usually incorporated as inclusions or clusters [*Petrenko and Withworth,* 1999]. Only specific chemical compounds at very low concentrations (lower than 10^{-3} - 10^{-2} M in the mother solution) can be incorporated in the ice lattice as true mixed crystals, thus forming a solid solution with the ice. In this case the experimental results can be interpreted within the framework of the Jaccard theory because such impurities are able to replace the water molecules, thereby generating additional defects ("extrinsic defects") and to modify the dielectric properties of the ice even at very low concentrations (on the order of micromoles). On the other hand, at higher concentrations (greater than 10^{-3} - 10^{-2} M) some structural imperfections, like bubbles, start to form in the ice [*Granicher,* 1963] and the impurities are segregated at the grain boundaries or as inclusions in the grains, resulting in a much more complex dielectric behavior which cannot be explained only in terms of the Jaccard theory.

Historically, the first molecules used to dope ice were HF and NH_3 [*Granicher,* 1963 and references therein], as they have approximately the same dimensions of the water molecules and can easily be incorporated in the ice lattice to create extrinsic defects. According to Jaccard theory, such defects increase the partial conductivities (cf. Equations (10)) and affect the dielectric properties of the doped ice in terms of σ_s, σ_∞, ε_s, and ν_{rel} (see Equations (11-14)), whereas they do not appreciably affect ε_∞ [*Matsuoka et al*., 1996b]. In particular, HF increases the number of L and H_3O^+ defects and NH_3 the number of D and OH^- defects. However, it should be highlighted that despite many laboratory experiments devoted to ice doped with these molecules [e.g., *Granicher et al*., 1957; *Steinemann and Granicher,* 1957;

© 2015 American Geophysical Union. All rights reserved.

Levi and Lubart, 1961; *Granicher*, 1963; *Levi*, 1967; *Bilgram and Granicher*, 1974; *Hobbs*, 1974; *Petrenko and Withworth*, 1999 and references therein] are in general agreement with the Jaccard theory [*Camplin et al*., 1978], a full understanding of the doping mechanisms in terms of impurity incorporation and chemical dissociation, and the consequent generation of the defects, has not yet been achieved. After many years of experimental studies it is now evident that the dielectric properties of the doped ice do not depend on the class of the dopant molecule (i.e., if it is an acid, a basis or a salt), but rather the key parameter is the capability of the dopant to substitute the water molecules and to generate protonic point defects. For example, some acids like HF or HCl can be very effective dopants while others, like H_2SO_4, are surprisingly less efficient in creating extrinsic defects and changing the dielectric properties of the ice [*Gross et al*., 1994; *Gross and Svec*, 1997].

In the following we will discuss in detail the dielectric properties of HF doped ice, as this molecule is the most soluble and active ice dopant, and can be considered as a reference model to explain the behavior of other compounds. Figure 11 schematically illustrates the static and high frequency conductivity behavior as a function of temperature and HF concentration. At low concentrations and high temperatures (left panel), σ_∞ is determined by the intrinsic L defects (majority carriers) and rapidly decreases with temperature due to the high activation energy (about 0.6eV) of such defects [*Camplin et al*., 1978]. Moreover, the high frequency conductivity increases weakly with the impurity concentration (orange line in the insert plot of Figure 11, left panel), as the dopant introduces only a small amount of extrinsic L defects with respect to those that already exist in the ice as intrinsic L defects (cf. Table 3). The presence of HF also introduces extrinsic H_3O^+ defects (minority carriers); these new defects significantly affect the static conductivity value because they add to the intrinsic H_3O^+ defects, which are a few orders of magnitude lower than those of L defects (cf. Table 3). As a consequence, the trend of σ_s increases steeply with the impurity concentration (green line in the insert plot of Figure 11, left panel). Furthermore, since the extrinsic H_3O^+ defects are the product of the full dissociation of HF, they exhibit a very small activation energy, with the consequence being that σ_s is almost independent of temperature. As the temperature decreases or the concentration increases the behavior of σ_s and σ_∞ becomes more complex, because both L and H_3O^+ defects contribute to these quantities without predominance of one defect over the other. The defects modify and interchange their role when the ice passes the so called "crossover temperature" T_c (Figure 11, central panel).

© 2015 American Geophysical Union. All rights reserved.

Accepted Article

Above T_c the L defects are the majority carriers and dominate σ_∞ (orange curve), whereas H_3O^+ are the minority carriers and control σ_s (green curve). The opposite is true below T_c, as the L defects become the minority carriers, now affecting σ_s (green curve), and H_3O^+ the majority carriers, affecting σ_∞ (orange curve). As a consequence, also the temperature slope of the high and low frequency conductivities interchange: σ_∞ vs 1/T becomes less steeper and σ_s vs 1/T becomes much steeper. Finally, at high concentrations (right panel of Figure 11) the magnitude of σ_∞ and σ_s become comparable and the experimental data indicate that σ_s tends to become proportional to $[x]_{HF}^{1/2}$ (inset plot in the right panel).

The dielectric behavior of HCl doped ice is quite similar to that of HF doped ice [*Gross et al*., 1978] even if, at low temperatures (i.e., below the crossover temperature), the curves of σ_s and σ_∞ are less separated than those of the HF doped ice [*Takei and Maeno*, 1987]. The effect of Cl^- in ice has also been studied using salts like: NaCl [*Gross et al*., 1978; *Grimm et al*., 2008], *KCl* [*Maeno*, 1973], and $CaCl_2$ [*Grimm et al*., 2008]. In particular, *Gross et al*. [1978] did not find any appreciable difference between the effect produced by the acid and the salt dopants and thus made the assumption that Cl^- enters the ice lattice as HCl [*Maeno*, 1973; *Gross et al*., 1978; *Petrenko and Withworth*, 1999]. A different interpretation has recently been given by *Grimm et al*. [2008] who, on the basis of their experimental evidence, suggested that Cl^- enters the ice lattice producing two L defects instead of one L defect and one H_3O^+, as in the case of HCl.

The other important ice dopant is NH_3, which has been studied, amongst others, by *Levi et al*. [1963], *Chai and Vogelhut* [1965], *Arias et al.* [1966], and *Hubmann* [1978]. According to the Jaccard theory, this molecule should introduce both OH^- and D extrinsic defects in the ice lattice, thus increasing σ_s and decreasing σ_∞ because the D defects partially compensate the excess of intrinsic L defects [*Petrenko and Withworth*, 1999]. The experimental data, however, only show an increase of σ_s with the impurity concentration, and no appreciable variation in σ_∞ has been found [*Arias et al*., 1966; *Hubmann*, 1978]. This observation seems to indicate that the conductivity is only affected by the OH^- defects [*Petrenko and Withworth*, 1999 and references therein]. More interesting, it has been proven that the presence of NH_4^+ ions increases the solubility of some anions (e.g., Cl^-, F^-) or even facilitates the incorporation of some insoluble anions (e.g., NO_3^-, SO_4^{2-}) in the ice lattice [*Gross et al*.,

© 2015 American Geophysical Union. All rights reserved.

1977; *Gross et al*., 1987; *Gross et al*., 1994]. It follows that, given two compounds having the same anion and the same impurity concentration, the compound with the NH_4^+ cation will have a higher σ_∞ with respect to the compound without the ammonium [e.g., *Gross and Svec*, 1997; *Stillman et al*., 2013a]. This result can be explained assuming that NH_4^+ favors the accommodation of the soluble and insoluble anions in the ice structure, generating more point defects [*Gross and Svec*, 1997]. More recently, *Stillman et al*. [2013a] interpreted the increase in σ_∞ associated with NH_4^+ ions to a larger L defects concentration produced by an enhanced partitioning of Cl^-.

The few examples discussed above clearly illustrate that, in general, doped ice electrical properties are poorly constrained because they depend, in a non-trivial way, on solubility and concentration of the dopant and on the temperature of the ice. Unfortunately, the experiments in this field suffer the same problems already discussed for pure water ice, as the difference in sample preparation, impurity concentration, laboratory procedure and measurement techniques do not yield reproducible data. The lack of consistency in the experimental procedures is probably the main cause preventing a univocal interpretation of the doped ice dielectric phenomena.

VI DIELECTRIC PROPERTIES OF NATURAL WATER ICE

6.1 Meteoric ice

What is known about the electrical properties of meteoric ice is mainly based on the results obtained during more than forty years of polar (and sub-polar) ice core research. In fact, the electrical measurements have been a powerful tool to estimate, in a non-destructive way, the impurity concentration in each resolvable ice layer composing the core (see Appendix 1), with the final goal of inferring the environmental conditions at the time the ice was formed [*Wolff*, 2000 and references therein]. In meteoric ice the four most common ionic impurities are: i) sea salt ions; ii) sulfuric acid produced by volcanic eruptions; iii) ammonium and organic anions; and iv) terrestrial dust-derived ions (cf. Figure 4). In general, the bulk ionic concentration in meteoric ice is low, on the order 1–10 μM, even though much larger concentrations (several hundreds of μM) can be found in some glacier basal layers [*Cuffey and Paterson*, 2010]. The ice core electrical measurements have been performed using either Electrical Conductivity Measurements (ECM) [*Hammer*, 1980] or Dielectric Profiling (DEP) [e.g., *Moore et al*., 1994a; *Wolff et al*., 1997; *Wolff*, 2000] (for details see Appendix I). The

© 2015 American Geophysical Union. All rights reserved.

measurements conducted with ECM have found a nonlinear relation between the Direct Current (DC) and H^+ concentration measured in the melt-water, whereas no correlations have been reported with other ionic species [*Hammer*, 1980]. It is worth noting that, as explained in detail in Appendix I, ECM does not allow one to retrieve the σ_s value of ice [*Maccagnan and Duval*, 1982]. On the other hand, DEP measurements have shown that high frequency conductivity is linearly dependent on ionic impurity concentration in melt-water, according to the general expression

$$\sigma_\infty = \sigma_{\infty\, pure} + \sum_i \hat{\sigma}_i \left[x_i \right] \qquad (18)$$

where $\sigma_{\infty\, pure}$ is the high frequency conductivity of pure ice, $\left[x_i \right]$ are the concentration of the specific ions, and $\hat{\sigma}_i$ are the molar conductivities. The most common relationship found in the literature is that proposed by *Wolff et al*. [1995]

$$\sigma_\infty = 9 + 4\left[H^+ \right] + 1\left[NH_4^+ \right] + 0.55\left[Cl^- \right] \qquad (19)$$

where σ_∞ is expressed in μS m^{-1} and the ionic concentration in μM. In Equation (19) the first term represents the contribution of pure ice, estimated by *Camplin et al*. [1978] on a laboratory-grown single crystal. The second coefficient was estimated by *Moore et al*. [1989; 1994a] based on measurements performed on ice cores collected in Antarctica and Greenland. The third coefficient was calculated by *Moore et al*. [1994a] from data collected on Greenland cores, where ammonium salts are common. Finally, the forth term was estimated by *Moore et al*. [1992] from Greenland cores containing sea salts. In Equation (19) the uncertainties in both the acid and ammonium coefficients are as large as 20%, whereas those in the others two coefficients are only on the order of a few percent [*Moore et al*., 1994a; *Wolff*, 2000]. The conductivity given by Equation (19) is normalized to the reference temperature -15°C. However, different molar conductivity coefficients have also been derived in other coring sites, sometimes using a different reference temperature [*Moore et al*., 1989; *Barnes et al*., 2002].

The proportionality between the high frequency conductivity and the ionic concentration found in meteoric ice is conceptually similar to that found in laboratory-grown ice doped for the low concentration and high temperature range (cf. section 5.2). However, quantitatively the measurements on laboratory-grown and meteoric ice are in disagreement and seem to suggest that Bjerrum defects are more numerous in polar ice than in artificial ice [*Takei*,

Accepted Article

© 2015 American Geophysical Union. All rights reserved.

2007]. If this difference is explained within the framework of Jaccard theory, this pattern suggests it could be claimed that the impurity partition is more effective in meteoric than in laboratory-grown ice [*Moore et al*., 1992; *Stillman et al*., 2013b]. Indeed, it has been shown that the dielectric properties of ice samples derived from polar ice core that has been melted and refrozen are similar to those of laboratory-grown ice [*Takei*, 2007]. However, it cannot be ignored that the growth process underlying ice formation, which is very different in natural and artificial conditions, has a strong impact on the mechanisms that control the distribution and location of impurities as well as on the total number of ions incorporated in the ice lattice. Moreover, the properties of natural ice are affected by structural imperfections, gas bubbles and/or clathrate hydrates [*Takei*, 2007] and are subject to change over time due to post-depositional and re-crystallization processes [*Kulessa*, 2007], annealing and aging [*Reynolds*, 1985] and impurity displacement and transport [*Rempel et al., 2002*].

6.2 Sea ice

As described in section 3.2, sea ice is a multiphase structure composed of ice Ih crystals, gas, liquid brine, solid salts, and other impurities. As a result its electric properties are quite variable and, for natural samples, can be strongly site-specific. For this reason it is difficult to associate unambiguous values to the permittivity and conductivity of sea ice. The literature reports a variety of dielectric measurements conducted on sea ice in different experimental conditions, such as temperature interval, frequency range, salinity percentage, aging and growing mechanism (see e.g., *Vant et al*., [1978]; *Hallikanien and Winebrenner* [1992]). The experimental procedure to prepare and measure both natural and laboratory grown sea ice samples is complex [*Addison*, 1969]. For example, in natural ices, when a piece of ice is cut from a larger mass, brines could drain from the sample and prevent a correct measurement of the bulk dielectric properties [*Addison*, 1969]. On the other hand, there is always an uncertainty in how well laboratory grown sea ice is able to reproduce the electrical properties of natural sea ice [*Ingham et al.*, 2012]. *Fujino* [1967] measured the complex permittivity of two sea ice samples between 268 K and 203 K in the frequency range 100 Hz-50 kHz. The first sample was a natural "mosaic" ice, sealed in a box to limit brine drainage, while the second was a "granular" ice obtained by pouring synthetic brines, at freezing temperature, on a sample of snow. In spite of the different origins, the two samples showed a similar dielectric behavior consisting of two abrupt changes in the trends of permittivity and conductivity versus temperature. The first change occurs at the NaCl eutectic temperature (about 250 K), when the salt starts to precipitate in the brine and produce a mixture of liquid

© 2015 American Geophysical Union. All rights reserved.

Accepted Article

and solids. The second change takes place at the temperature (about 218K) where the entire brine salt content turns into a solid eutectic mixture. Below this temperature liquid brine does not exist anymore. In this study, *Fujino* [1967] also found two anomalous frequency dispersion regions. The first, at low frequencies, was attributed to the migration of ions within the brine channels, which produces a DC conductivity and an ion-space charge polarization. The second, at higher frequencies, was associated to the Debye relaxation of protons in the ice. *Addison* [1969; 1970], using artificial samples of sea ice, studied a wider range of frequency and temperature values (up to 100 MHz and down to 123 K), finding similar relaxation phenomena reported by *Fujino* [1967]. In addition, the author identified a further dispersion mechanism in the MHz region and interpreted such phenomenon using the Maxwell-Wagner-Sillars model [*Sillars*, 1937], which combines the electrical properties of the brine cells with those of the ice matrix. The three dispersion mechanisms, at different temperatures, are illustrated in Figure 12.

Vant et al. [1978] carried out an extensive study at higher frequencies (100 MHz - 40 GHz), performing electric measurements on both artificial and natural sea ice (first- and multi-year ice) as well as an in-depth analysis of various empirical models. The authors concluded that the dielectric behavior of sea ice is well described by the *Tinga et al*. [1973] mixing rule. A modification of this model was proposed afterwards by *Morey et al*. [1984] and *Arcone et al*. [1986], who introduced an additional term, due to bulk DC conductivity, to take into account the hydraulic permeability between the various brine pockets.

6.3 Marine ice

Marine ice electrical properties have only been studied by *Moore et al*., [1994b]. The ice core was collected in the Ronne Ice Shelf (Antarctica) and the analyses were performed on samples extracted at four different depths (from 154 m to 197 m). The salinity of the melt-water ranged from $0.076‰$ to $0.024‰$ which, as discussed in section III, is intermediate between meteoric and sea ice. The authors measured the dielectric properties of the samples at 251 K and found σ_∞ on the order of 100 μS m^{-1}. Figure 13 illustrates these results (open squares) together with conductivity data collected on meteoric and sea ice samples. The figure shows that only two marine ice samples are fitted by the linear regression of the low salinity data (meteoric ice), whereas the other two significantly deviate from such trend. The authors argue that the dielectric behavior of the two low salinity samples is in agreement with that of meteoric ice as the Cl^- ions are incorporated in the ice lattice, producing L-defects. In

© 2015 American Geophysical Union. All rights reserved.

Accepted Article

contrast, the dielectric behavior of the other two samples could be explained by the fact that the Cl^- concentration is above the solubility limit, thus causing the ions to also concentrate at the grain boundaries.

Finally, Figure 13 highlights the fact that meteoric and sea ice belong to two different populations, characterized by conductivities (or attenuation) which differ by almost three orders of magnitude.

VII DIELECTRIC PROPERTIES OF HYDRATES AND ICY MIXTURES

7.1 Clathrate hydrates

As discussed in depth in sections 5.1 and 5.2, pure ice Ih follows a Debye relaxation model as the reorientation of the water molecules proceeds with only a single relaxation time. Conversely, clathrate hydrates show a slightly different dielectric behavior, better described by a Cole-Cole model [*Cole and Cole*, 1941], which exhibits a larger dispersion bell-shaped curve due to a continuous distribution of relaxation times. Dielectric properties of clathrate hydrates have been studied since the early 1960s, in comparison with those of ice Ih and sometime those of ice Ic. However, type II clathrate hydrates have been better characterized than type I because the latter have, in general, more volatile guest molecules and thus are difficult to accurately measure [e.g., *Davidson*, 1973; *Gough et al*., 1973; *Davidson et al*., 1977; *Davidson and Ripmeester*, 1978; *Murthy*, 1999]. Both types of clathrate hydrates have a region of dielectric absorption in the audio-frequency range, which can be ascribed to the freezing of re-orientational motion of the water molecules; however, the departure of the dispersion-absorption curve from the Debye model is usually small in type II and much broader in type I [*Davidson*, 1973]. Interestingly, even though the two types of clathrate hydrates are clearly distinguishable on the basis of their absorption and dispersion curves, they have similar ε_s and ε_∞ values (see Table 6).

In particular, the static permittivity follows the typical 1/T trend, and it is quite smaller (about 60 at 243 K) than that of ice Ih, probably due to the lower density of the clathrates [*Rick and Freeman*, 2010]. The high frequency value, in case of nonpolar guest molecules, is comparable (about 2.9 at 243 K) with that of ice Ih, whereas it becomes higher if the guest molecules are polar (see Table 6). Moreover, the "mean" relaxation frequency of the clathrate hydrates is only slightly higher than that of ice Ih when the guest molecules are nonpolar, but

© 2015 American Geophysical Union. All rights reserved.

Accepted Article

increases significantly in the case of polar guests (see Figure 14), as such molecules introduce additional Bjerrum defects in the surrounding ice lattice. Moreover, it has been shown that oxygen-containing guests shorten the relaxation time of the host clathrate hydrates by three orders of magnitude and reduce its activation energy by almost a factor of two [*Alavi et al*., 2010 and reference therein]. The presence of dipolar guest molecules in the clathrate hydrates modifies the overall dielectric spectrum, adding a second region of dielectric dispersion and absorption associated with the much faster reorientation of such molecules [*Gough et al*., 1973]. In practice, ε_∞, which is the high-frequency side of the dispersion region associated with reorientation of the water molecules, corresponds to the static permittivity of the dispersion associated with the reorientation of the dipolar guest molecules. The relaxation frequency of dipolar guests like CO, H_2S [*Davidson et al*., 1977; *Davidson et al*., 1987] and SO_2 [*Gough et al*., 1983], which reorient extremely quickly, falls in the MHz region at very low temperatures (tens of kelvins) but moves in the GHz range or higher above about 60 K [*Gough et al*., 1973].

The types of clathrate hydrates that have been hypothesized to be present in the Galilean icy satellite crusts, and especially on Europa, are SO_2, CO_2, H_2S and CH_4 [*Prieto-Ballesteros et al*., 2005] and O_2 [*Hand et al*., 2006]. To our knowledge, no specific data have been published on the dielectric properties of such clathrate hydrates, however their dielectric behavior can be inferred from the general properties described above. Thus we can expect that nonpolar guest molecules, like O_2, CH_4 and CO_2, should only weakly affect the dielectric behavior of the overall clathrate structure, slightly increasing the relaxation frequency with respect of that of pure water ice. On the other hand, the presence of polar guests like H_2S and SO_2 should significantly increase the relaxation frequency of the clathrate hydrates.

7.2 $MgSO_4$ and Na_2SO_4 hydrates

Magnesium and sodium sulfate hydrates have always played an important role in the theoretical considerations regarding the composition of the jovian icy satellites [e.g., *Kargel*, 1991; *Kargel et al*., 2000]. The subsequent experimental confirmation made by NIMS [*McCord et al*.,1999; *McCord et al*., 2001; *Dalton*, 2003; *Dalton et al*., 2005] gave further strength to this hypothesis, even if there is still no full agreement on the interpretation of the spectra [*Dalton et al*., 2010; *Brown and Hand*, 2013 and references therein]. Based on the issues discussed in section 5.5, it can be expected that neither $MgSO_4$ nor Na_2SO_4 have the chemical characteristics to enter the ice lattice in substitution of water molecules, thus they

© 2015 American Geophysical Union. All rights reserved.

should aggregate in the ice only as inclusions.

The equilibrium phase diagram (at *P=1* atm) of the binary system $MgSO_4$-H_2O [*McCarthy et al*., 2007; *Fortes and Choukroun*, 2010] shows that magnesium sulfate has multiple levels of hydration and can form four hydrated salts in equilibrium with an aqueous solution, each having a unique crystal structure (see Table 7). Similarly, the equilibrium phase diagram of the binary system Na_2SO_4-H_2O shows that Na_2SO_4 has multiple levels of hydration, with two stable hydrates and one (heptahydrate) metastable hydrate (see Table 7) [*McCarthy et al*., 2007; *Fortes and Choukroun*, 2010].

The dielectric behavior of $MgSO_4$ and Na_2SO_4 (pure or hydrated) is poorly known, as very few data have been published so far. However, some experimental values, measured at about 300 K in the kHz-MHz range, can be found in a series of papers published by *Borel* [1893], *Voronkov* [1958], *Burton and Turnbull* [1937], *Cheng* [1939], *Roberts* [1949] and *Kamiyoshi and Miyamoto* [1950]. In addition, the studies performed by *Cheng* [1939] and *Kamiyoshi and Miyamoto* [1950] suggest that the real part of permittivity in a composite material like a hydrate salt can be estimated as follows:

$$\varepsilon_{\mathrm{hd}} = \frac{2P_{\mathrm{a}} + 2nP_{\mathrm{w}} + \left(M_{\mathrm{hd}} / \rho_{\mathrm{hd}}\right)}{\left(M_{\mathrm{hd}} / \rho_{\mathrm{hd}}\right) - P_{\mathrm{a}} - nP_{\mathrm{w}}} \qquad (20)$$

where $P = \frac{\varepsilon - 1}{\varepsilon + 2}\frac{M}{\rho}$ is the Clausius-Mosotti equation for the molar polarizability, *M* the molecular weight, ρ the density and *n* the hydration number. The suffixes a, w and hd refer to the anhydrous phase, the water of crystallization and the hydrate phase, respectively. Figure 15 shows the permittivity estimated with Equation (20) for the hydrate sulfates of Table 7, together with the data available in the literature. The values of $\varepsilon_{\mathrm{hd}}$ have been calculated using the data reported in *Kamiyoshi and Miyamoto* [1950]: $P_{a_{\mathrm{MgSO_4}}} = 29.60 cm^3$ ($\varepsilon_{a_{\mathrm{MgSO_4}}} = 6.67$), $P_{a_{\mathrm{Na_2SO_4}}} = 36.70 cm^3$ ($\varepsilon_{a_{\mathrm{Na_2SO_4}}} = 7.90$), $P_{\mathrm{w}} = \left(8.62 \pm 0.13\right) cm^3$ ($\varepsilon_{\mathrm{w}} = 3.75 \pm 0.07$).

Both estimated and experimental values, reported in Figure 15, clearly show that the permittivity decreases with the hydration number.

7.3 Dirty ice

Besides the effects of the soluble chemical impurities, ice electrical properties are also affected by the presence of mineral grains mechanically trapped in the polycrystalline

© 2015 American Geophysical Union. All rights reserved.

structure. This type of ice, usually called dirty ice, is uncommon on Earth as the amount of grain content in meteoric ice is negligible (usually lower than 1%) [*Petit et al.,* 1999]. Conversely, dirty ice is common in planetary exploration, as demonstrated by recent measurements on the Martian polar caps [*Plaut et al*., 2005 *Li et al., 2012*] and by observations performed on the icy Galilean satellite surfaces [*Moore et al*., 2004; *Pappalardo et al*., 2004]. The literature on dielectric measurements of dirty ice analogs is fairly limited and relatively recent. In the framework of the Rosetta mission, the dielectric properties of mixtures of ice and dunite, montmorillonite and kaolinite (with a maximum dust mass fraction of 25%) were measured by *Herique et al*. [2002]. The scope of the work was to predict the radio wave velocity inside comet-like materials. The authors measured real and imaginary parts of permittivity on dry and frozen samples as a function of temperature (77-350 K) and at specific frequencies (0.12, 1.2 and 12 kHz). They extrapolated the results at the operating frequency of CONSERT (90 MHz), finding a different dispersive behavior at high and low temperatures. Above about 200 K the bulk permittivity exhibits a significant dispersion and it is dominated by the ice. Below this temperature the bulk permittivity is substantially frequency independent, it is dominated by the grain density and, to a lesser extent, by their mineral composition.

Stillman et al. [2010] measured the electrical properties of ice silicate/salt mixtures with different volume fractions as a function of temperature (180-298 K) and frequency (1 mHz – 1 MHz). They found a complex spectrum with five dielectric relaxation frequencies associated with different physical mechanisms. In particular, at the lowest temperature (181 K) they observed a first relaxation, due to the dipole reorientation process of adsorbed water (at 630 kHz), and a second one associated with the rotation of L-defects (at 200 Hz). Moreover, they identified two Maxwell-Wagner effects, one due to interfacial polarization within adsorbed water (at 10 Hz) and another produced by polarization between salt hydrates and silicates (at 10 mHz). Finally, a further low frequency dispersion was observed in samples at low water content.

Heggy et al. [2012] measured cometary analogs (ice/chondrites mixtures) with porosities from 20% to 50% as a function of frequency (1 MHz-1 GHz) and temperature (113-298 K). Their data indicate that the real part of permittivity increases with temperature, however the results were not conclusive for the imaginary part, as it was too low to be measured. As expected, the authors also found a dependence of complex permittivity on bulk density and retrieved the following empirical equation for the real part $\varepsilon' = 2.2^{\rho_{bulk}}$ (with ρ_{bulk} expressed

© 2015 American Geophysical Union. All rights reserved.

Accepted Article

in g cm^{-3}). Furthermore, to overcome the lack of experimental data in the imaginary part, *Heggy et al*. [2012] applied the Maxwell-Garnett rule [*Sihvola*, 1999] to determine the dependence of this quantity on dust content ($\varepsilon'' = 2.3\times10^{-3}\, e^{1.17\rho_{bulk}}$).

In order to evaluate the attenuation of radar signals in martian polar terrains, *Mattei et al*. [2014] studied the effect of basalt dust in ice, measuring the complex permittivity versus temperature (150-250 K) and frequency (20 Hz - 1 MHz) of dry basalt dust, pure ice and two different ice/basalt mixtures (11% and 43% dust fractions). The results show that the $\varepsilon'(\nu)$ spectrum of the mixtures is very similar to the one of pure ice, approaching a high frequency value of $\varepsilon_\infty = 3.5$ and $\varepsilon_\infty = 5.0$, respectively. On the other hand, the imaginary part exhibits a more complex behavior (see Figure 16): at low frequencies and high temperatures the $\varepsilon''(\nu)$ spectra resemble that of pure ice, whereas at high frequencies and low temperatures they tend to flatten and converge towards the values of the dry material. This behavior suggests that the imaginary part of dielectric permittivity is approximately a linear combination of those of ice and basalt grains.

VIII DIELECTRIC PROPERTIES OF NON-WATER ICES

8.1 Solid CO_2

CO_2 ice is common in the Galilean satellites and could be generated from internal degassing (as in Callisto) or from radiolytic and photolytic reactions involving carbonaceous material in water ice [*Dalton et al*., 2010 and references therein]. It is not clear, however, if it can be present in the icy crusts as a pure phase, enclathrated in water ice or adsorbed on other species, or some combination of all three. CO_2 is the simplest form of linear triatomic molecules abundant in nature. At low pressures and temperatures, CO_2 condenses as a molecular solid in the cubic structure (known as dry ice, phase I), which is characterized by strong double bonds ($C{=}O$ distance of 1.16 Å) and rather weak intermolecular interactions.

The literature on the dielectric behavior of CO_2 ice in the MHz-GHz range is very limited. *Pettinelli et al*. [2003] conducted laboratory experiments on solid CO_2 (ice, snow and powder) in both the frequency and time domains. The measurements in the frequency domain (20 Hz - 1 MHz) were performed using a capacitive cell filled with CO_2 ice powder and connected to an impedance analyzer (LCR meter). The measurements in the time domain, corresponding to a frequency band of 100-1000 MHz, were conducted using a transmission

© 2015 American Geophysical Union. All rights reserved.

Accepted Article

line inserted in solid CO_2 ice, snow or powder, and connected to a cable tester (Time Domain Reflectometry - TDR). The low frequency results highlighted the nonpolar behavior of CO_2 ice powder, as the real part of the permittivity was found to be very low (about 1.4) and constant across the entire frequency range. Moreover, the low conductivity ($10^{-9} - 10^{-7}$ S m^{-1}) found in the same range also underlines the low-loss character of the material. The low values of the real part of permittivity measured for CO_2 powder (and CO_2 snow) were confirmed by TDR measurements, as shown in Table 8. This table compares the values found by *Pettinelli et al*. [2003] with those reported in *Simpson et al*. [1980], who measured samples of CO_2 powder as a function of density within the microwave frequency range of 2.2–12 GHz. Taking into account the difference in sample densities, the agreement between the two sets of measurements is significant, also in the case of the solid CO_2 ice sample, which was measured in *Pettinelli et al*. [2003] and estimated using the Maxwell-Garnett mixing formula in *Simpson et al*. [1980]. Moreover, *Simpson et al*. [1980] also found an upper limit of the loss factor $\tan\delta = 0.005$. Combining the results of these two experimental studies it is possible to argue that the dielectric behavior of CO_2 ice is affected by the sample density, but it is essentially independent of frequency in a large band extending from high frequency to microwaves. Finally, more recently *Paillou et al*. [2008] measured a sample of solid CO_2 (of unspecified density) in a resonant cavity at 10 GHz, obtaining a lower value than those shown in Table 8 for the real part of permittivity ($\varepsilon = 1.55$) but a comparable value with that reported by *Simpson et al*. [1980] for the loss tangent ($\tan\delta = 0.002$).

8.2 Solid NH_3

Ammonia is a very efficient "anti-freezing" chemical compound, and its presence has been hypothesized to explain phenomena such as cryovolcanism. It also plays a fundamental role in justifying the presence of an ocean below the Ganymede and Callisto icy crusts (see e.g., *Spohn and Schubert* [2003] and literature therein). Several condensed hydrogen-bonded molecular phases of ammonia have been identified at low temperatures: a fluid phase, two rotationally disordered solid phases (II and III), and three low-temperature fully ordered crystalline phases (I, IV and V). The low temperature and pressure phase I has a cubic structure and undergoes phase transitions into phase IV (orthorhombic structure) between 3 and 4 GPa. Phases I and IV are compatible with the range of pressures (0-5 GPa) and temperatures (100-300 K) typical of the Galilean icy satellites. However, as water ice is the

© 2015 American Geophysical Union. All rights reserved.

predominant solid ice phase in both Ganymede and Callisto, ammonia is most likely to be stable as ammonia dihydrate ($NH_3 \cdot 2H_2O$) or monohydrate ($NH_3 \cdot H_2O$) [*Fortes and Choukroun*, 2010].

To our knowledge only one paper on the dielectric properties of pure NH_3 ice has been published to date [*Smyth and Hitchock*, 1934], which reports the values of the real part of permittivity and conductivity vs. temperature (87-194.1 K) and frequency (0.3, 1, 5, 60 kHz). Results indicate a slight increase with temperature and a slight decrease with frequency of the real part of permittivity, with ε' ranging between 3.36 and 4.83. On the other hand, the measurements show that the conductivity exhibits a weak increase with frequency and a weak decrease with temperature, with values lower than 0.1×10^{-9} S m^{-1} in the temperature range 87.0-150.2 K (for all frequencies), and values of 3.5×10^{-9} S m^{-1} (at 0.3 kHz) and 8.4×10^{-9} S m^{-1} (at 60 kHz) near the melting point (194.1 K) (for details see *Smyth and Hitchock* [1934]). The authors, in analogy to the behavior of pure water ice, attributed the slight frequency dispersion measured in their solid sample, as well as the high conductivity value measured in the liquid phase ($\varepsilon = 25, \sigma = 5.5\times10^{-6}$ S m^{-1}), to a small amount of ionic impurities present in the NH_3 sample, concluding that there is no dipole rotation in solid ammonia.

The dielectric behavior of frozen, highly concentrated water-ammonia solutions has been investigated at low frequency (near DC and at about 1 MHz) by *Lorenz* [1998] and in the microwave range by *Lorenz* [1999], *Lorenz and Shandera* [2001] and *Paillou et al*. [2008]. The measurements performed by *Lorenz* [1998] where conducted on several samples of water-ammonia ices (from a few percent to 30% of ammonia) frozen with liquid nitrogen at a temperature of about 77 K (see details in *Lorenz* [1998]). The real part of permittivity was estimated at 12 Hz and 0.6 MHz using a standard capacitance technique and the imaginary part in the kHz range using a Vector Network Analyzer (VNA). The results of these measurements can be considered semi-quantitative as they are affected by large uncertainties (10% on the real part of permittivity and 20% on the imaginary part) and several calibration problems, and thus, as highlighted by the author, are only indicative of the dielectric behavior of water-ammonia ices. Nevertheless, the data show that the real part of permittivity increases with ammonia concentration (from 3.1 for 0% to 4.5 for 30%), and that a similar trend is also visible in the imaginary part of permittivity (see Figure 3a in *Lorenz* [1998]), especially in the values collected at higher frequencies. In the microwave range, the dielectric parameters of water-ammonia ice have been estimated by *Paillou et al*. [2008] using the resonant cavity

© 2015 American Geophysical Union. All rights reserved.

Accepted Article

method (at 10 GHz). The authors measured the complex permittivity of several samples (at a temperature of about 77 K), doubling the ammonia concentration in each sample (from 1.7% to 28%). The reported values confirmed the behavior observed at lower frequency by *Lorenz* [1998], with an increase from 3.13 to 4.38 in the real part and from 0.0013 to 0.0042 in the imaginary part as a function of the ammonia concentration. It is worth noting that *Paillou et al*. [2008] also calculated the loss tangent of their ammonia-rich ice samples, obtaining values lower than 10^{-3}, which are much smaller than those previously estimated from calorimetric data acquired using a microwave oven [*Lorenz*, 1999; *Lorenz and Shandera*, 2001].

IX RADIO-WAVE PROPAGATION IN THE ICY CRUSTS OF JOVIAN SATELLITES

9.1 Estimated wave parameters

The information on the dielectric behavior of the various types of ice reviewed in the previous sections, and specifically on ε_∞ and σ_∞, is the starting point from which the radio wave parameters can be calculated (cf. section 4.2). Regardless of the GPR characteristics, once the radar signal has "entered" the subsurface, maximum penetration depth, vertical resolution and time depth of the interfaces all depend on the dielectric properties of the subsurface materials. Using the data available from the discussions above (but neglecting the volumetric scattering effects which are beyond the scope of this review) we have attempted to determine the electromagnetic wave parameters affecting the fate of the radar signal. Figure 17 reports the attenuation rate α(dB/km) vs. 1/T (or T on the top axis of the graph) for different materials, calculated at 9 MHz and 60 MHz, i.e., the operating frequencies of RIME and Europa Clipper, using Equation 6 and plotted in the 270-150 K interval. It should be noted that since the literature data are heterogeneous in terms of measured temperature intervals and frequency ranges, and very few data refer to temperatures below 200 K or frequencies above 1 MHz, therefore some assumptions have been made; these assumptions are described in detail in the following. For CO_2 ice we used the permittivity data at 10 kHz and about 195 K [*Pettinelli et al*., 2003] and we assumed that such values are valid at 9 MHz and 60 MHz and are constant over the entire temperature range. For dirty ice we applied the Bruggeman mixing formula [*Sihvola*, 1999] to *Mattei et al*. [2014] data to estimate the permittivity of the dust, then we used this data together with *Auty and Cole* [1952] pure water

© 2015 American Geophysical Union. All rights reserved.

Accepted Article

ice data to estimate the complex permittivity of an icy mixture with 11% of dust. For pure water ice, doped ice (with HCl and NH_3) and nonpolar guest clathrate hydrate we assumed a single Debye relaxation process and used Equation 3 to estimate the real and imaginary parts of the permittivity of the various ices, starting from the data reported in *Auty and Cole* [1952], *Kawada* [1978], *Gross et al.* [1978] and *Davidson* [1973]. Note that for HCl doped ice, we used the data with the concentration of HCl at its solubility limit. For the NH_3 ice we extrapolated the data measured at 60 kHz [*Smyth and Hitchcock*, 1934] to 9 MHz and 60 MHz, assuming a conductive behavior for the imaginary part and a constant value for the real part. Finally, to estimate the attenuation of sea ice we used the data reported in Figure 12, on the basis of the measurements performed by *Addison* [1969] on a 5.12% salinity ice sample (cf. section 6.2).

Accounting for the assumptions made, several interesting conclusions can be drawn from an analysis of Figure 17. First of all, for some materials (CO_2 ice, dirty ice and sea ice) the attenuation is frequency-dependent. As a consequence, for each of them the curves at low and high frequencies are distinct, whereas for the other materials the curves at 9 MHz and 60 MHz coincide. As expected, among all materials reported in the graph, pure water ice is the most transparent over the whole temperature range. For temperatures above about 220 K the different data (i.e., *Auty and Cole* [1952] and *Kawada* [1978]) are in agreement, however below this temperature the values measured by *Kawada* [1978] progressively diverge from the perfectly linear trend of *Auty and Cole* [1952] (cf. Figure 10). Also the attenuation trend of NH_3 doped ice and nonpolar guest clathrate hydrate does not deviate significantly from that of pure water ice. The former is in agreement with the experimental evidence discussed in section 5.5 which indicates that NH_3 does not increase σ_∞, and the latter is in agreement with the behavior expected for a nonpolar guest clathrate hydrate, as discussed in section 7.1. Regarding NH_3 ice, it is interesting to note that despite the limited amount of experimental data available to compute α, the attenuation trend is clearly recognizable. In the temperature interval where the ammonia data are present, which starts below 200 K as the freezing point of ammonia at *P=1* atm is about 195 K, the attenuation of this type of ice is always larger than those of pure water ice, NH_3 doped ice and nonpolar guest clathrate hydrate. The estimated attenuation for CO_2 ice and dirty ice is relatively high and becomes the highest at low temperatures, due to their temperature-independent nature. Finally, the attenuation of HCl doped ice and especially that of sea ice and polar guest clathrate hydrate is remarkably high, being three orders of magnitude larger than that of pure water ice, and significantly

Accepted Article

© 2015 American Geophysical Union. All rights reserved.

decreases when the temperature drops.

Using the data on the high frequency real part of permittivity reported in the literature it is possible to also estimate radio wave velocity (applying Equation (7)) and maximum vertical resolution (applying Equation (8)). These calculated values are reported in Table 9, where the vertical resolution has been computed for the 9 MHz RIME antenna (bandwidth 1 MHz and 3 MHz) [*Bruzzone et al*., 2013] and for the 9 MHz and 60 MHz Europa Clipper antennas (bandwidth 3 MHz and 10 MHz) [*Grima et al*., 2013]. As expected, the vertical resolution in the same type of material is higher for larger bandwidths; on the other hand for a fixed bandwidth the resolution increases with permittivity of the material.

9.2 Radar equation

The dielectric properties and wave parameters can be used to produce realistic electromagnetic models of the jovian satellites icy crusts or, alternatively, once the radar data have been acquired, to invert such data and extract some information on the geological nature of the subsurface, as attempted by several authors for the Moon and Mars in past and ongoing missions [e.g., *Porcello et al.*, 1974; *Picardi*, 2004; *Zhang et al*. 2008; *Campbell et al*., 2008; *Lauro et al*. 2010; *Lauro et al*. 2012]. The returned power $P_r(z)$ from a buried interface, smooth and flat relative to the wavelength of the radio wave (horizon) and located at *z* depth inside the planetary crust, depends on several parameters as follows [*Gudmundsen*, 1971]

$$P_r(z) = \frac{R(z)\ A(z)\ B(z)\ \Psi(z)}{\left[2\left(H + z/\sqrt{\bar{\varepsilon}(z)}\right)\right]^2} P_e \qquad (21)$$

In this equation, $R(z)$ represents the reflectivity which, as discussed in section 4.2, is a function of the dielectric contrast between two adjacent layers, and $A(z)$ is the two-way attenuation along the propagation path given by $A(z) = e^{-2\int_0^z \alpha(z')dz'}$ where $\alpha(z)$ is the attenuation coefficient defined in Equation (6). Moreover, $B(z)$ accounts for the birefringence and $\Psi(z)$ is the total transmission (two-way path) after multiple reflections due to internal layers. The term $\left[2\left(H + z/\sqrt{\bar{\varepsilon}(z)}\right)\right]^2$ is the geometric spreading, which depends on the spacecraft altitude *H*, the depth *z* and the depth-averaged permittivity $\bar{\varepsilon}(z)$; for an orbiting GPR at a fixed *H*, such a term can be considered constant ($\cong 4H^2$) as $H >> z$. Furthermore, P_e is the irradiated effective power corrected for the system gain (azimuth and range compressions). In airborne GPR data acquired on polar ices, the term $B(z)$ is usually

© 2015 American Geophysical Union. All rights reserved.

assumed to be depth-independent [*Matsuoka et al.*, 2010], the geometric spreading is considered constant and the transmission coefficient $\Psi(z)$ approximately unity [*MacGregor et al.*, 2007]. Thus, assuming that the same approximations hold for the data acquired on jovian satellite icy crusts, Equation (21) can be simplified as

$$P_r(z) \propto R(z)\, A(z)\, P_c \qquad (22)$$

where P_c is the irradiated power corrected for the geometrical spreading and the birefringence factor. Equation (22) shows that, besides the evaluation of P_c, the reflected power depends on the attenuation $A(z)$ and the reflection coefficient $R(z)$, which are functions of the physical and geological properties of the subsurface.

9.3 Radar signal attenuation

To our knowledge, very few papers have been dedicated to model the radar response in the crust of the jovian satellites; and they are all devoted to study the interior of Europa, under the assumption that an orbiting GPR would be operating at 50 MHz. This frequency represents the best tradeoff between the effect of Jupiter's radiation noise and signal attenuation in the icy crust. However, in the case of RIME, a lower operating frequency of 9 MHz was chosen to maximize the probability to detect deep subsurface structures, while minimizing the effect of surface roughness. The consequent higher radio noise from Jupiter will be avoided by acquiring data only on the anti-jovian side of the icy satellites [*Bruzzone et al.*, 2013]. The Europa Clipper radar will consist of both a 9 MHz antenna and a second antenna at 60 MHz .

Chyba et al. [1998] first estimated radar signal attenuation in the europan subsurface, assuming different thermal profiles within the crust (conductive and convective). The authors estimated the electrical properties of the icy crust by applying the Maxwell-Garnett mixing formula to a mixture of pure ice and lunar soil at different volume fractions (1%, 10%, 50%), finding, in the most favorable case (i.e., 1% volume fraction), a detectability limit of the ice/ocean interface at about 10 km. Subsequently, *Moore* [2000] and *Blankenship et al*. [2009] modified this model, using the lowest concentration (1% volume fraction) suggested by *Chyba et al*. [1998] but substituting the lunar soil with salt grains.

The authors simulated the structural and dynamical properties of the europan crust in three geologically plausible scenarios (see Figure 18, left panel). The first model (a) considers a thin conductive shell composed of "marine-like" ice subjected to accretion/ablation processes at the bottom of the crust (Figure 18). The second model (b) considers a thicker conductive

© 2015 American Geophysical Union. All rights reserved.

Accepted Article

shell, composed of salty ice overlying a thin layer of brine-rich sea ice, which is subject to tectonic processes capable of generating crustal features associated with rapid freezing of water injected along cracks [*Greenberg et al*., 1998]. The third scenario (c) depicts solid-state convection in the icy crust [*McKinnon*, 1999]; in this model a conductive stagnant lid of salty ice overlies a convective cleaner and warmer ice, similar to terrestrial sea ice, in which the impurities have been segregated downward in brine pockets [*Pappalardo and Barr*, 2004]. Figure 18 (right panels) also illustrates the attenuation rate (at 50 MHz) associated with the various scenarios, which has been estimated using different electromagnetic properties for each layer, as described in of *Moore* [2000]. The third scenario has also been studied by *McKinnon* [2005], who estimated radar signal attenuation in cold/hot convective plumes made of dirty ice (with different percentages of silicates), assuming weak convection near the convective instability threshold [*McKinnon*, 1999]. The results of that work highlight that radar signal propagation into the cold down-welling part is favored with respect to that in a pure conductive shell (Figure 19).

Similar results were found by *Di Paolo et al*. [2014], who evaluated the detectability of a liquid ocean buried beneath a 10 km thick convective icy crust, considering a 9 MHz radar signal. The authors computed the reflected power from the ice/ocean interface in seven different thermal scenarios (Figure 20), from hot up-welling (1) to cold down-welling (7), confirming that the detection of the ocean is possible only near the cold plume. In addition, *Di Paolo et al*. [2014] suggested that a sharp interface between dusty and pure ice could be detected on Ganymede and Callisto in the first few kilometers.

9.4 Dielectric targets

On Earth, three major mechanisms control the radio wave internal reflections inside the polar ice sheets. In the first few hundred meters, where air bubbles are present, the dominant cause of radar reflections is the contrast in density which, as discussed in section 5.3, affects the real part of permittivity. At greater depths, contrast in chemical impurities (σ contrast) and in the alignment of the ice fabric in the polycrystalline structure (ε' contrast), which is quantified by the COF [*Hargreaves*, 1978; *Fujita and Mae*, 1994], becomes predominant [*Fujita et al*., 1999; *Siegert and Kwok*, 2000; *Matsuoka et al*. 2003]. On the icy satellites, reflectors similar to those described above for terrestrial ices can be associated with different geological features. Dielectric interfaces due to compositional contrasts could be generated by thermal segregation of impurities (such as salts and/or acids) associated with present or

© 2015 American Geophysical Union. All rights reserved.

Accepted Article

past convective/tectonic processes, such as those proposed to explain chaos terrains on Europa [*Collins et al*., 2000; *Pappalardo and Barr*, 2004; *Collins and Nimmo*, 2009]. Moreover, several dielectric features could also be associated with buried impact craters [*Blankenship et al*., 2009]: i) a blanket of ejecta (eventually in multiple overlapping layers) covering the old surficial material; ii) solidified eutectics associated with rapid melting/freezing due to the impact; and iii) impact related structures like crater basins. On Ganymede and Callisto, a dielectric interface could be associated with the geological contact between a silicate-rich regolith layer (possibly related to sublimation degradation and/or mass wasting phenomena [*Moore et al*., 1999]) and the underlying cleaner ice substrate [*Prockter et al*., 1998]. The thickness of such a layer is still unknown but some authors estimated a regolith thickness of few to some tens of meters [see e.g., *McKinnon and Parmentier*, 1986].

Dielectric interfaces related to abrupt changes in COF [*Barr and Stillman*, 2011] could be caused by the strain related to solid-state convection [*Goldsby and Kohlstedt*, 2002]. On Europa, horizons between regions with different orientation fabrics could be present within the stagnant lid and in the cold down-welling [*Barr and Stillman*, 2011]. The COF could be connected to the Brittle-Ductile Transition (BDT) within the ice shell. On Europa such a transition is expected to be at a depth between hundreds of meters and a few kilometers [*Williams and Greeley*, 1998; *Nimmo et al*., 2003; *Hurford et al*., 2005; *Nimmo and Schenk*, 2006], on Ganymede a relic BDT is thought to be located at a depth of about 2-3 km [*Golombek and Banerdt*, 1985, 1986; *Collins et al*., 1998; *Dombard and McKinnon*, 2001; *Nimmo et al*., 2002*; Nimmo and Pappalardo*, 2004] and on Callisto down to several kilometres [*Golombek and Banerdt*, 1986 *McKinnon*, 2006]. Recently, *ElShafie and Heggy* [2013] performed measurements of the mechanical strength of ice in connection to the estimation of the permittivity, estimating the depth of the BDT to be about 5-6 km for Europa and 60-100 km for Ganymede. *McCarthy et al*. [2011] also performed experiments on the mechanical properties of ice Ih and on an ice Ih/meridianite eutectic mixture, highlighting that for a crust composed of salty ice the BDT is not sharp with a transition to a semi-brittle rheology.

On Europa dielectric interfaces could also be associated with the boundary between ice and water lenses of eutectic mixtures, fluids in fractures, brine pockets and refrozen brines, possibly present at a depth of a few kilometers beneath the chaotic regions and ridges [*Collins and Nimmo*, 2009; *Schmidt et al*., 2011; *Walker and Schmidt*, 2015] or in warm ice close to the ocean/ice interface [*Chyba et al*., 1998].

Finally, a strong dielectric reflector should be associated with the ice/ocean interface which,

© 2015 American Geophysical Union. All rights reserved.

Accepted Article

on Europa, is supposed to be located at a depth within a few tens of kilometers [*Pappalardo et al*., 1998]. On Ganymede this interface is assumed to be deeper than 150 km [*Kivelson et al*., 2002; *Sotin and Tobie*, 2004; *Kuskov and Kronrod*, 2005; *Seufert et al*., 2011], even though such a value could be reasonably reduced to 60-80 km by the presence of ammonia in the water [*McKinnon and Parmentier*, 1986; *Spohn and Schubert*, 2003]. On Callisto, measurements of the induced magnetic field suggest that the ice/ocean reflector is located at a depth between 150 and 300 km [*Khurana et al*., 1998; *Zimmer et al*., 2000; *Zhang*, 2003; *Kuskov and Kronrod*, 2005].

Considering the complexity of the targets described above, it is rather difficult to produce a realistic electromagnetic model of the internal structure of the icy satellite crusts. However, it can be conceptually useful to look at the dielectric contrast generated by two adjacent materials, as it can help to understand what could be the detectability limit of each dielectric contrast. Under the assumption of a normally incident plane waves and a perfectly flat interface between two adjacent layers, we used Equation (9) to estimate the reflection coefficients (expressed in dB) between pure water ice and the materials reported in Table 9. Note that for the reflection coefficient of the COF we used the highest value proposed by *Fujita and Mae* [1994]. Moreover, for the brines, not reported in the table, we used a permittivity value of 90 [*Stogryn*, 1971] and for the sulfate eutectic mixtures we computed the bulk permittivity applying the Bruggeman formula, using 3.1 for water ice, 5.3 for $MgSO_4 \cdot 11H_2O$ and 5.0 for $Na_2SO_4 \cdot 10H_2O$ (cf. Figure 15). The permittivity values of CO_2, NH_3 and dirty ice have been taken from *Pettinelli et al*. [2003], *Smyth and Hitchcock* [1934] and *Mattei et al*. [2014], and that of clathrate hydrates from Table 6. The results are illustrated in Figure 21 together with the signal to noise ratio (SNR) estimated by *Blankenship et al*. [2009]. The data show that in the best case, i.e., when the attenuation in the upper layer is negligible as considered here, all contrasts but COF should be detectable as they are well above the SNR threshold.

X FINAL REMARKS

The present review has been inspired primarily by ESA's selection of JUICE, with its radar payload RIME, as the first large mission within its Cosmic Vision Program 2015-2025, as well as by the proposal recently made by NASA regarding a possible parallel mission to Europa. However, the theoretical basis and the experimental evidence summarized and

© 2015 American Geophysical Union. All rights reserved.

Accepted Article

discussed here are also of great interest for the geophysical exploration of the Earth, the Moon, Mars, comet 67P/Churyumov-Gerasimenko and, in general, all solar system bodies where ice can be present at surface or at relatively shallow depths (tens of kilometers). The starting point of this work has been the general similarity between terrestrial and extraterrestrial polycrystalline water ice Ih and, consequently, the expected invariance in its physical behavior. Beyond such similarity, the study of extraterrestrial ice dielectric properties represents a totally "new and unexplored world", first of all because of the limited knowledge on the thermodynamic state of the jovian satellite crusts and, secondly, because of the lack of information on ice origin, evolution and impurity composition. For pure water ice, as for any other crystalline material, the theory on electrical conduction and dielectric polarization is able to account for each phenomenon if, and only if, the crystal is "ideal", i.e., truly pure and defect-free. Every deviation from this ideality introduces new parameters which are difficult to account for. As highlighted in the review, Jaccard theory is sufficient to generalize and quantify both conduction and polarization phenomena in pure water ice using the kinematic concept of protonic point defects migration. That said, the interpretation of experimental data within the framework of the Jaccard theory is not trivial, due to the lack of a standard procedure in ice preparation and measuring techniques, which limits data reproducibility and intercomparison. The introduction of dopants increases the complexity of the phenomenon as incorporation into the ice lattice is not yet fully understood, and it is not totally clear what type of defects are created and in what percentage. The complexity becomes even higher when the coexistence of different chemical species generates cooperative phenomena. Bearing in mind these critical aspects, the development of a predictive dielectric model capable of accounting for the effects of impurity concentration, ice temperature and measuring frequency, is currently quite challenging. Moreover, the analysis of the dielectric properties of other ices (such as CO_2, NH_3, hydrates, etc.) indicates that, at present, very limited information can be extracted, as the experimental data are sparse and usually do not cover the temperature and the frequency intervals of interest for exploration of the icy moons.

These unresolved issues merit specific attention and should be addressed through additional laboratory work. In particular, standardized methodologies that address sample preparation and environmental conditions should be developed to allow for a better inter-comparison of results amongst different laboratories, as ice's dielectric properties strongly depend on the cooling process and growth mechanism. Furthermore, particular effort should be made to solve the apparent diversity in dielectric behavior between laboratory-grown and natural ice.

© 2015 American Geophysical Union. All rights reserved.

Accepted Article

Last but not least, a great effort is required to improve the understanding of the dielectric behavior of non-water ices which, so far, has only been explored for a very limited spectrum of materials.

Despite the limitations described above, in this work we have critically reviewed the available results on the dielectric behavior of the materials that have been detected, or that are expected to be present, in the jovian icy satellite crusts. Among these we have selected the most suitable data to compute the different radio-wave propagation parameters (attenuation, velocity, vertical resolution, and reflection coefficient) with the final goal to obtain an overview of the dielectric behavior of potentially-present materials at the frequency and temperature ranges of interest for the subsurface sounders. Our results allow to compare the different attenuating behavior of the various ices and help to visualize the variety in "dielectric strength" of the targets. These data, together with all other information reported in this review, represent a solid starting point to tackle the topic of solar system ices dielectric properties.

Every planetary mission represents a unique occasion to significantly improve our knowledge in every field of science related to the mission. The next two decades, the time span between JUICE mission selection and completion, will certainly not disappoint the expectations of the scientific community.

XI Appendix 1 Measurements techniques for the estimation of the ice electrical properties

The electromagnetic characterization of natural and artificial solid, liquid and granular samples can be performed using different measurement techniques, which can operate in either the frequency or time domain regimes (see Figure A1). From the viewpoint of the measurement procedure, frequency domain techniques (dielectric spectroscopy) are generally more complex, however they permit direct calculation of the real and imaginary parts of the permittivity from the circuit parameters, assuming a specific equivalent circuit. The main constraint of the frequency domain approach is the frequency band characteristic of each type of instrument (Figure A1), which strongly limits the possibility to perform measurements on the same type of Device Under Test (DUT) in a very broad frequency range (i.e., from DC to microwave). Conversely, time-domain measurement techniques are simpler but data analysis is more complicated and laborious. For example, to obtain the same dielectric parameters as

© 2015 American Geophysical Union. All rights reserved.

Accepted Article

in the frequency domain, the time domain data should be transformed from time to frequency domain and fitted using some dielectric model. However, both approaches are intimately connected and should yield, in principle, the same results [*Kao*, 2004]. Regardless of the type of technique employed, the measurement procedure should fulfill the following requirements: (i) data acquisition should be simple and fast; (ii) sample volume should be large (i.e., the bulk properties of a material should be measured); and (iii) the experimental techniques should be reproducible. An in-depth description of the different techniques used for material electromagnetic characterization is beyond the scope of this review, but can be found in *Chen et al*., [2004] and *Kaatze* [2013]. In the following we will only briefly describe the most common methods used to measure dielectric properties of ice or icy materials.

11.1 Techniques for laboratory-grown ice

The most common frequency domain technique used for ice dielectric characterization is based on the measurement of the impedance of a capacitor (i.e., a capacitive cell) filled with the test material over a wide range of frequencies, from Extremely Low Frequency (ELF) up to Very High Frequency (VHF) [*Von Hippel*, 1954; *Kaatze*, 2013]. In practice, accurate impedance readings can be obtained using capacitive cells equipped with guarded electrodes, which guarantee that the applied electric field is perpendicular to the sample surface [*Scott and Curtis*, 1939; *Misra*, 2004], and adopting four-wires fixtures. The equivalent circuit of the cell consists of a pure capacitor, which accounts for the polarizability of the material, in parallel to a resistor representing the relevant electric losses. An auto-balance bridge (or LCR meter) applies a voltage signal to the cell and measures the in-phase and quadrature current components, from which the capacitance $C(\nu)$ and loss tangent $\tan\delta(\nu)$ are estimated vs. frequency. The real part of permittivity $\varepsilon'(\nu)$ is directly calculated from the ratio of cell capacitance, measured when filled with test material, to capacitance measured when the cell is empty: $\varepsilon'(\nu) = C(\nu) / C_0$. Note that C_0 is a quantity determined by the cell geometry and is, in general, a frequency-independent parameter. Once the real part of permittivity is known, the imaginary part is directly estimated from the measured loss tangent using the equation $\varepsilon'' = \varepsilon' \tan\delta$ from which the effective conductivity can be calculated. Some considerations should be made on the accuracy and sensitivity of the capacitive cell method. At very low temperatures, such as those required to simulate the material that composes the crust of icy satellites, the in-phase and quadrature current components in the cell have very different amplitudes, with the former (i.e., the dissipative term) being much smaller than the latter. As

© 2015 American Geophysical Union. All rights reserved.

Accepted Article

a consequence, the real part of permittivity can be measured with a good accuracy (typical uncertainties are better than about 1%), whereas the lower measurable limit of the loss tangent is of the order of $10^{-3}-10^{-2}$ which, for very cold ice (or in general for low loss materials), can be of the same order as the quantity being measured [see e.g., *Agilent Technologies Impedance Measurement Handbook*, 2000]. It follows that the accuracy on the conductivity is always worse than that of the real part of permittivity.

At Ultra-High Frequencies (UHF – microwaves), the most common method is based on the measurement of wave propagation parameters in a transmission line filled with test material. These parameters can be either estimated in the time domain, using a pulse generator and an oscilloscope through dedicated instruments (TDR), or in the frequency domain, with a VNA. TDR has been extensively used in snow, firn, and ice studies [see e.g., *Stein et al*.,1997; *Stacheder*, 2005], as it is also suitable for in situ measurements. In addition, it allows the estimation of the material apparent permittivity $\varepsilon_a = \frac{1}{2}\left(\varepsilon' + \sqrt{\left(\varepsilon'\right)^2 + \left(\varepsilon''\right)^2}\right)$ using the signal velocity through $\varepsilon_a = \left(c/\mathrm{v}\right)^2$, and the DC conductivity from the signal amplitude under stationary conditions (i.e., when the multiple wave reflections are fully decayed). These parameters can be measured with an accuracy on the order of a few percent (see for details e.g., *O'Connor and Dowling* [1999] and *Ferré and Topp* [2000]). More extensive information can be obtained from measurements in the frequency domain using a two-port transmission line and the so-called scattering parameters (S-parameters), that is, the ratio of reflected or transmitted wave, at each port, to the incident wave (for details see *Chen et al*. [2004]). The extraction of the real and imaginary parts vs. frequency of the material under test requires a suitable algorithm like, for example, the one proposed by Nicolson-Ross-Weir (NRW) [*Chen et al*., 2004 and references therein]. For this method, the accuracy in the real part of permittivity is much better (a few percent) than that in the imaginary part which, in turn, can be estimated within a lower limit of about 10^{-2} [*Mattei et al*., 2013]. Finally, in the microwave range the complex dielectric permittivity can also be measured using resonant cavities, operating only at single frequencies, with an accuracy on the order of 0.01% for the real part of permittivity and an achievable lower limit for the imaginary part on the order of 10^{-8}, which implies a high degree of accuracy on this parameter [*Chen et al*., 2004; *Kaatze*, 2013].

Accepted Article

© 2015 American Geophysical Union. All rights reserved.

11.2 Techniques for ice cores

11.2.1 ECM and AC-ECM methods

Electrical measurements on ice cores have been extensively used for almost four decades, with the main purpose being to infer the ice chemical content as a proxy of the atmospheric composition at the time the snow was deposited [*Wolff*, 2000]. Techniques employed to perform such measurements, such as ECM and DEP, can be considered the non-destructive "evolution" of the method commonly used to measure a specific conductivity profile on melted samples along an ice core [*Hammer*, 1977]. They were originally developed to rapidly detect the abrupt and strong changes of ice core chemical composition associated with specific volcanic or climatic events.

The ECM was first proposed by *Hammer* [1980], who explored the electrical variability of an ice core at high spatial resolution (a few millimetres), applying the well-known DC resistivity method commonly used in geophysical prospecting. He suggested that the intensity of the direct current recorded in a specific core layer is correlated to the level of acidity in the melt-water of that layer. The setup proposed by *Hammer* [1980] consisted of a pair of brass electrodes fed by a voltage of 1250 V and separated by a distance of 1 cm. The electrode pairs were moved at a velocity of 10-20 cm s^{-1} on a freshly exposed ice core surface in a zig-zag fashion (to minimize the influence of air bubbles and other causes of poor contact) to measure the current I between them. The ice core was then sampled and melt-water was analyzed in terms of acidity to build a calibration curve. He found the following correlation: $\left[H^+\right] = 0.045 I^{1.73}$ at -15°C, where the current is expressed in μA and the acidity concentration in μ_{equiv} kg^{-1}. However, the above-mentioned correlation seems to hold just for Greenland ice cores, as no significant correlation has been found for Antarctic ice cores [*Maccagnan and Duval*, 1982*; Legrand*, 1987; *Taylor et al*., 1992]. This different behavior has been explained by Stillman et al. [2013b] using Jaccard theory. Moreover, despite the name, since the exact contact area of the electrodes with the ice and the current geometry are unknown, and since the current response is not linear with voltage [*Taylor et al*., 1992], the method is not suitable to quantitatively estimate the DC conductivity [*Maccagnan and Duval*, 1982]. In fact, the space charge build-up, which takes place close to the ice/electrodes interfaces, over time produces a current reduction that prevents the measurement of the DC value [*Hammer*, 1983; *Neftel et al*., 1985]. *Schwander et al*. [1983] attempted to find an empirical linear relationship between ECM current and conductivity, however their results were inconclusive. Finally, besides the well-known effect of ice temperature on current

© 2015 American Geophysical Union. All rights reserved.

Accepted Article

intensity [*Hammer*, 1980; *Neftel et al*., 1985] it should be underlined that ECM, being mainly affected by surface conductivity, is not totally reproducible, as suggested by significant current variations observed after a time lapse of few weeks to few months [*Taylor et al*., 1992].

As discussed above, ECM is affected by uncertainty that can be mainly attributed to: i) space charge effects arising close to the electrode/ice contact region, and ii) modification of charge location and distribution in the ice caused by the large electric fields typically applied to the ice core. The former effect implies that the measured current is not stable vs. time, whereas the latter is thought to be the primary reason for the degradation of ice surfaces preventing the repeatability of the measurement, unless a mechanical re-smoothing of the surface is performed before a new measurement.

To circumvent these problems, *Sugiyama et al*. [1995] proposed a new method based on Alternate Current (AC) conductance measurements performed at low electric field levels and at frequencies high enough (about 1 MHz) to suppress the space charge effects and reduce, at the same time, the variability due to dielectric relaxations (practically absent above about 100 kHz). The AC-ECM employs the same electrode geometry as the standard ECM, which essentially consists of two cylindrical rods (3 mm diameter, 1 cm apart) grazing the outside skin of the ice. The system slides along the ice core with a continuous motion to obtain measurements with high spatial resolution (few millimetres). However, in contrast to the original ECM, the electrodes are not polarized by a high DC voltage but connected to an LCR-meter (usually a Hewlett-Packard 4284A) operating in the AC regime with an amplitude range of 1-3 V. The measurements are capable of estimating the complex admittance with a high degree of accuracy, using a four-wire configuration, in a wide band of frequencies. The method was validated through the comparison with results obtained from a capacitive cell filled with the same material [*Sugiyama et al*., 1995], allowing a direct cross-check between the real part of the admittance (i.e., the conductance measured with the LCR-meter) and the conductivity of the ice. This method was tested on several Antarctic and Arctic cores [*Sugiyama et al*., 2000], confirming its ability to provide a fast and reliable survey of ice-core conductivity.

11.2.2 DEP method

The DEP technique is based on the measurement of permittivity and conductivity of ice cores vs. frequency through a capacitive cell equipped with curved electrodes, to match ice core shape. The method is equivalent to that already described for laboratory measurements in the

© 2015 American Geophysical Union. All rights reserved.

Accepted Article

ELF – VHF range, but suitably adapted to in-situ core measurements [*Moore and Paren*, 1987]. The ice core is enclosed in a capacitor consisting of a pair of electrodes curved in an arc of 108°. One of the two electrodes (highly elongated in the direction parallel to the core axis) is used to apply the voltage signal to the capacitor (HI electrode), whereas the second, much thinner electrode, virtually grounded by the balance bridge, is used to pick up the current (LO electrode). The voltage to current ratio allows the measurement of the sample complex impedance. The LO electrode is placed between two contiguous additional electrodes, which play the role of guards. Early DEP systems [*Moore and Paren*, 1987] were built using a multi-electrode assembly (made of a large number of 5 cm wide LO electrodes) deployed along the ice core. With such a configuration, the LO electrodes are electrically switched such that when a given LO electrode is selected all the neighboring electrodes are grounded to play the role of guards. In this way a rapid dielectric profile of the core is performed with a resolution limited by the LO electrode width. In addition, DEP systems use blocking electrodes (i.e., electrodes insulated by a thin sheet of Teflon or through anodization) to suppress the charge exchange at the ice/metal interfaces, which is responsible for Maxwell-Wagner relaxation at low frequencies. With this technique *Moore and Maeno* [1991] performed detailed measurements on two cores from different Antarctic regions and having different chemical compositions, showing that DEP can accurately evaluate the conductivity σ_∞ due to the presence of chemical impurities (salts and acids) in the ice. A more advanced DEP device was subsequently proposed by *Wilhelms et al*. [1998] in which the scanning of the ice sample is performed using a sledge mechanism capable of moving the electrodes (HI, LO and Guards) along the core. In this way, and using a much thinner LO electrode (only 1 cm wide), the dielectric profile resolution is significantly improved.

NOTATION

Acronyms

AC	Alternate Current.
ALSE	Apollo Lunar Sounder Experiment.
BDT	Brittle-Ductile Transition.
COF	Crystal Orientation Fabric.
CONSERT	Comet Nucleus Sounding Experiment by Radiowave Transmission.

Accepted Article

© 2015 American Geophysical Union. All rights reserved.

DC	Direct Current.
DEP	Dielectric Profiling.
DUT	Device Under Test.
ECM	Electrical Conductivity Measurements.
ELF	Extremely Low Frequency.
GPR	Ground Penetrating Radar.
HDA	High Density Amorph.
HF	High Frequency.
JAXA	Japan Aerospace Exploration Agency.
JUICE	JUpiter ICy moons Explorer.
LDA	Low Density Amorph.
LRS	Lunar Radar Sounder.
MARSIS	Mars Advanced Radar for Subsurface and Ionosphere Sounding.
MRO	Mars Reconnaissance Orbiter.
NIMS	Near-Infrared Mapping Spectrometer.
NRW	Nicholson-Ross-Weir algorithm.
RES	Radio Echo Sounding.
RIME	Radar for Icy Moon Exploration.
SEP	Surface Electrical Properties.
SHARAD	SHAllow RADar.
SNR	Signal to Noise Ratio
TDR	Time Domain Reflectometry.
UHF	Ultra High Frequency.
VHF	Very High Frequency.
VNA	Vector Network Analyzer.

PARAMETERS

A	attenuation.
B	birefringence.

Accepted Article

© 2015 American Geophysical Union. All rights reserved.

C	capacitance.
c	speed of light in vacuum.
D	dielectric displacement.
E	applied electric field.
E_i^F	activation energy of the i-th defect formation.
E_i^M	activation energy of the i-th defect motion.
$E_{\omega_{rel}}$	activation energy.
E_{σ_∞}	activation energy of high frequency conductivity.
e_i	effective charge of the i-th defect.
H	spacecraft altitude.
J_c	conduction current density.
J_d	displacement current density.
J_T	total current density induced in a material.
j	imaginary unit.
k_B	Boltzmann constant.
M_i	normalization coefficient for mobility of the i-th defect.
M_{hd}	molar weight of a hydrated salt.
N	number of H_2O molecules per unit volume.
N_i	normalization coefficient for volumetric concentration of the i-th defect.
n	hydratation number.
n_i	volumetric concentration of the i-th defect.
P	polarization.
P_a	polarization of an anhydrous salt.
P_W	polarization of water of crystallization.
P_c	irradiated effective power corrected for the geometric spreading and the birefringence factor.
P_e	irradiated effective power.
P_r	reflected power.
R	Fresnel reflection coefficient.

Accepted Article

© 2015 American Geophysical Union. All rights reserved.

r_{O-O} distance between two adjacent oxygens.

T temperature.

$\tan\delta$ loss tangent.

v phase velocity of a plane wave.

$[x]$ molar concentration.

z unidimensional spatial coordinate.

α real part of the propagation constant (attenuation factor).

β imaginary part of the propagation constant (phase constant).

γ propagation constant.

Δz range resolution.

Δv radar signal bandwidth.

ε complex relative permittivity.

ε' real part of the complex relative permittivity.

ε'' imaginary part of the complex relative permittivity.

ε_a apparent permittivity.

ε_s static permittivity.

ε_∞ high frequency permittivity.

ε_0 vacuum permittivity.

$\varepsilon_{\perp c}$ complex permittivity for electric field perpendicular to the *c*-axis.

$\varepsilon_{\square c}$ complex permittivity for electric field parallel to the *c*-axis.

ε_{hd} real part of permittivity for a hydrated salt.

ε_W part of the permittivity of water of crystallization.

$\bar{\varepsilon}(z)$ depth dependent average permittivity.

μ_i mobility of the i-th defect.

v frequency.

v_{rel} relaxation frequency.

ρ density.

ρ_{bulk} bulk density.

ρ_{hd} density of a hydrated salt.

Accepted Article

© 2015 American Geophysical Union. All rights reserved.

σ	effective conductivity.
σ_D	conductivity due to the D defects.
σ_{DL}	Bjerrum conductivity.
$\sigma_{H_3O^+}$	conductivity due to the H_3O^+ ions.
σ_L	conductivity due to the L defects.
σ_{OH^-}	conductivity due to the OH^- ions.
σ_s	static conductivity.
σ_∞	high frequency conductivity.
$\sigma_\pm$	ionic conductivity.
$\hat{\sigma}_i$	molar conductivity of the *i*-th ion.
$\sigma_{\infty\ pure}$	high frequency conductivity of pure ice.
τ_{rel}	relaxation time.
Φ	polarizability constant.
Ψ	total transmission coefficient.
ω	angular frequency.
ω_{rel}	relaxation angular frequency.

GLOSSARY

Annealing: heat treatment capable to modify strength, hardness and ductility properties of materials.

Attenuation: energy reduction factor of electromagnetic waves propagating through a dissipative medium.

Backscattered echo: wave reflection due to discontinuities of the medium electromagnetic properties.

Brittle-Ductile Transition: crust region where rocks modifies the rheology becoming less

Accepted Article

© 2015 American Geophysical Union. All rights reserved.

likely to fracture and more likely to deform.

Bulk (permittivity, conductivity, density): properties averaged in a large volume of material.

Chaos terrain: Europan surface areas with randomly distributed ridges, cracks and plains.

Cole-Cole model: generalization of the Debye relaxation model (see Debye relaxation).

Complex dielectric permittivity: complex parameter, relating the electric field to current density, which considers both the storage and dissipation of energy associated to the polarization process.

Complex magnetic permeability: complex parameter, relating the magnetic field to magnetic induction, which considers both the storage and dissipation of energy associated to the magnetization process.

Conductivity: real coefficient relating electric field to current density in materials.

Constitutive parameters: see complex dielectric permittivity and complex magnetic permittivity.

DC resistivity method: measurement of resistivity of a material through DC current-voltage technique.

Debye relaxation: frequency dispersion due to the delay occurring between polarization response and applied electric field in materials.

Defect in ice lattice: see Intrinsic and Extrinsic defect.

Dispersive behavior: dependence of complex permittivity and permeability (and thus the wave velocity) on frequency.

Accepted Article

© 2015 American Geophysical Union. All rights reserved.

$\delta^{18}O$: ratio of stable isotopes δO^{18} to δO^{16} commonly used as a proxy of the temperature at the time of ice solidification.

Effective charge: fractional electric charge associated to migration of defects in ice according to Bjerrum theory.

Epsomite: hydrated magnesium sulfate ($MgSO_4 \cdot 7H_2O$).

Eutectic system: liquid solution of chemical elements mixed at the specific concentration that solidifies at the lower temperature than any other possible concentration.

Eutectic temperature: solidification temperature of eutectic liquid solutions.

Extrinsic defects: ice lattice defects caused by admixed impurities which increase the bulk electric conductivity.

Fresnel reflection coefficient: fraction of electromagnetic energy reflected by a dielectric interface due to discontinuity in subsurface materials.

Galileo mission: NASA mission devoted to studies of the inner solar system and Jupiter satellites.

Geometric spreading: inverse square law reduction of power density which occurs along a transmitter-receiver radio-path.

High frequency conductivity: real coefficient relating electric field to current density in ice at frequencies higher than Debye relaxation.

Hydrohalite: hydrated sodium chloride formed from brines at low temperatures ($NaCl \cdot 2H_2O$).

Intrinsic defects: defects naturally present in ice lattice, governing the bulk electric conductivity.

© 2015 American Geophysical Union. All rights reserved.

Accepted Article

Low-loss material: material with a low value of the imaginary part of complex permittivity.

Maxwell-Garnett rule: analytical mixing rule capable to evaluate the resultant complex permittivity of a mixture between two substances, as a function of their volume fractions and their individual complex permittivity.

Maxwell-Wagner effect: polarization process due to the charge separation occurring either at inner dielectric interfaces between two different materials (on microscopic scale) or at the external electrode-sample interfaces (on a macroscopic scale).

Meridianite: hydrated magnesium sulfate with chemical formula $MgSO_4 \cdot 11H_2O$.

Mirabilite: hydrated sodium sulfate with chemical formula $Na_2SO_4 \cdot 10H_2O$.

Optical axis: the optic axis of a crystal is the direction in which a ray of transmitted light suffers no birefringence (double refraction).

Partitioning (partition coefficient): fraction of chemical species which is included in the ice lattice with respect to the concentration in liquid phase.

Photolysis: chemical decomposition of molecules caused by electromagnetic radiation.

Polarization: displacement of bound charges in atoms and molecules (atomic or ionic polarization), or re-orientation of existing dipoles under the effect of applied field.

Proton hopping: displacement of protons within the ice lattice which produces electric polarization and conductivity.

Proton ordering: process which controls the energetic status of protons in ice lattice, which, in turn, governs the transition among different ice phases.

Accepted Article

© 2015 American Geophysical Union. All rights reserved.

Radiolysis: chemical dissociation of molecules by high energy radiation.

Relaxation process: phenomenon associated with non-instantaneous polarization response of a material to the applied electric field (see also Debye relaxation).

Relaxation time: time delay between the dielectric polarization of a material and the applied electric field (see also Relaxation process).

Solid-state convection: physical process involving convection in a solid ductile medium.

Space charge: effect arising by separation of mobile charge carriers at dielectric interfaces or close to electrode/material contacting region.

S-parameters: scattering parameters used to characterize a two-port transmission line, defined at each port as the ratio of reflected (or transmitted) waves, to the incident waves.

Stagnant lid: thermal conductive layer formed above a solid-state convective shell with a huge viscosity gradient.

Static conductivity: real coefficient relating electric field to current density in ice at frequencies lower than Debye relaxation.

Tholin: nitrogen-rich organic substances produced by solar radiation and/or energetic particles on nitrogen and methane gaseous mixtures.

ACKNOWLEDGEMENTS

We would like to thank Dr. Joseph A. MacGregor and the other anonymous reviewer whose contribute helped to significantly improve the quality of the manuscript. Moreover, we are grateful to Dr. Stanley Eugene Beaubien for correcting the English. This work has been supported by the Italian Space Agency through Contract ASI/INAF 2013-056-RO. The data presented in this work are available; to have access to the files please contact the

© 2015 American Geophysical Union. All rights reserved.

Accepted Article

corresponding author at the following email address: pettinelli@fis.uniroma3.it.

Accepted Article

REFERENCES

Addison, J. R. (1969), Electrical properties of saline ice, Journal of Applied Physics, 40(8), 3105-3114.

Addison, J. R. (1970), Electrical relaxation in saline ice, Journal of Applied Physics, 41(1), 54-63.

Alavi, S., K. Udachin, and J. A. Ripmeester (2010), Effect of guest–host hydrogen bonding on the structures and properties of clathrate hydrates, Chemistry-A European Journal, 16(3), 1017-1025.

Andersson, O. (2005), Relaxation time of water's high-density amorphous ice phase, Physical review letters, 95(20), 205503.

Andersson, O. (2007), Dielectric relaxation of low-density amorphous ice under pressure, Physical review letters, 98(5), 057602.

Andersson, O. (2008), Dielectric relaxation of the amorphous ices, Journal of Physics: Condensed Matter, 20(24), 244115.

Andersson, O., and Inaba, A. (2006), Dielectric properties of high-density amorphous ice under pressure, Physical Review B, 74(18), 184201.

Annan, A. P., (2002), GPR—History, trends, and future developments, Subsurface sensing technologies and applications, 3(4), 253-270.

Arcone, S. A., A. J. Gow, and S. McGrew (1986), Structure and dielectric properties at 4.8 and 9.5 GHz of saline ice, Journal of Geophysical Research: Oceans (1978–2012), 91(C12), 14281-14303.

Auty, R. P., and R. H. Cole (1952), Dielectric Properties of Ice and Solid DO, The Journal of Chemical Physics, 20, 1309.

© 2015 American Geophysical Union. All rights reserved.

Baker, I., D. Cullen, and D. Iliescu, (2003), The microstructural location of impurities in ice. Canadian journal of physics, 81(1-2), 1-9.

Balanis, C. A. (1989), Advanced Electromagnetic Engineering, 2nd edition, New York: John Wiley & Sons.

Baratta, G. A., G. Leto, F. Spinella, G. Strazzulla, and G. Foti, (1991), The 3.1 microns feature in ion-irradiated water ice, Astronomy and Astrophysics, 252, 421-424.

Barbin, Y., F. Nicollin, W. Kofman, V. Zolotarev, and V. Glotov (1995), Mars 96 GPR program. Journal of applied geophysics, 33(1), 27-37.

Barletta, R. E., J. C. Priscu, H. M. Mader, W. L. Jones and C. H. Roe (2012), Chemical analysis of ice vein microenvironments: II. Analysis of glacial samples from Greenland and Antarctica, Journal of Glaciology, 58(212), 1109.

Barnes, P. R. F., E. W. Wolff, R. Mulvaney, R. Udisti, E. Castellano, R. Röthlisberger, and J. P. Steffensen (2002), Effect of density on electrical conductivity of chemically laden polar ice, Journal of geophysical research, 107(B2), 2029.

Barnes, P. R., and E. W. Wolff (2004), Distribution of soluble impurities in cold glacial ice. Journal of Glaciology, 50(170), 311-324.

Barnes, P. R., E. W. Wolff, D. C. Mallard and H. M. Mader (2003), SEM studies of the morphology and chemistry of polar ice. Microscopy research and technique, 62(1), 62-69.

Barr, A. C., and D. E. Stillman (2011), Strain history of ice shells of the Galilean satellites from radar detection of crystal orientation fabric, Geophysical Research Letters, 38(6).

Bartels-Rausch, T., V. Bergeron, J. H. Cartwright, R. Escribano, J. L. Finney, H. Grothe and N. Uras-Aytemiz (2012), Ice structures, patterns, and processes: a view across the ice fields, Reviews of Modern Physics, 84(2), 885.

Bell, R. E. et al. (2011), Widespread persistent thickening of the East Antarctic Ice Sheet by freezing from the base. Science, 331(6024), 1592-1595.

Bell, R. E., Studinger, M., Tikku, A. A., Clarke, G. K., Gutner, M. M., and Meertens, C. (2002), Origin and fate of Lake Vostok water frozen to the base of the East Antarctic ice

© 2015 American Geophysical Union. All rights reserved.

Accepted Article

sheet. Nature, 416(6878), 307-310.

Berthelier, J. J., R. Ney, F. Costard, M. Hamelin, A. Meyer, B. Martinat, and P. Paillou, (2000), The GPR experiment on NETLANDER. Planetary and Space Science, 48(12), 1161-1180. (I)

Bilgram, J. H., and H. Gränicher (1974), Defect equilibria and conduction mechanisms in ice, Physics of condensed matter, 18(4), 275-291.

Bjerrum, N. (1952), Structure and properties of ice. Science, 115(2989), 385-390.

Blankenship, D. D., and D. L. Morse, (2004, February), Earth's Ice Sheets and Ice Shelves as an Analog for Europa's Icy Shell. In Workshop on Europa's Icy Shell: Past, Present, and Future (Vol. 1, p. 7053).

Blankenship, D.D., D.A. Young, W.B. Moore, J.C. Moore (2009), Radar Sounding of Europa‘s Subsurface Properties and Processes: The View from Earth. Europa, edited by R.T. Pappalardo, W.B. McKinnon & K. Khurana, The Univ. of Arizona Press, Tucson, pp. 631-654.

Bohleber, P., N. Wagner, and O. Eisen, (2012), Permittivity of ice at radio frequencies: Part I. Coaxial transmission line cell, Cold Regions Science and Technology, 82, 56-67.

Borel, C. (1893), Recherche des constants diélectriques de quelque cristaux biaxes,Comptes rendus hebdomadaires des séances de l'Académie des Sciences 116, 1509-1511.

Brown, M. E., and Hand, K. P. (2013). Salts and radiation products on the surface of Europa. The Astronomical Journal, 145(4), 110.

Brox T. I., M. L. Skidmore, and J.R. Brown (2015), Characterizing the internal structure of laboratory ice samples with nuclear magnetic resonance, Journal of Glaciology, 61(225), 55.

Bruzzone, L., G. Alberti, C. Catallo, A. Ferro, W. Kofman, and R. Orosei (2011), Subsurface Radar Sounding of the Jovian Moon Ganymede, in: Proceedings of the IEEE, 99(5), pp. 837-857, doi:10.1109/JPROC.2011.2108990.

Bruzzone, L., J. J. Plaut, G. Alberti, D. D. Blankenship, F. Bovolo, B. A. Campbell, A. Ferro, Y. Gim, W. Kofman, G. Komatsu, W. McKinnon, G. Mitri, R. Orosei, G. W. Patterson, R. Seu (2013), RIME: Radar for Icy Moon Exploration, in: Proceedings of the 33rd IEEE

© 2015 American Geophysical Union. All rights reserved.

Accepted Article

International Geoscience and Remote Sensing Symposium, IGARSS 2013, 3907-3910.

Buffett B. A. (2000), Clathrate hydrates, Annual Review of Earth and Planetary Sciences, 28(1), 477-507.

Burton, E. F., and L. G. Turnbull (1937), Dielectric constants of solids at high frequencies and the influence of water of crystallization on dielectric constant, Proceedings of the Royal Society of London. Series A-Mathematical and Physical Sciences, 158(893), 182-198.

Campbell, B. et al. (2008), SHARAD radar sounding of the Vastitas Borealis Formation in Amazonis Planitia, Journal of Geophysical Research (Planets) 113, 12010.

Camplin, G. C., J. W. Glen, and J. G. Paren, (1978), Theoretical models for interpreting the dielectric behavior of HF-doped ice, Journal of Glaciology, 21, 123-141.

Carlson, R. W., M. S. Anderson, R. Mehlman, and R. E. Johnson (2005), Distribution of hydrate on Europa: Further evidence for sulfuric acid hydrate, Icarus, 177(2), 461-471, doi:10.1016/j.icarus.2005.03.026.

Carlson, R. W., R. E. Johnson, and Anderson, M. S. (1999), Sulfuric acid on Europa and the radiolytic sulfur cycle. Science, 286(5437), 97-99.

Carlson, R. W., W. M. Calvin, J. B. Dalton, G. B. Hansen, R. L. Hudson, R. E. Johnson, T. B. McCord, and M. H. Moore (2009), Europa's Surface Composition, in Europa, edited by R. T. Pappalardo, W. B. McKinnon and K. K. Khurana with the assistance of R. Dotson with 85 collaborating authors, pp. 283-327, University of Arizona Press, Tucson, AZ.

Carlson, R. W., W. Smythe, K. Baines, E. Barbinis, K. Becker, R. Burns, S. S. Calcutt, W. Calvin, R. Clark, G. Danielson, A. Davies, P. Drossart, T. Encrenaz, F. Fanale, J. Granahan, G. Hansen, P. Herrera, C. Hibbitts, J. Hui, P. Irwin, T. Johnson, L. Kamp, H. Kieffer, F. Leader, E. Lellouch, R. Lopes-Gautier, D. Matson, T. McCord, R. Mehlman, A. Ocampo, G. Orton, M. Roos-Serote, M. Segura, J. Shirley, L. Soderblom, A. Stevenson, F. Taylor, J. Torson, A. Weir, and P. Weissman (1996), Near-infrared spectroscopy and spectral mapping of Jupiter and the Galilean satellites: Results from Galileo's initial orbit, Science, 274, 385–388, doi:10.1126/science.274.5286.385.

Carroll, J. (2014), Natural gas hydrates: a guide for engineers, Gulf Professional Publishing.

© 2015 American Geophysical Union. All rights reserved.

Accepted Article

Chen L, C.K. Ong, C.P. Neo, V.V. Varadan, V.K. Varadan (2004), Microwave Electronics: measurement and materials characterization J. Wiley and Sons Ltd.

Cheng, C. K. (1939), The dielectric constants of some metallic sulfates containing various amounts of water of crystallization, Philosophical Magazine, 30(203), 505-515

Chicarro, A., P. Martin, and R. Trautner (2004), The Mars Express mission: an overview, Mars Express: The Scientific Payload, 3-13.

Choukroun, M., S. W. Kieffer, X. Lu, and G. Tobie (2013), Clathrate hydrates: implications for exchange processes in the outer solar system, In The Science of Solar System Ices, pp. 409-454, Springer New York.

Chyba, C. F., S. J. Ostro, and B. C. Edwards, (1998), Radar detectability of a subsurface ocean on Europa, Icarus, 134(2), 292-302.

Cole, K. S., and R. H. Cole, (1941), Dispersion and absorption in dielectrics I, Alternating current characteristics, The Journal of Chemical Physics, 9(4), 341-351.

Cole, R. H., and O. Worz (1969), Physics of Ice, edited by N. Riehl, B. Bullemer, and H. Engelhardt.

Collins, G. C., Head, J. W., Pappalardo, R. T., and Spaun, N. A. (2000). Evaluation of models for the formation of chaotic terrain on Europa. Journal of Geophysical Research: Planets (1991–2012), 105(E1), 1709-1716.

Collins, G., and F. Nimmo, (2009), Chaotic terrain on Europa, Europa, The University of Arizona space science series. University of Arizona Press, Tucson, 259-281.

Cooper, J. F., R. E. Johnson, B. H. Mauk, H. B. Garrett, and N. Gehrels, (2001), Energetic ion and electron irradiation of the icy Galilean satellites, Icarus, 149(1), 133-159.

Craven, M., I. Allison, H. A. Fricker, and R. Warner, (2009), Properties of a marine ice layer under the Amery Ice Shelf, East Antarctica, Journal of Glaciology, 55(192), 717-728.

Craven, M., F. Carsey, A. Behar, J. Matthews, R. Brand, A. Elcheikh, and A. Treverrow (2005), Borehole imagery of meteoric and marine ice layers in the Amery Ice Shelf, East Antarctica. Journal of Glaciology, 51(172), 75-84.

© 2015 American Geophysical Union. All rights reserved.

Accepted Article

Craven, M., I. Allison, R. Brand, A. Elcheikh, J. Hunter, M. Hemer, and S. Donoghue (2004), Initial borehole results from the Amery Ice Shelf hot-water drilling project, Annals of Glaciology, 39(1), 531-539.

Cuffey, M. Kurt and W. Stanley B. Paterson (2010), The physics of glaciers, Academic Press.

Dalton, J. B. (2003), Spectral behavior of hydrated sulfate salts: Implications for Europa mission spectrometer design, Astrobiology, 3, 771–784, doi:10.1089/153110703322736097.

Dalton, J. B. (2007), Linear mixture modeling of Europa's non-ice material based on cryogenic laboratory spectroscopy, Geophys. Res. Lett., 34(21), L21205, doi:10.1029/2007GL031497.

Dalton, J. B., D. P. Cruikshank, K. Stephan, T. B. McCord, A. Coustenis, R. W. Carlson, and A. Coradini (2010), Chemical Composition of Icy Satellite Surfaces, Space Sci. Rev., 153, 113-154, doi:10.1007/s11214-010-9665-8.

Dalton, J. B., O. Prieto-Ballesteros, C. S. Jamieson, J. S. Kargel, J. Jolivet, and R. C. Quinn (2005), Spectral comparison of heavily hydrated salts to disrupted terrains on Europa, Icarus, 177, 472–490, doi:10.1016/j.icarus.2005.02.023.

Dalton, J.B. (2010), Spectroscopy of Icy Moon Surface Materials (2010). Space Sci. Rev., 153, 219-247, doi:10.1007/s11214-010-9658-7.

Dash, J. G., A. W. Rempel and J. S. Wettlaufer (2006), The physics of premelted ice and its geophysical consequences, Reviews of Modern Physics, 78(3), 695.

Davidson D.W. (1973), Water: a comprehensive treatise, Vol2, Water in Crystalline Hydrates Aqueous, Solutions of Simple Non electrolytes, Cap. Clathate hydrates, pp 115-234, The Physycal chemistry of water, Plenum Press NewYork.

Davidson, D. W., and J. A. Ripmeester, (1978), Clathrate ices--recent results, Journal of Glaciology, 21, 33-49.

Davidson, D. W., M. A. Desando, S. R. Gough, Y. P. Handa, C. I. Ratcliffe, J. A. Ripmeester, and J. S. Tse (1987), A clathrate hydrate of carbon monoxide.

Davidson, D. W., S. K. Garg, S. R. Gough, R. E. Hawkins, and J. A. Ripmeester (1977),

© 2015 American Geophysical Union. All rights reserved.

Accepted Article

Characterization of natural gas hydrates by nuclear magnetic resonance and dielectric relaxation, Canadian Journal of Chemistry, 55(20), 3641-3650.

Debye, P. (1929), Polar molecules (No. EPFL-BOOK-106114). Dover.

Di Paolo, F., B. Cosciotti, S. E. Lauro, E. Mattei, E. Pettinelli, G. Vannaroni (2014), Thermal and electromagnetic models for radar sounding of the galilean satellite icy crusts, in: Proceedings of the 15th International Conference on Ground Penetrating Radar, GPR 2014, 362-366.

Dobrin, M. B., and C. H. Savit (1960), Introduction to geophysical prospecting, New York: McGraw-Hill.

Dombard, A. J., and W. B. McKinnon, (2001), Formation of grooved terrain on Ganymede: Extensional instability mediated by cold, superplastic creep, Icarus, 154(2), 321-336.

Dowdeswell, J. A., and S. Evans (2004), Investigations of the form and flow of ice sheets and glaciers using radio-echo sounding, Reports on Progress in Physics, 67(10), 1821.

Dubochet, J., and J. Lepault, (1984), Cryo-electron microscopy of vitrified water, Le Journal de Physique Colloques, 45(C7), C7-85.

Eicken, H., A. L. Lovecraft, and M. L. Druckenmiller, (2009), Sea-Ice System Services: A Framework to Help Identify and Meet Information Needs Relevant for Arctic Observing Networks. Arctic, 62(2).

Eicken, H., M. A. Lange, and P. Wadhams (1994), Characteristics and distribution patterns of snow and meteoric ice in the Weddell Sea and their contribution to the mass balance of sea ice, In Annales Geophysicae (Vol. 12, No. 1, pp. 80-93). Springer-Verlag.

El-Said, M. A. H., (1956), Geophysical prospection of underground water in the desert by means of electromagnetic interference fringes, Proceedings of the IRE, 44(1), 24-30.

ElShafie, A., and E. Heggy, (2013), Radar Detection of the Brittle-Ductile Transition on Icy Satellites Based on Ice's Mechanical and Electrical Properties, 44th Lunar and Planetary Science Conference, The Woodlands, Texas.

Eluszkiewicz J., J. Leliwa-Kopystyński, and K. J. Kossacki (1998), Metamorphism of solar

© 2015 American Geophysical Union. All rights reserved.

Accepted Article

system ices, In Solar System Ices, pp. 119-138, Springer Netherlands.

Famá, M., M. J. Loeffler, U. Raut, and R. A. Baragiola, (2010), Radiation-induced amorphization of crystalline ice, Icarus, 207(1), 314-319.

Ferré, P. A., and G. C. Topp (2000), Time-domain Reflectometry Techniques for Soil Water Content and Electrical Conductivity Measurements, Sensors update, 7(1), 277-300.

Fortes, A. D., and M. Choukroun, (2010), Phase behavior of ices and hydrates, Space science reviews, 153(1-4), 185-218.

Franks, F. (1972), Water: a comprehensive treatise, Vol1, (p 596), Plenum Press Newyork, The Physycal Chemistry of Water.

Fricker, H. A., S. Popov, I. Allison, and N. Young (2001), Distribution of marine ice beneath the Amery Ice Shelf, Geophysical Research Letters, 28(11), 2241-2244.

Fujino, K. (1967), Electrical properties of sea ice, Physics of Snow and Ice: proceedings= 雪氷の物理学: 論文集, 1(1), 633-648.

Fujita, S., and S. Mae, (1994), Causes and nature of ice-sheet radio-echo internal reflections estimated from the dielectric properties of ice, Annals of Glaciology, 20(1), 80-86.

Fujita, S., H. Maeno, S. Uratsuka, T. Furukawa, S. Mae, Y. Fujii, and O. Watanabe (1999), Nature of radio echo layering in the Antarctic Ice Sheet detected by a two-frequency experiment, Journal of Geophysical Research: Solid Earth (1978–2012), 104(B6), 13013-13024.

Fujita, S., T. Matsuoka, T. Ishida, K. Matsuoka, and S. Mae (2000), A summary of the complex dielectric permittivity of ice in the megahertz range and its applications for radar sounding of polar ice sheets, in Physics of Ice Core Records, edited by T. Hondoh, pp. 185-212, Hokkaido University Press, Hokkaido, Japan.

Glen J.W., and J.G. Paren (1975), The electrical Proprieties of snow and Ice, Journal of Glaciology, 15, 15-37.

Goldsby, D. L., and D.L. Kohlstedt, (2002), Reply to comment by P. Duval and M. Montagnat on “Superplastic deformation of ice: Experimental observations”, Journal of

© 2015 American Geophysical Union. All rights reserved.

Accepted Article

Geophysical Research: Solid Earth (1978–2012), 107(B11), ECV-17.

Golombek, M. P., and W. B. Banerdt, (1985), Lithospheric strength of Ganymede: Clues to early thermal profiles from extensional tectonic features, LPI Contributions, 575, 45.

Golombek, M. P., and W. B. Banerdt, (1986), Early thermal profiles and lithospheric strength of Ganymede from extensional tectonic features, Icarus, 68(2), 252-265.

Gough, S. R. (1972), A low temperature dielectric cell and the permittivity of hexagonal ice to 2 K. Canadian Journal of Chemistry, 50(18), 3046-3051.

Gough, S. R., J. A. Ripmeester, and D. W. Davidson (1983), Dielectric evidence for the formation of a clathrate hydrate by sulfuryl chloride, Canadian journal of chemistry, 61(9), 2053-2054.

Gough, S. R., R. E. Hawkins, B. Morris, and D. W. Davidson (1973), Dielectric properties of some clathrate hydrates of structure II, The Journal of Physical Chemistry, 77(25), 2969-2976.

Gough, S. R., and Davidson, D. W. (1970). Dielectric behavior of cubic and hexagonal ices at low temperatures. *The Journal of Chemical Physics*, *52*(10), 5442-5449.

Granicher, H. (1963), Properties and lattice imperfections of ice crystals and behavior of H_2O-HF solid solutions, Phys.condens.Mater., 1, 1-12.

Granicher, H., C. Jaccard, P. Scherrer, and A. Steinemann (1957), Dielectric relaxation and the electrical conductivity of ice crystals, Discussions of the Faraday Society, 23, 50-62.

Grasset, O., M. K. Dougherty, A. Coustenis, E. J. Bunce, C. Erd, D. Titov, M. Blanc, A. Coates, P. Drossart, L. N. Fletcher, H. Hussmann, R. Jaumann, N. Krupp, J. –P. Lebreton, O. Prieto-Ballesteros, P. Tortora, F. Tosi, and T. Van Hoolst (2013), JUpiter ICy moons Explorer (JUICE): An ESA mission to orbit Ganymede and to characterise the Jupiter system, Planet. Space Sci., 78, 1-21, doi:10.1016/j.pss.2012.12.002.

Greeley, R., C. F. Chyba, J. W., III Head, T. B. McCord, W. B. McKinnon, R. T. Pappalardo, and P. H. Figueredo (2004), Geology of Europa, in Jupiter: The planet, satellites, and magnetosphere, edited by F. Bagenal, T. Dowling and W. B. McKinnon, pp. 329-361, Cambridge University Press, Cambridge, U. K.

© 2015 American Geophysical Union. All rights reserved.

Accepted Article

Greenberg, R., P. Geissler, G. Hoppa, B. R. Tufts, D. D. Durda, R. Pappalardo, M. H. Carr, (1998), Tectonic processes on Europa: Tidal stresses, mechanical response, and visible features, Icarus, 135(1), 64-78.

Grima, C., D. M. Schroeder, D. D. Blankenship (2013), Identifying Surface Characteristics Using an Ice Penetrating Radar Sounder at Europa: Potential for Landing Site Selection, 44th Lunar and Planetary Science Conference, The Woodlands, Texas.

Grimm, R. E., D. E. Stillman, S. F. Dec, and M. A. Bullock (2008), Low-frequency electrical properties of polycrystalline saline ice and salt hydrates, The Journal of Physical Chemistry B, 112(48), 15382-15390.

Gross, G. W. (1962), Four-electrode method for measuring the direct-current resistivity of ice, Science, 138(3539), 520-521.

Gross, G. W. (1965), Ion incorporation and activation energies of conduction in ice*, Annals of the New York Academy of Sciences, 125(2), 380-389.

Gross, G. W., A. Gutjahr, and K. Caylor, (1987), Recent experimental work on solute redistribution at the ice/water interface, Implications for electrical properties and interface processes, Le Journal de Physique Colloques, 48(C1), C1-527.

Gross, G. W., and Svec R. K. (1997), Effect of ammonium on anion uptake and dielectric relaxation in laboratory-grown ice columns, The Journal of Physical Chemistry B, 101(32), 6282-6284.

Gross, G. W., I. C. Hayslipand, R. N. Hoy, (1978), Electrical conductivity and relaxation in ice crystals with known impurity content, Journal of Glaciology, 21(85).

Gross, G. W., P. M. Wong, and K. Humes (1977), Concentration dependent solute redistribution at the ice-water phase boundary. III. Spontaneous convection. Chloride solutions, J. Chem. Phys., 67(11), 5264–5274.

Gross, G. W., R. K. Svec, and P. Y. Whung (1994), Dielectric response of ice grown from dilute sulfate solutions, Antarctic Journal of The United States, 29, 75-76.

Gudipati, M. S., and J. Castillo-Rogez (2013), The Science of Solar System Ices, Vol. 356,

© 2015 American Geophysical Union. All rights reserved.

Accepted Article

Springer Science & Business Media.

Gudmandsen, P., (1971), Electromagnetic probing of ice, in Electromagnetic Probing in Geophysics, edited by J. R. Wait, pp. 321-348, Golem Press, Boulder, Colorado.

Hallbrucker, A., E. Mayer, and G. P. Johari (1989), Glass-liquid transition and the enthalpy of devitrification of annealed vapor-deposited amorphous solid water: a comparison with hyperquenched glassy water, The Journal of Physical Chemistry, 93(12), 4986-4990.

Hallikainen, M., and D. P. Winebrenner, (1992), The physical basis for sea ice remote sensing. Geophysical Monograph Series, 68, 29-46.

Hammer, C. U. (1977), Past volcanism revealed by Greenland ice sheet impurities, Nature, 270, 482-486.

Hammer, C. U. (1980), Acidity of polar ice cores in relation to absolute dating, past volcanism, and radio-echoes, Journal of Glaciology, 25, 359-372.

Hammer, C. U. (1983), Initial direct current in the buildup of space charges and the acidity of ice cores, The Journal of Physical Chemistry, 87(21), 4099-4103.

Hand, K. P., C. F. Chyba, R. W. Carlson, and J. F. Cooper (2006), Clathrate hydrates of oxidants in the ice shell of Europa, Astrobiology, 6(3), 463-482.

Hanel, R., B. Conrath, M. Flasar, V. Kunde, P. Lowman, W. Maguire, J. Pearl, J. Pirraglia, R. Samuelson, D. Gautier, P. Gierasch, S. Kumar, and C. Ponnamperuma, (1979), Infrared observations of the Jovian system from Voyager 1, Science, 204, 972-976, doi:10.1126/science.204.4396.972.

Hansen, G. B., and T. B. McCord, (2004), Amorphous and crystalline ice on the Galilean satellites: A balance between thermal and radiolytic processes, Journal of Geophysical Research: Planets (1991–2012), 109(E1).

Hargreaves, N.D., (1978), The polarization of radio signals in the radio-echo sounding of ice sheets, Journal of Physics. D Applied Physics, 10(9), 1285-1304.

Head, J. W., R. T Pappalardo., and Sullivan, R. (1999), Europa: Morphological characteristics of ridges and triple bands from Galileo data (E4 and E6) and assessment of a

© 2015 American Geophysical Union. All rights reserved.

Accepted Article

linear diapirism model. Journal of Geophysical Research: Planets (1991–2012), 104(E10), 24223-24236.

Heggy, E., E.M. Palmer, W. Kofman, S. Clifford, K. Righter and A. Hérique, (2012), Radar properties of comets: Parametric dielectric modeling of Comet 67P/Churyumov–Gerasimenko, Icarus, doi: 10.1016/j.icarus.2012.09.023

Herique, A., J. Gilchrist, W. Kofman, and J. Klinger (2002), Dielectric properties of comet analog refractory materials, Planetary and Space Science, 50(9), 857-863.

Hibbitts, C. A., T. B. McCord, and G. B. Hansen (2000), Distributions of CO2 and SO2 on the surface of Callisto, J. Geophys. Res., 105(E9), 22541-22558, doi:10.1029/1999JE001101.

Hobbs P. V. (1974), Ice physics, Oxford, Clarendon Press, 1.

Holland, P. R., H. F. Corr, D. G. Vaughan, A. Jenkins, and P. Skvarca (2009), Marine ice in Larsen ice shelf, Geophysical Research Letters, 36(11).

Hubbard, B., J. L Tison, F. Pattyn, M. Dierckx, T. Boereboom, D. Samyn (2012), Optical-televiewer-based identification and characterization of material facies associated with an Antarctic ice-shelf rift, Annals of glaciology, 53(60), 137-146.

Hubmann, M. (1978). Effect of pressure on the dielectric properties of ice Ih single crystals doped with NH3 and HF. Journal of Glaciology, 21, 161-172.

Humbel, H., F. Jona, and P. Scherrer (1953), Anisotropie der DielectriziUts Konstante des Ekes., Helv. Phys. Acta., 26, 17-32.

Hurford, T. A., R. A. Beyer, B. Schmidt, B. Preblich, A. R. Sarid, and R. Greenberg (2005), Flexure of Europa's lithosphere due to ridge-loading, Icarus, 177(2), 380-396.

Ingham, M., G. Gouws, S. Buchanan, R. Brown, and T. Haskell, (2012), In-situ measurements of the low frequency dielectric permittivity of first-year Antarctic sea ice, Cold Regions Science and Technology, 83, 139-146.

Itagaki K. (1978), Dielectric properties of dislocation-free ice, Journal of Glaciology, 21, 207-217.

Jaccard, C. (1959), Etude theorique et experimentale des proprietes electriques de la glace

© 2015 American Geophysical Union. All rights reserved.

Accepted Article

(Doctoral dissertation, Diss. Naturwiss. ETH Zürich, Nr. 2871, 0000. Ref.: Scherrer, P.; Korref.: Busch, G.).

Jaccard, C. (1964), Thermodynamics of irreversible processes applied to ice, Physik der kondensierten Materie, 3(2), 99-118.

Jansen, D., A.. Luckman, B. Kulessa, P. R. Holland, and E. C. King, (2013), Marine ice formation in a suture zone on the Larsen C Ice Shelf and its influence on ice shelf dynamics, Journal of Geophysical Research: Earth Surface, 118(3), 1628-1640.

Johari, G. P. (1976), The dielectric properties of H2O and D2O ice Ih at MHz frequencies, The Journal of Chemical Physics, 64, 3998-4005 DOI: http://dx.doi.org/10.1063/1.432033.

Johari, G. P., and S. J. Jones, (1976). Dielectric properties of polycrystalline D2O ice Ih (hexagonal). Proceedings of the Royal Society of London. Series A, Mathematical and Physical Sciences, 467-495.

Johari, G. P. (1981), The spectrum of ice, Contemporary Physics, 22(6), 613-642.

Johari, G. P. and E. Whalley, (1981), The dielectric properties of ice Ih in the range 272–133 K, The Journal of Chemical Physics, 75, 1333.

Johari, G. P., A. Hallbrucker and E. Mayer (1991), The dielectric behavior of vapor-deposited amorphous solid water and of its crystalline forms, The Journal of chemical physics, 95(4), 2955-2964.

Johari, G. P., and Charette, P. A. (1975), The permittivity and attenuation in polycrystalline and single-crystal ice Ih at 35 and 60 MHz. J. Glaciol, 14(71), 293-303.

Johari, G. P., and O. Andersson, (2007a), Vibrational and relaxational properties of crystalline and amorphous ices, Thermochimica Acta, 461(1), 14-43.

Johari, G. P., and O.Andersson (2007b), In situ transformation of amorphous ices at high pressures. Physical Review B, 76(13), 134103.

Johari, G. P., Hallbrucker, A., & Mayer, E. (1991). The dielectric behavior of vapor-deposited amorphous solid water and of its crystalline forms. *The Journal of chemical physics*, *95*(4), 2955-2964.

© 2015 American Geophysical Union. All rights reserved.

Accepted Article

Jonscher, A. K. (1983), Dielectric relaxation in solids, Chelsea Dielectric, London.

Kaatze, U. (2013), Measuring the dielectric properties of materials. Ninety-year development from low-frequency techniques to broadband spectroscopy and high-frequency imaging, Measurement Science and Technology, 24(1), 012005.

Kamiyoshi, K. I., and T. Miyamoto (1950), Dielectric Properties of the Water of Crystallization.

Kao, K. C. (2004), Dielectric phenomena in solids, Academic press.

Kargel, J. S., and J. I. Lunine (1998), Clathrate hydrates on Earth and in the solar system, In Solar System Ices, pp. 97-117, Springer Netherlands.

Kargel, J. S., Brine volcanism and the interior structures of asteroids and icy satellites (1991), Icarus, 94, 368–390, doi:10.1016/0019-1035(91)90235-L.

Kargel, J. S., et al. (2000), Europa's crust and ocean: Origin, composition, and the prospects for life. Icarus, 148(1), 226-265.

Kawada, S. (1978), Dielectric anisotropy in ice Ih, Journal of the Physical Society of Japan, 44(6), 1881-1886.

Khazendar, A., J. L Tison, B. Stenni, M. Dini, and A. Bondesan (2001), Significant marine-ice accumulation in the ablation zone beneath an Antarctic ice shelf, Journal of Glaciology, 47(158), 359-368.

Khurana, K. K., M. G. Kivelson, D. J. Stevenson, G. Schubert, C. T. Russell, R. J. Walker, and C. Polanskey (1998), Induced magnetic fields as evidence for subsurface oceans in Europa and Callisto, Nature, 395, 777–780, doi:10.1038/27394.

Kivelson, M. G., K. K. Khurana, and M. Volwerk (2002), The Permanent and Inductive Magnetic Moments of Ganymede, Icarus, 157, 507–522, doi:10.1006/icar.2002.6834.

Kivelson, M. G., K. K. Khurana, C. T. Russell, M. Volwerk, R. J. Walker, and C. Zimmer (2000), Galileo magnetometer measurements: A stronger case for a subsurface ocean at Europa, Science, 289, 1340-1343, doi:10.1126/science.289.5483.1340.

Kofman W. et al. (2007), The Comet Nucleus Sounding Experiment by Radiowave

© 2015 American Geophysical Union. All rights reserved.

Accepted Article

Transmission (CONSERT): A Short Description of the Instrument and of the Commissioning Stages Space Science Reviews 01/2007; 128(1):413-432. DOI:10.1007/s11214-006-9034-9

Kofman, W., R. Orosei, and E. Pettinelli (2010), Radar Signal Propagation and Detection Through Ice, Space Sci. Rev., 153(1-4), 249-271, doi:10.1007/s11214-010-9642-2.

Koh, G. (1992), Dielectric constant of ice at 26.5–40 GHz, Journal of applied physics, 71(10), 5119-5122.

Kouchi, A., and Kuroda, T. (1990), Amorphization of cubic ice by ultraviolet irradiation, Nature 344, 134 – 135, doi:10.1038/344134a0

Kovacs, A., A. J. Gow, and R. M. Morey (1995), The in-situ dielectric constant of polar firn revisited, Cold Regions Science and Technology, 23(3), 245-256.

Kulessa, B. (2007), A critical review of the low-frequency electrical properties of ice sheets and glaciers, Journal of Environmental & Engineering Geophysics, 12(1), 23-36.

Kuskov, O.L., and V. A. Kronrod (2005), Internal structure of Europa and Callisto, Icarus, 177, 550–569, doi:10.1016/j.icarus.2005.04.014.

Lauro, S.E et al. (2010), Permittivity estimation of layers beneath the northern polar layered deposits, Mars, Geophysical Research Letter 37.

Lauro, S.E., E.Mattei, F. Soldovieri, E. Pettinelli, R.Orosei, G. Vannaroni (2012), Dielectric constant estimation of the uppermost Basal Unit layer in the martian Boreales Scopuli region. Icarus 219, 458-467.

Legrand, M. (1987), Chemistry of Antarctic snow and ice, Le Journal de Physique Colloques, 48(C1), C1-77.

Legrand, M. and P. Mayewski (1997), Glaciochemistry of polar ice cores: A review, Reviews of Geophysics, 35(3), 219-243.

Levi, L. (1967), Electrical properties of ice doped with different electrolytes, Physics of Snow and Ice: proceedings= 雪氷の物理学: 論文集, 1(1), 159-172.

Levi, L., and L. Lubart (1961), Conductivite Electrique De La Glace Dopee De NH4OH,

© 2015 American Geophysical Union. All rights reserved.

Accepted Article

Journal De Chimie Physique et de Physico-Chimie Biologique, 58(9), 863-868.

Lewis, E. L., and R. G. Perkin (1986), Ice pumps and their rates, Journal of Geophysical Research: Oceans (1978–2012), 91(C10), 11756-11762.

Li, J., J. C. Andrews-Hanna, Y. Sun, R. J. Phillips, J. J. Plaut, and M. T. Zuber, (2012), Density variations within the south polar layered deposits of Mars, Journal of Geophysical Research: Planets (1991–2012), 117(E4).

Lorenz R. D. (1998), Preliminary measurements of the cryogenic dielectric properties of water–ammonia ices: Implications for radar observations of icy satellites, Icarus, 136(2), 344-348.

Lorenz, R. D. (1999), Calorimetric radar absorptivity measurement using a microwave oven, Measurement Science and Technology, 10(6), L29.

Lorenz, R. D., and S. E. Shandera (2001), Physical properties of ammonia-rich ice: Application to Titan, Geophysical research letters, 28(2), 215-218.

Maccagnan, M., and P. Duval (1982), Electrical behavior of Antarctic ice and radio echo layers in ice sheets, Ann. Glaciol, 3, 195-198.

MacGregor, J. A., D. P. Winebrenner, H. Conway, K. Matsuoka, P. A. Mayewski, and G. D. Clow, (2007), Modeling englacial radar attenuation at Siple Dome, West Antarctica, using ice chemistry and temperature data, Journal of Geophysical Research: Earth Surface (2003–2012), 112(F3).

Maeno, N. (1973). Single Crystals of Ice Grown from KCl Solution and Their Dielectric Properties. Canadian Journal of Physics, 51(10), 1045-1052.

Maidique, M. A., A. von Hippel, and W. B. Westphal (1971), Transfer of protons through “pure” ice Ih single crystals. III. Extrinsic versus intrinsic polarization; Surface versus volume conduction, The Journal of Chemical Physics, 54(1), 150-160.

Matsuoka, K., J. A. MacGregor, and F. Pattyn (2010), Using englacial radar attenuation to better diagnose the subglacial environment: A review, In Ground Penetrating Radar (GPR), 2010 13th International Conference on (pp. 1-5). IEEE.

Accepted Article

© 2015 American Geophysical Union. All rights reserved.

Matsuoka, K., S. Fujita, T. Matsuoka, T. Ishida, T. Hondoh And S. Mae (1996b), Measurements of the complex permittivity of acid-doped ice from 1 kHz to 30 MHz: new data set for developing ice radar and dielectric analysis of ice cores, In Proceedings of the NIPR Symposium on Polar Meteorology and Glaciology (Vol. 10, pp. 25-35).

Matsuoka, K., T. Furukawa, S. Fujita, H. Maeno, S. Uratsuka, R. Naruse, and O.Watanabe (2003), Crystal orientation fabrics within the Antarctic ice sheet revealed by a multipolarization plane and dual-frequency radar survey, Journal of Geophysical Research: Solid Earth (1978–2012), 108(B10).

Matsuoka, T., Fujita, S., and Mae, S. (1996a), Effect of temperature on dielectric properties of ice in the range 5–39 GHz. Journal of Applied Physics, 80(10), 5884-5890.

Matsuoka, T., S. Fujita and S. Mae, (1997), Dielectric properties of ice containing ionic impurities at microwave frequencies, The Journal of Physical Chemistry B, 101(32), 6219-6222.

Mattei, E., S. E. Lauro, E. Pettinelli, and G. Vannaroni (2013), Coaxial-Cage Transmission Line for Electromagnetic Parameters Estimation, IEEE Transactions on Instrumentation and Measurement vol. 62, no. 11.

Mattei, E., S. E. Lauro, G. Vannaroni, B. Cosciotti, F. Bella, and E. Pettinelli, (2014), Dielectric measurements and radar attenuation estimation of ice/basalt sand mixtures as martian Polar Caps analogues, Icarus, 229, 428-433.

Matzler, C., and U. Wegmuller, (1987), Dielectric properties of freshwater ice at microwave frequencies, Journal of Physics D: Applied Physics, 20(12), 1623.

Maxwell, T. A., and R. J. Phillips, (1978), Stratigraphic correlation of the radar-detected subsurface interface in Mare Crisium, Geophysical Research Letters, 5(9), 811-814.

Mayer, E., and P. Brüggeller (1982), Vitrification of pure liquid water by high pressure jet freezing.

McCarthy, C., Cooper, R. F., Kirby, S. H., Rieck, K. D., & Stern, L. A. (2007). Solidification and microstructures of binary ice-I/hydrate eutectic aggregates. American Mineralogist, 92(10), 1550-1560.

© 2015 American Geophysical Union. All rights reserved.

Accepted Article

McCarthy, C., R. F. Cooper, D. L. Goldsby, W. B. Durham, and S. H. Kirby (2011), Transient and steady state creep response of ice I and magnesium sulfate hydrate eutectic aggregates, Journal of Geophysical Research: Planets (1991–2012), 116(E4).

McCord, T. A., G. B. Hansen, R. N. Clark, P. D. Martin, C. A. Hibbitts, F. P. Fanale, and G. E. Danielson (1998), Non-water-ice constituents in the surface material of the icy Galilean satellites from the Galileo near-infrared mapping spectrometer investigation, Journal of Geophysical Research: Planets (1991–2012), 103(E4), 8603-8626.

McCord, T. B., G. B. Hansen, and C. A. Hibbitts, Hydrated Salt Minerals on Ganymede's Surface: Evidence of an Ocean Below (2001), Science, 292, 1523-1525, doi:10.1126/science.1059916.

McCord, T. B., G. B. Hansen, D. L. Matson, T. V. Johnson, J. K. Crowley, F. P. Fanale, R. W. Carlson, W. D. Smythe, P. D. Martin, C. A. Hibbitts, J. C. Granahan, A. Ocampo, and the NIMS Team (1999), Hydrated salt minerals on Europa's surface from the Galileo NIMS investigation, J. Geophys. Res., 104, 11827–11851, doi:10.1029/1999JE900005.

McKinnon, W. B. (1999), Convective instability in Europa's floating ice shell, Geophysical research letters, 26(7), 951-954.

McKinnon, W. B. (2005), Radar sounding of convecting ice shells in the presence of convection: application to Europa, Ganymede, and Callisto, In Workshop on Radar Investigations of Planetary and Terrestrial Environments (Vol. 1, p. 53).

McKinnon, W. B. (2006), On convection in ice I shells of outer Solar System bodies, with detailed application to Callisto, Icarus, 183(2), 435-450.

McKinnon, W. B., and E. M. Parmentier (1986), Ganymede and Callisto, in IAU Colloq. 77: Some Background about Satellites, Vol. 1, pp. 718-763.

Miller, S. L. (1961), The occurrence of gas hydrates in the solar system, Proceedings of the National Academy of Sciences of the United States of America, 47(11), 1798.

Miller, S. L. (1969), Clathrate hydrates of air in Antarctic ice, Science, 165(3892), 489-490.

Mishima, O., L. D. Calvert, and E. Whalley, (1985), An apparently first-order transition between two amorphous phases of ice induced by pressure, Nature, 314(6006), 76-78.

© 2015 American Geophysical Union. All rights reserved.

Accepted Article

Misra, D. K. (2004), Permittivity Measurement, Electrical Measurement, Signal Processing, and Displays, Webster, J. G. (Ed.), CRC Press.

Moore, J. C., and Paren, J. G. (1987). A new technique for dielectric logging of Antarctic ice cores. *Le Journal de Physique Colloques*, *48*(C1), C1-155.

Moore, J. C., R. Mulvaney, and J. G. Paren (1989), Dielectric stratigraphy of ice: A new technique for determining total ionic concentrations in polar ice cores, Geophysical Research Letters, 16(10), 1177-1180.

Moore, J. C., (2000), Models of radar absorption in Europa ice, Icarus, 147(1), 292-300.

Moore, J. C., and N. Maeno, (1991), Application of the dielectric profiling technique to ice core studies, In Proc. NIPR Symp. Polar Meteorol. Glaciol (Vol. 4, pp. 81-92).

Moore, J. C., E. W. Wolff, H. B. Clausen, C. U. Hammer, M. R. Legrand, and K. Fuhrer, (1994a), Electrical response of the Summit-Greenland ice core to ammonium, sulfuric acid, and hydrochloric acid, Geophysical Research Letters, 21(7), 565-568.

Moore, J. C., Reid, A. P., & Kipfstuhl, J. (1994b). Microstructure and electrical properties of marine ice and its relationship to meteoric ice and sea ice. *Journal of Geophysical Research: Oceans* (1978–2012), 99(C3), 5171-5180.

Moore, J. M., C. R. Chapman, E. B. Bierhaus, R. Greeley, F. C. Chuang, J. Klemaszewski, R. N. Clark, J. B. Dalton, C. A. Hibbitts, P. M. Schenk, J. R. Spencer, and R. Wagner (2004), Callisto, in Jupiter: The Planet, Satellites and Magnetosphere, edited by F. Bagenal, T. Dowling and W. McKinnon, pp. 397–426, Cambridge University Press, Cambridge, U. K.

Moore, J. M., E. Asphaug, D. Morrison, J. R. Spencer, C. R. Chapman, B. Bierhaus, R. J. Sullivan, F. C. Chuang, J. E. Klemaszewski, R. Greeley, K. C. Bender, P. E. Geissler, P. Helfenstein, C. B. Pilcher (1999), Mass Movement and Landform Degradation on the Icy Galilean Satellites: Results of the Galileo Nominal Mission, Icarus, 140, 294-312.

Moore, J., J. Paren, and H. Oerter (1992), Sea salt dependent electrical conduction in polar ice, Journal of Geophysical Research: Solid Earth (1978–2012), 97(B13), 19803-19812.

Moore, M. H.; R. L. Hudson, R. W. Carlson (2007), The radiolysis of SO2 and H2S in water ice: Implications for the icy jovian satellites, Icarus, Volume 189, Issue 2, p. 409-423, doi:

© 2015 American Geophysical Union. All rights reserved.

Accepted Article

10.1016/j.icarus.2007.01.018.

Morey, R. M., A. Kovacs, and G. F. Cox (1984), Electromagnetic properties of sea ice, Cold Regions Science and Technology, 9(1), 53-75.

Morgan, V. I. (1972), Oxygen isotope evidence for bottom freezing on the Amery Ice Shelf., Nature, 238(5364), 393-394.

Murthy, S. S. N. (1999), Detailed study of ice clathrate relaxation: Evidence for the existence of clathrate structures in some water-alcohol mixtures, The Journal of Physical Chemistry A, 103(40), 7927-7937.

Nagle, J. F. (1979), Theory of the dielectric constant of ice, Chemical Physics, 43(3), 317-328.

Neal, C. S. (1979), The dynamics of the Ross Ice Shelf revealed by radio echo-sounding, Journal of Glaciology, 24, 295-307.

Neftel, A., M. Andree, J. Schwander, B. Stauffer, and C. U. Hammer (1985), Measurements of a kind of DC-conductivity on cores from Dye 3, Geophysical Monograph Series, 33, 32-38.

Nimmo, F., and P. Schenk, (2006), Normal faulting on Europa: Implications for ice shell properties. Journal of structural geology, 28(12), 2194-2203.

Nimmo, F., and R. T. Pappalardo, (2004), Furrow flexure and ancient heat flux on Ganymede, Geophysical research letters, 31(19).

Nimmo, F., B. Giese, and R. T. Pappalardo (2003), Estimates of Europa's ice shell thickness from elastically-supported topography, Geophysical research letters, 30(5).

Nimmo, F., Pappalardo, R. T., and Giese, B. (2002). Effective elastic thickness and heat flux estimates on Ganymede. *Geophysical research letters*, *29*(7), 62-1.

Obbard, R., D. Iliescu, D. Cullen, J. Chang, and I. Baker, (2003), SEM/EDS comparison of polar and seasonal temperate ice, Microscopy research and technique, 62(1), 49-61.

O'Connor, K. M., and C. H. Dowding (1999), Geomeasurements by pulsing TDR cables and probes. CRC Press.

© 2015 American Geophysical Union. All rights reserved.

Accepted Article

Oerter, H., J. Kipfstuhl, J. Determann, H. Miller, D. Wagenbach, A. Minikin, and W. Graf (1992), Evidence for basal marine ice in the Filchner-Ronne ice shelf., Nature, 358, 399-401.

Okada, T., and T. Ono, (1998), Application of altimeter experiments of Planet-B orbiter to the exploration of Martian surface and subsurface layers, Earth Planets Space, 50(3), 235-240.

Olhoeft, G. R. (1998), Ground penetrating radar on Mars, In Proc. of Seventh Intl. Conf. on Ground Penetrating Radar (Vol. 387).

Ono, T., A. Kumamoto, Y. Kasahara, Y. Yamaguchi, A. Yamaji, T. Kobayashi, and H. Oya, (2010), The Lunar Radar Sounder (LRS) Onboard theá KAGUYA (SELENE) Spacecraft, Space science reviews, 154(1-4), 145-192.

Onsager, L., and M. Dupuis (1960), The electrical properties of ice, Termodinamica dei processi irreversibili, Rendiconti della Scuola Internazionale di Fisica "Enrico Fermi," Corso X, Varenna, 1959., 294-315.

Ori, G. G., and F. Ogliani, (1996), Potentiality of the ground-penetrating radar for the analysis of the stratigraphy and sedimentology of Mars, Planetary and space science, 44(11), 1303-1315. (I)

Orlando, T. M., T. B. McCord, and G. A. Grieves, (2005), The chemical nature of Europa surface material and the relation to a subsurface ocean, Icarus, 177(2), 528-533.

Orton, G. S., J. R. Spencer, L. D. Travis, T. Z. Martin, and L. K. Tamppari (1996), Galileo Photopolarimeter-Radiometer Observations of Jupiter and the Galilean Satellites, Science, 274(5286), 389-391, doi:10.1126/science.274.5286.389.

Paillou P., J. Lunine, G. Ruffiè, P. Encraz, S. Wall, R. Lorentz, and M. Janssen (2008), Microwave dielectric constant of Titan-relevant materials, Geophysical Research Letters, 35(18).

Pappalardo, R. T., and A. C. Barr, (2004), The origin of domes on Europa: The role of thermally induced compositional diapirism, Geophysical research letters, 31(1).

Pappalardo, R. T., G. C. Collins, J. W. Head, P. Helfenstein, T. B. McCord, J. M. Moore, L. M. Prockter, P. M. Schenk, and J. R. Spencer (2004), Geology of Ganymede, in Jupiter: The

© 2015 American Geophysical Union. All rights reserved.

Accepted Article

planet, satellites, and magnetosphere, edited by F. Bagenal, T. Dowling and W. B. McKinnon, pp. 363-396, Cambridge University Press, Cambridge, U.K..

Pappalardo, R. T., J. W. Head, R. Greeley, R. J. Sullivan, C. Pilcher, G. Schubert, D. L Goldsby, (1998), Geological evidence for solid-state convection in Europa's ice shell, Nature, 391(6665), 365-368.

Petit, J. R., J. Jouzel, D. Raynaud, N. I. Barkov, J. M. Barnola, I. Basile, and M. Stievenard, (1999), Climate and atmospheric history of the past 420,000 years from the Vostok ice core, Antarctica, Nature, 399(6735), 429-436.

Petrenko, V. F. (1993), Electrical properties of ice (No. CRREL-SR-93-20), Cold Regions Research And Engineering Lab Hanover Nh.

Petrenko, V.F., and R. W. Whitworth (1999), Physics of Ice, 386 pp., Oxford University Press, USA, doi:10.1093/acprof:oso/9780198518945.001.0001.

Pettinelli, E., G. Vannaroni, A. Cereti, F. Paolucci, G. Della Monica, M. Storini, and F. Bella (2003), Frequency and time domain permittivity measurements on solid CO2 and solid CO2–soil mixtures as Martian soil simulants, Journal of Geophysical Research: Planets (1991–2012), 108(E4).

Phillips, C. B., R. T. Pappalardo (2014), Europa Clipper Mission Concept, Eos, Transactions American Geophysical Union 95 (20), 165-167.

Phillips, R. J et al. (2008), Mars north polar deposits: Stratigraphy, age, and geodynamical response. Science, 320(5880), 1182-1185.

Picardi, G., S. Sorge, R. Seu, J. J. Plaut, W. Johnson, R. L. Jordan, and E. Zampolini, (1999), The Mars advanced radar for subsurface and ionosphere sounding (MARSIS): concept and performance. In Geoscience and Remote Sensing Symposium, 1999. IGARSS'99 Proceedings. IEEE 1999 International (Vol. 5, pp. 2674-2677). IEEE.

Picardi, G. (2004), Radar for measuring interplanetary bodies. In: Ground Penetrating Radar (2nd Edition), Daniels, David J. (Editor), Institution of Engineering and Technology, 663-686.

Picardi, G. et al. (2005), Radar soundings of the subsurface of Mars. Science 310(5756),

© 2015 American Geophysical Union. All rights reserved.

Accepted Article

1925-1928.

Plaut, J. J et al. (2007), Subsurface radar sounding of the south polar layered deposits of Mars, Science, 316(5821), 92-95.

Poole P. H., U. Essmann, F. Sciortino, and H. E. Stanley (1993), Phase diagram for amorphous solid water, Physical Review E, 48(6), 4605.

Popov, I., A. Puzenko, A. Khamzin, and Y. Feldman (2015), The dynamic crossover in dielectric relaxation behavior of ice I h, Physical Chemistry Chemical Physics, 17(2), 1489-1497.

Porcello, L. J., R. L. Jordan, J. S. Zelenka, G. F. Adams, R. J. Phillips, W. E. Brown Jr, and P. L. Jackson, (1974), The Apollo lunar sounder radar system, Proceedings of the IEEE, 62(6), 769-783.

Prieto-Ballesteros, O., J. S. Kargel, M. Fernández-Sampedro, F. Selsis, E. S. Martínez, and D. L. Hogenboom (2005), Evaluation of the possible presence of clathrate hydrates in Europa's icy shell or seafloor, Icarus, 177(2), 491-505.

Prockter, L. M., J. W.Head, R. T. Pappalardo, D. A. Senske, G. Neukum, R. Wagner, and M. J. Belton, (1998), Dark terrain on Ganymede: Geological mapping and interpretation of Galileo Regio at high resolution, Icarus, 135(1), 317-344.

Reynolds, J. M. (1985), Dielectric behavior of firn and ice from the Antarctic Peninsula, Antarctica, J. Glaciol, 31(109), 253-262.

Rick, S. W., and D. L. Freeman (2010), Proton disorder and the dielectric constant of type II clathrate hydrates, The Journal of chemical physics, 132(5), 054509.

Robin, G. D. Q., S. Evans, and J. T. Bailey (1969), Interpretation of radio echo sounding in polar ice sheets, Philosophical Transactions of the Royal Society of London. Series A, Mathematical and Physical Sciences, 265 (1166), 437-505.

Robin, G. de Q., C.S.M. Doake, H. Kohnen, R.D. Crabtree, S.R. Jordan, and D. Moller (1983), Regime of the FiIchner-Ronne ice shelves, Antarctica. Nature, 302(5909), 582-586.

Roth, L., J. Saur, K. D. Retherford, D. F. Strobel, P. D. Feldman, M. A. McGrath, and F.

© 2015 American Geophysical Union. All rights reserved.

Accepted Article

Nimmo (2014), Transient water vapor at Europa's south pole, Science, 343 (6167), 171-174.

Roush, T. L. (2001), Physical state of ices in the outer solar system. Journal of Geophysical Research, Volume 106, Issue E12, p. 33315-33324, doi: 10.1029/2000JE001334

Schmidt, B. E., D. D. Blankenship, G. W. Patterson, and P. M. Schenk (2011), Active formation of "chaos terrain" over shallow subsurface water on Europa, Nature, 479(7374), 502-505, doi:10.1038/nature10608.

Schwander, J., A. Neftel, H. Oeschger, and B. Stauffer (1983), Measurement of direct current conductivity on ice samples for climatological applications, The Journal of Physical Chemistry, 87(21), 4157-4160.

Scott, A. H., and H. L. Curtis (1939), Edge correction in the determination of dielectric constant., Journal of Research, 747-775.

Seu, R. et al. (2007), Accumulation and Erosion of Mars' South Polar Layered Deposits, Science, 317(5845), 1715-1718, doi:10.1126/science.1144120.

Seufert, M., J. Saur, and F. M. Neubauer (2011), Multi-frequency electromagnetic sounding of the Galilean moons, Icarus, 214, 477–494, doi:10.1016/j.icarus.2011.03.017.

Showman, A., and R. Malhotra (1999), The Galilean Satellites, Science, 286, 77-84, doi:10.1126/science.286.5437.77.

Siegert, M. J., and R. Kwok, (2000), Ice-sheet radar layering and the development of preferred crystal orientation fabrics between Lake Vostok and Ridge B, central East Antarctica, Earth and Planetary Science Letters, 179(2), 227-235.

Siegert, M. J., S. Carter, I. Tabacco, S. Popov, and D. D. Blankenship, (2005), A revised inventory of Antarctic subglacial lakes, Antarctic Science, 17(03), 453-460.

Sihvola, A. H. (Ed.), (1999), Electromagnetic mixing formulas and applications, IEE, Electromagnetic Waves Series, No. 47.

Sillars, R. W. (1937),The properties of a dielectric containing semiconducting particles of various shapes, Institution of Electrical Engineers-Proceedings of the Wireless section of the Institution, 12(35), 139-155.

© 2015 American Geophysical Union. All rights reserved.

Accepted Article

Simmons, G., T. Todd, and H. Wang, (1973), The 25-km discontinuity: Implications for lunar history, Science, 182(4108), 158-161.

Simpson, R. A., B. C. Fair, and H. T. Howard (1980), Microwave properties of solid CO2. Journal of Geophysical Research: Solid Earth (1978–2012), 85(B10), 5481-5484.

Singh, V. P., P. Singh, and Haritashya, U. K. (2011), Encyclopedia of Snow, Ice and Glaciers, Encyclopedia of Earth Sciences Series.

Sloan E. D.J., Koh A. C. (2008), Clathrate Hydrates of Natural Gases, Chemical Industries Series, CRC Press, p. 721.

Sloan, E. D. J. (1998), Physical/chemical properties of gas hydrates and application to world margin stability and climatic change, Geological Society, London, Special Publications, 137(1), 31-50.

Smyth, C. P., and C. S. Hitchcock, (1934), The Dielectric Constants and Transitions of Solid Ammonia, Hydrogen Sulfide and Methyl Alcohol, Journal of the American Chemical Society, 56(5), 1084-1087.

Sohl, F., M. Choukroun, J. Kargel, J. Kimura, R. T. Pappalardo, S. Vance, and M. Zolotov (2010), Subsurface Water Oceans on Icy Satellites: Chemical Composition and Exchange Processes, Space Sci. Rev., 153(1-4), 485-510, doi:10.1007/s11214-010-9646-y.

Sotin, C., and G. Tobie (2004), Internal structure and dynamics of the large icy satellites, C. R. Physique, 5, 769-780, doi:10.1016/j.crhy.2004.08.001.

Spencer, J. R., L. K. Tamppari, T. Z. Martin, and L. D. Travis (1999), Temperatures on Europa from Galileo Photopolarimeter-Radiometer: Nighttime Thermal Anomalies, Science, 284(5419), 1514-1516, doi:10.1126/science.284.5419.1514.

Spohn, T., and G. Schubert (2003), Oceans in the icy Galilean satellites of Jupiter?, Icarus, 161, 456–467, doi:10.1016/S0019-1035(02)00048-9.

Stacheder, M. (2005), TDR and low-frequency measurements for continuous monitoring of moisture and density in a snow pack, Int. Agrophysics, 19, 75-78.

Stein, J., G. Laberge and D. Lévesque (1997), Monitoring the dry density and the liquid water

© 2015 American Geophysical Union. All rights reserved.

Accepted Article

content of snow using time domain reflectometry (TDR), Cold Regions Science and Technology, 25(2), 123-136.

Steinemann, A. and H. Granicher (1957), Dielektrische Eigenschaften von Eiskristallen II. Teil Dielectrische Untersuchungen an Eiskristallen mit eingelagerten Fremdatomen, Helv. Phys. Acta, 30, 581-610.

Stillman, D. E., and R. E. Grimm, (2011), Dielectric signatures of adsorbed and salty liquid water at the Phoenix landing site, Mars, Journal of Geophysical Research: Planets, 116 (E9).

Stillman, D. E., J. A. MacGregor and R. E. Grimm, (2013b), The role of acids in electrical conduction through ice, Journal of Geophysical Research: Earth Surface, 118 (1), 1-16.

Stillman, D. E., J. A. MacGregor, and R. E. Grimm, (2013a), Electrical response of ammonium-rich water ice, Annals of Glaciology, 54 (64), 21-26.

Stillman, D. E., R. E. Grimm and S. F. Dec (2010), Low-Frequency Electrical Properties of Ice Silicate Mixtures, The Journal of Physical Chemistry B, 114 (18), 6065-6073.

Stogryn, A. (1971). Equations for calculating the dielectric constant of saline water (correspondence). *IEEE transactions on microwave theory and Techniques*, 733-736.

Strangway, P. K., H. D. Lien, and H. U. Ross, (1969), Studies on kinetics of iron oxide reduction. Canadian Metallurgical Quarterly, 8(2), 235-244.

Suga, H., Matsuo, T., and Yamamuro, O. (1993). Molecular motion and phase transitions of clathrate hydrates. Supramolecular Chemistry, 1(3-4), 221-233.

Sugiyama, K., S. Fujita, H. Narita, S. Mae, T. Hondoh, K. Goto-Azuma, and R. M. Koerner, (2000), Measurement of electrical conductance in ice cores by AC-ECM method, Physics of Ice Core Records, 173-184.

Sugiyama, K., S. Fujita, S. Sueoka, S. Mae, and T. Hondoh, (1995), Preliminary measurement of high-frequency electrical conductivity of Antarctic ice with AC-ECM technique, In Proceedings of the NIPR Symposium on Polar Meteorology and Glaciology (Vol. 9, pp. 12-22).

Surdyk, S., and S. Fujita, (1995), Microwave dielectric properties of snow: Modeling and

© 2015 American Geophysical Union. All rights reserved.

Accepted Article

measurements, Geophysical research letters, 22(8), 965-968.

Tabraham, J. (1998), The desalination of marine ice. (PhD thesis, University of Cambridge).

Takei, I. (2007). Dielectric relaxation of ice samples grown from vaporphase or liquid-phase water. In *Physics and Chemistry of Ice* (Vol. 1, p. 577).

Takei, I., and N. Maeno (1987), Electric characteristics of point defects in HCl-doped ice, Le Journal de Physique Colloques, 48(C1), C1-121.

Takei, I., and N. Maeno (1997), Dielectric low-frequency dispersion and crossover phenomena of HCl-doped ice. The Journal of Physical Chemistry B, 101(32), 6234-6236.

Taubenberger R. (1973), Physics and Chemistry of Ice, p. 187, (E. Whalley, Ed.), Roy. See, Canada.

Taylor, K. C., R. B. Alley, G. W. Lamorey, and P. Mayewski, (1997), Electrical measurements on the Greenland Ice Sheet Project 2 core, Journal of Geophysical Research: Oceans (1978–2012), 102(C12), 26511-26517.

Taylor, K., R. Alley, J. Fiacco, P. Grootes, G. Lamorey, P. A. Mayewski, and M. J. Spencer, (1992), Ice-core dating and chemistry by direct-current electrical conductivity, Journal of Glaciology, 38(130), 325.

Telford, W. M., and R. E. Sheriff, (1990), Applied geophysics (Vol. 1), Cambridge university press.

Thomas, D. N., and G. S Dieckmann (2009), Sea ice, John Wiley & Sons.

Thyssen, F. (1988), Special aspects of the central part of Filchner-Ronne Ice Shelf, Antarctica., Ann. Glaciol, 11, 173-179.

Tinga, W. R., WAG. Voss and DF. Blossey, (1973), Generalized approach to multiphase dielectric mixture theory, J Appl Phys 44, 3897–3902.

Tison, J. L., A. Khazendar and E. Roulin (2001), A two-phase approach to the simulation of the combined isotope/salinity signal of marine ice, Journal of Geophysical Research: Oceans (1978–2012), 106(C12), 31387-31401.

Tobie, G., B. Giese, T. A. Hurford, R. M. Lopes, F. Nimmo, F. Postberg, K. D. Retherford, J.

© 2015 American Geophysical Union. All rights reserved.

Accepted Article

Schmidt, J. R. Spencer, T. Tokano, and E. P. Turtle (2010), Surface, Subsurface and Atmosphere Exchanges on the Satellites of the Outer Solar System, Space Sci. Rev., 153(1-4), 375-410, doi:10.1007/s11214-010-9641-3.

Tonkonogov, M. P. (1998), Dielectric spectroscopy of hydrogen-bonded crystals, and proton relaxation, Physics-Uspekhi, 41(1), 25.

Treverrow, A., R. C. Warner, W. F. Budd, and M. Craven, (2010), Meteoric and marine ice crystal orientation fabrics from the Amery Ice Shelf, East Antarctica, Journal of Glaciology, 56(199), 877-890.

Vant, M. R., R. O. Ramseier, and V. Makios, (1978), The complex-dielectric constant of sea ice at frequencies in the range 0.1–40 GHz, Journal of Applied Physics, 49(3), 1264-1280.

von Hippel A., (1971), Transfers of protons through "Pure" ice Ih single crystals. II. Molecular models for polarization and conduction, Journal of Chemical Physics, 54, 145.

von Hippel A., 1988, The dielectric relaxation spectra of water, ice and aqueous solutions and their interpretation. 3. Proton organization and proton transfer in ice, IEEE Transaction on Electrical Insulation, 23, 5.

von Hippel A., D.B. Knoll and W.B. Westphal (1971), Transfers of protons through "Pure" ice Ih single crystals. I. Polarization spectra of ice Ih, Journal of Chemical Physics, 54, 134.

von Hippel, A. R. (1954), Dielectric Materials and Applications. Papers by 22 Contributors. New York.

Voronkov, A. A. (1958), The piezoelectric, elastic and dielectric properties of crystals of MgSO4.7H2O. Soviet Physics: Crystallography, 3, 722-725.

Waite, A. H., and S. J. Schmidt (1962), Gross errors in height indication from pulsed radar altimeters operating over thick ice or snow, Proceedings of the IRE, 50(6), 1515-1520.

Walker C. C., and B. E. Schmidt (2015), Ice collapse over trapped water bodies on Enceladus and Europa, Geophysical Research Letters.

Warren, S. G. (1984), Optical constants of ice from the ultraviolet to the microwave, Applied optics, 23(8), 1206-1225.

© 2015 American Geophysical Union. All rights reserved.

Accepted Article

Warren, S. G., and R. E. Brandt (2008), Optical constants of ice from the ultraviolet to the microwave: A revised compilation, Journal of Geophysical Research: Atmospheres (1984–2012), 113(D14).

Wettlaufer, J. S., and Worster, M. G. (2006), Premelting dynamics. Annu. Rev. Fluid Mech., 38, 427-452.

Wilhelms, F., J. Kipfstuhl, H. Miller, K. Heinloth, and J. Firestone (1998), Precise dielectric profiling of ice cores: a new device with improved guarding and its theory, Journal of Glaciology, 44(146), 171-174.

Williams, K. K., and R. Greeley (1998), Estimates of ice thickness in the Conamara Chaos region of Europa, Geophysical research letters, 25(23), 4273-4276.

Wolff, E. W., Moore, J. C. Clausen, H. B., Hammer, C. U., Kipfstuhl, J., and K. Fuhrer, (1995), Long-term changes in the acid and salt concentrations of the Greenland Ice Core Project ice core from electrical stratigraphy, Journal of Geophysical Research: Atmospheres (1984–2012), 100(D8), 16249-16263.

Wolff, E. W., W. D. Miners, J. C. Moore, and J. G. Paren, (1997), Factors Controlling the Electrical Conductivity of Ice from the Polar Regions A Summary. *The Journal of Physical Chemistry B*, *101*(32), 6090-6094.

Wolff, E.W. (2000), Electrical stratigraphy of polar ice cores: principles, methods, Geophys. Res, 100, 1933.

Worz, O., and R. H. Cole (1969), Dielectric properties of ice I, The Journal of Chemical Physics, 51(4), 1546-1551.

Young, K. F., and Frederikse, H. P. R. (1973). Compilation of the static dielectric constant of inorganic solids. *Journal of Physical and Chemical Reference Data*, *2*(2), 313-410.

Zhang, H. (2003), Internal structure models and dynamical parameters of the Galilean satellites, Celestial Mechanics and Dynamical Astronomy, 87, 189-195.

Zhang, Z., T. Hagfors, E. Nielsen, G. Picardi, A. Mesdea, J. J. Plaut (2008), Dielectric properties of the Martian south polar layered deposits: MARSIS data inversion using Bayesian inference and genetic algorithm, Journal of Geophysical Research (Planets) 113,

© 2015 American Geophysical Union. All rights reserved.

Accepted Article

5004.

Zimmer, C., K. K. Khurana, and M. G. Kivelson (2000), Subsurface oceans on Europa and Callisto: Constraints from Galileo magnetometer observations, Icarus, 147(2), 329-347.

Zotikov, I. A., V. S. Zagorodnov, J. V. Raikovsky (1980), Core drilling through the Ross Ice Shelf (Antarctica) confirmed basal freezing, Science, 207, 1463-5.

Accepted Article

© 2015 American Geophysical Union. All rights reserved.

Table 1 Major compounds identified on the three icy Galilean satellites, and those predicted by models or experiments.

Satellite	Range of measured temperatures	Known Compounds	Predicted Compounds
Europa	86-132 K	H_2O, SO_2, CO_2, H_2O_2, O_2, hydrates of H_2SO_4, $MgSO_4$ and Na_2SO_4	heavily hydrated and/or hydroxylated minerals, tholins
Ganymede	90-160 K	H_2O, SO_2, CO_2, O_2, O_3	Ammonia, aliphatic hydrocarbons, heavily hydrated and/or hydroxylated minerals, tholins
Callisto	80-158 K	H_2O, SO_2, CO_2, O_2, silicates	Ammonia, aliphatic hydrocarbons, heavily hydrated and/or hydroxylated minerals, tholins

[a]Table adapted from *Dalton* [2010], data taken from *Carlson et al*. [1996, 2005, 2009], *Dalton* [2007], *Hanel et al*. [1979], *Hibbits et al*. [2000], *Moore et al*. [2007], *Orton et al*. [1996], *Roush* [2001], *Spencer et al*. [1999].

Accepted Article

© 2015 American Geophysical Union. All rights reserved.

Table 2 Salinity of marine ice melt-water[a]

Location	Salinity ‰	Thickness (m)	Reference
Ronne Ice Shelf	0.02-0.1	170	*Eiken et al*. [1994]
Amery Ice Shelf	0.05-0.1	160	*Morgan* [1972]
Hell's Gate Ice Shelf	0.01-2	35-80	*Baroni* [1988]; *Souchez et al*. [1991]
Ross Ice Shelf	2-4	6	*Zotikov et al*. [1980]
Koettlitz Ice Tongue	0.2-5.3	9- 15	*Cow and Epstein* [1972]
Ward Hunt Ice Shelf	0.3-15.3	25	*Jeffries* [1991]
Hells Gate Ice Shelf	0.03 – 0.3	10- 45	*Tison et al*. [1998]
Nansen Ice Shelf	0.035 - 0.10	45	*Khazendar et al*. [2001]
Amery Ice Shelf	0.03 - 0.53	203	*Craven et al*. [2009]
Roi Baudouin Ice Shelf	0.1 – 0.9	5-66	*Hubbard et al*. [2012]
Multi-year sea ice	2-5	2.5-5	*Weeks and Ackley* [1986]

[a] (modified from *Eicken et al*. [1994]).

Accepted Article

© 2015 American Geophysical Union. All rights reserved.

Table 3 Parameters for water ice protonic point defects at 253 K[a]

Defect type	e_i (1.609×10^{-19} C)	Intrinsic concentration n_i/N	μ_i at 253 K (10^{-8} m^2 V^{-1} s^{-1})	$\frac{1}{2}E_i^F + E_i^M$ [b] (eV)
H_3O^+	0.62	$\leq 10^{-13}$	10	>0.7
OH^-	-0.62	$\leq 10^{-13}$	3	?
intrinsic L	0.38	10^{-7}	2	0.58

[a] Values taken from *Petrenko and Withworth* [1999]

[b] Activation energies for formation and motion (see text)

Accepted Article

© 2015 American Geophysical Union. All rights reserved.

Table 4 Characteristics of the experimental setup used to measure the dielectric properties of pure water ice

Ice type	Measurement frequency	Temperature	Measuring techniques	Critical aspects	Reference
Ih Polycrystalline	50Hz-70kHz	218K-273K	Bridge/transient method	Crack and ice/electrode contact	Auty & Cole (1952)
Ih Polycrystalline	0.045kHz-300kHz	249.6K	Bridge method	Effect of pressure	Chan (1965)
Ih Polycrystalline	1Hz-1kHz	83K-273K	Bridge method	Presence of unexpected impurities	Ida et al. (1966)
Ih Polycrystalline	50kHz-200kHz 0.05Hz-1kHz	193K-273K	Bridge method	Hysteresis in the thermal cycle/Cracks	Cole & Worz (1969)
Ic and Ih Polycrystalline	0.02Hz-500kHz	153K-273K	Bridge method	Ice growth and phase transitions	Gough & Davidson (1970)
Ih single-crystal	0.008Hz-100kHz	93K-273K	Bridge method	Unexpected impurities and space charge	von Hippel et al. (1971)
Ih single-crystal	1mHz-10kHz	123K-273K	Bridge/ loop method	Anisotropy/Presence of unexpected impurities	Kawada (1978)
Hoar-frost ice crystal	20Hz-100kHz	253K	Bridge method	Mercury electrode/dislocation effects	Itagaki (1978)
Ih Polycrystalline	0.1Hz-10kHz	133K-272K	Bridge/transient method	Impure ice/high pressure	Johari & Whalley (1981)
Ih single-crystal	20-100 kHz	264.6K/270.5K/259K	Bridge method	Copper electrodes/Aging effects	Camp (1983)
Amorphous-polycrystalline	At 1kHz and 10kHz	80K-253K	Bridge method	Amorphous vs. crystalline	Johari (1991)
Ih single-crystal	1mH-10kHz	123K-263K	Bridge/ loop method	Anisotropy	Takei & Maeno (1987)

Accepted Article

© 2015 American Geophysical Union. All rights reserved.

Table 5 Parameters (A, B, C) based on interpolation between low frequencies data and microwave data*.

Temperature (K)	A ($\times 10^4$)	B ($\times 10^5$)	C
190	0.005	1.537	1.175
200	0.010	1.747	1.168
220	0.031	2.469	1.129
240	0.268	3.495	1.088
248	0.635	4.006	1.073
253	1.059	4.380	1.062
258	1.728	4.696	1.056
263	2.769	5.277	1.038
265	3.326	5.646	1.024

*** Data were compiled by *Fujita et al*. [2000].**

Accepted Article

© 2015 American Geophysical Union. All rights reserved.

Table 6 Dielectric properties of different type of clathrate hydrates after *Davidson* [1973] and *Davidson and Ripmeester* [1978]. The reference temperature is ~233 K when not specified.

Material	Clathrate type	Relaxation frequency (kHz)	Activation energy (eV)	ε_s	ε_∞
Ice Ih	-	0.11	0.575	107	3.1
Argon	Type II	1.66	0.247	62	2.85
Nitrogen	Type II	0.88	0.343	61	2.85
Acetone	Type II	279.22	0.282	70 (236 K)*	8.6(168 K)*
Ethylene oxide	Type I	482.29	0.334	62	7.7
Cyclopropane	Type I	0.51	0.494	53	2.9
Trimethylene oxide	Type II	331.57	0.303	65	5.63
Tetrahydrofuran	Type II	159.15	0.309	67	5.06

*Taken from *Suga et al*. [1993].

Accepted Article

© 2015 American Geophysical Union. All rights reserved.

Table 7 Crystal structure, molecular weights and density of $MgSO_4$ and Na_2SO_4 stable hydrates

Sulfate hydrates	*Natural Mineral*	*Crystal structure*	*Molecular Weight (g/mol)*	*Density (g/cm^3)*
$MgSO_4$	-	ortho-rhombic	120.37	2.66
$MgSO_4 \cdot 1H_2O$	Kieserite	monoclinic	138.38	2.57
$MgSO_4 \cdot 6H_2O$	Hexahydrate	monoclinic	228.46	1.76
$MgSO_4 \cdot 7H_2O$	Epsomite	ortho-rhombic	246.47	1.67
$MgSO_4 \cdot 11H_2O$	Meridianite	triclinic	318.54	1.51
Na_2SO_4	Thenardite	ortho-rhombic	142.04	2.66
$Na_2SO_4 \cdot 7H_2O$	Heptahydrate	(unknown)	268.15	(unknown)
$Na_2SO_4 \cdot 10H_2O$	Mirabilite	monoclinic	322.19	1.46

Accepted Article

© 2015 American Geophysical Union. All rights reserved.

Table 8 Comparison between CO_2 ice dielectric properties estimated in two different experiments

	***Pettinelli et al*. [2003]** **TDR (500-1000 MHz)**		***Simpson et al*. [1980]** **Microwave (2.2-12 GHz)**	
Material	**Density (g cm^{-3})**	**ε_a*± $\Delta\varepsilon_a$**	**Density (g cm^{-3})**	**$\varepsilon_a \pm \Delta\varepsilon_a$**
CO_2 ice	1.50	2.12 ± 0.04	1.56 (literature)	2.25 (estimated)
CO_2 snow	---	1.48 ± 0.04	---	---
CO_2 powder(1)	0.99	1.67 ± 0.06	0.95	1.74 ± 0.04
CO_2 powder(2)	1.01	1.63 ± 0.06	1.02	1.73 ± 0.04
CO_2 powder(3)	1.02	1.67 ± 0.06	1.06	1.80 ± 0.04

*** Apparent permittivity (see Appendix 1).**

Accepted Article

© 2015 American Geophysical Union. All rights reserved.

Table 9 Permittivity, velocity and vertical resolution in various types of ice. Vertical resolution has been computed for RIME and Europa Clipper radars.

Material	ε'	v (m/μs)	Δz (m) (Δf = 1MHz)	Δz (m) (Δf = 3MHz)	Δz (m) (Δf =10MHz)	Reference
Pure ice	3,1	170,4	170,4	56,8	17,0	**Petrenko & Witworth [1999]**
Dirty ice	3,5	160,4	160,4	53,5	16,0	**Mattei et al. [2014]**
Nonpolar clathrate (Cyclopropane)	2,9	176,2	176,2	58,7	17,6	**Davidson [1973]**
Polar clathrate (Trimethylene oxide)	5,6	126,4	126,4	42,1	12,6	**Davidson [1973]**
CO_2	2,1	206,0	206,0	68,7	20,6	**Pettinelli et al. [2003]**
$MgSO_4 \cdot 11H_2O$ eutectic mixture	3,8	153,7	153,7	51,2	15,4	**Clausius-Mosotti formula**
$Na_2SO_4 \cdot 10H_2O$ eutectic mixture	3,2	166,9	166,9	55,6	16,7	**Young & Frederikse [1973]**
NH_3 ice	3,4	163,2	163,2	54,4	16,3	**Smyth & Hitchcok [1934]**

Accepted Article

© 2015 American Geophysical Union. All rights reserved.

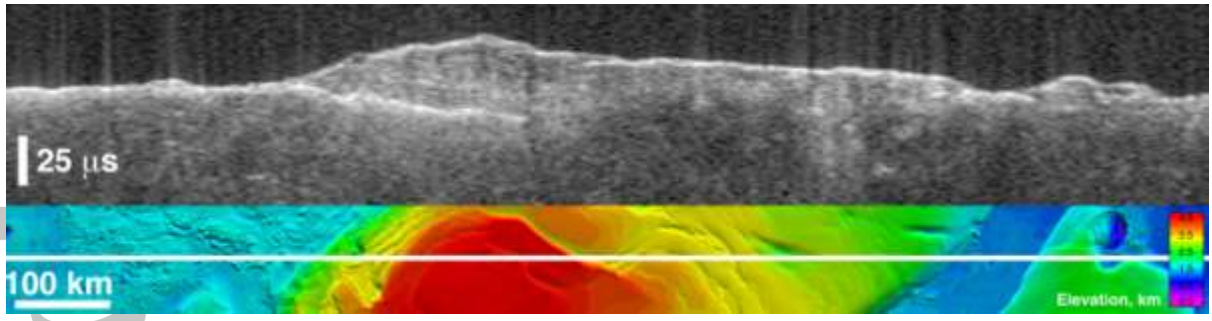

Figure 1 (Top) A radargram of the reflected echo power measured by MARSIS [*Picardi et al*., 2005] over Planum Australe, Mars, showing a bright basal reflector beneath the ice-rich South Polar Layered Deposits. A radargram is a representation of radar echoes acquired continuously during the movement of the radar as a grey-scale image, in which the horizontal dimension is distance along the ground track, the vertical dimension is the round trip time of the echo, and the brightness of the pixel is a function of the strength of the echo. The apparent curvature of the reflector is an artifact of the time representation of the data. The maximum depth at which the basal reflector could be detected, converting travel time to depth based on propagation through water ice, is about 3.5 km. (Bottom) Ground track of the spacecraft during data acquisition, shown on a shaded relief topographic map of the south polar region of Mars (taken from *Plaut et al*. [2007]).

Accepted Article

© 2015 American Geophysical Union. All rights reserved.

Accepted Article

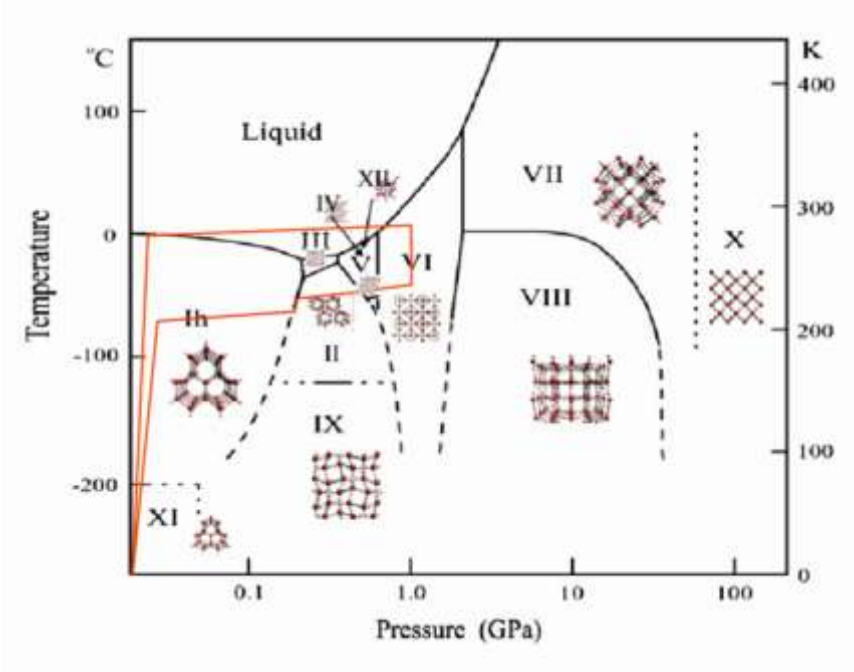

Figure 2 right

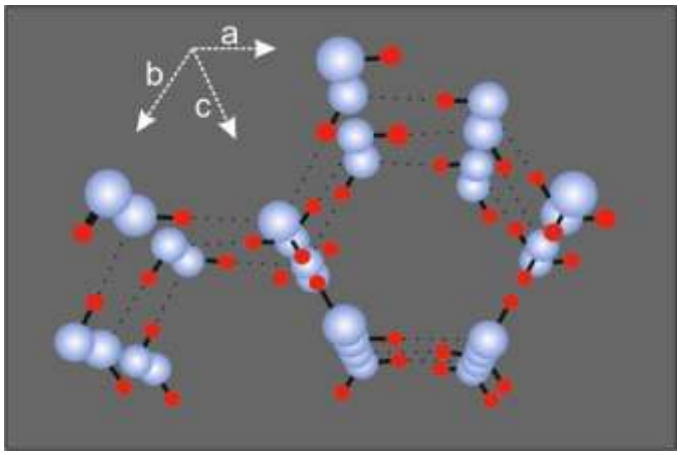

Figure 2 left

Figure 2 (Left) Solid-liquid phase diagram showing the different water ice phases and relevant lattice structures. Solid lines represent experimental data whereas dashed lines are extrapolated or inferred phase boundaries (taken from *Bartels-Rausch et al.* [2012]). The area delimited by the red line indicates the range of plausible values of pressure and temperature on the jovian icy moons. (Right) Ice Ih crystalline structure with the c-axis (optical axis) normal to the hexagonal rings. Blue spheres are oxygen atoms and red spheres are hydrogen atoms.

© 2015 American Geophysical Union. All rights reserved.

Accepted Article

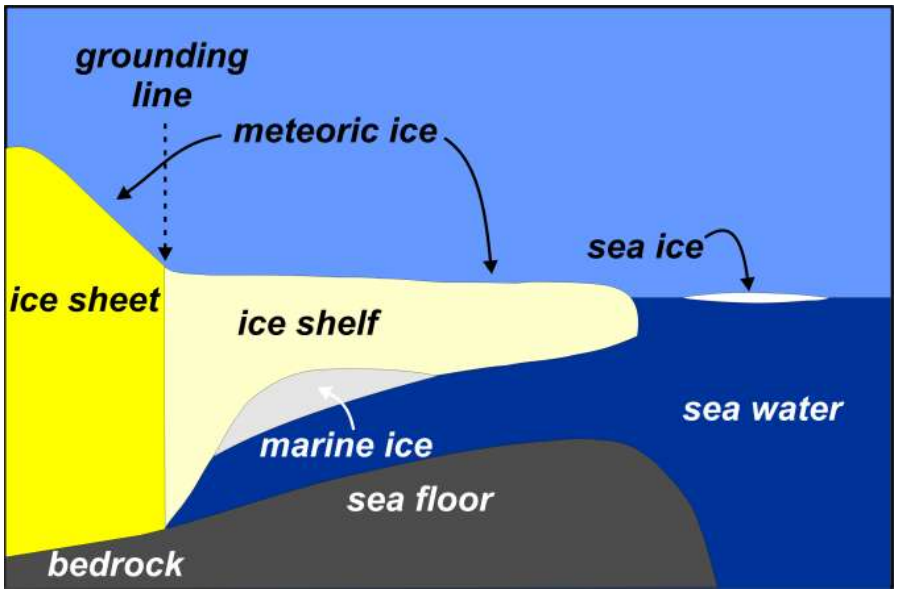

Figure 3 Schematic of the location of the different terrestrial ice bodies.

© 2015 American Geophysical Union. All rights reserved.

Accepted Article

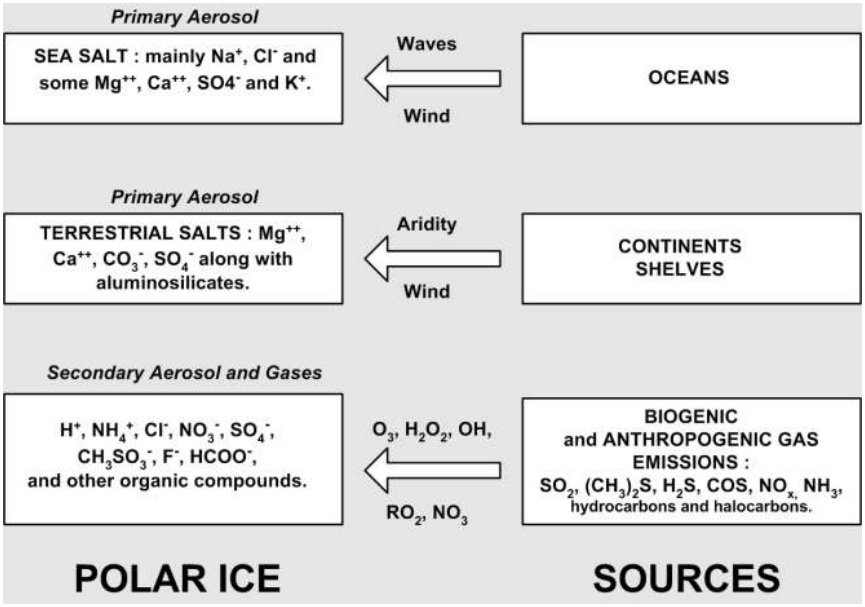

Figure 4 Scheme of the different soluble impurities expected to be found in polar ice and relevant sources (modified from Legrand and Mayewski [1997])

© 2015 American Geophysical Union. All rights reserved.

Accepted Article

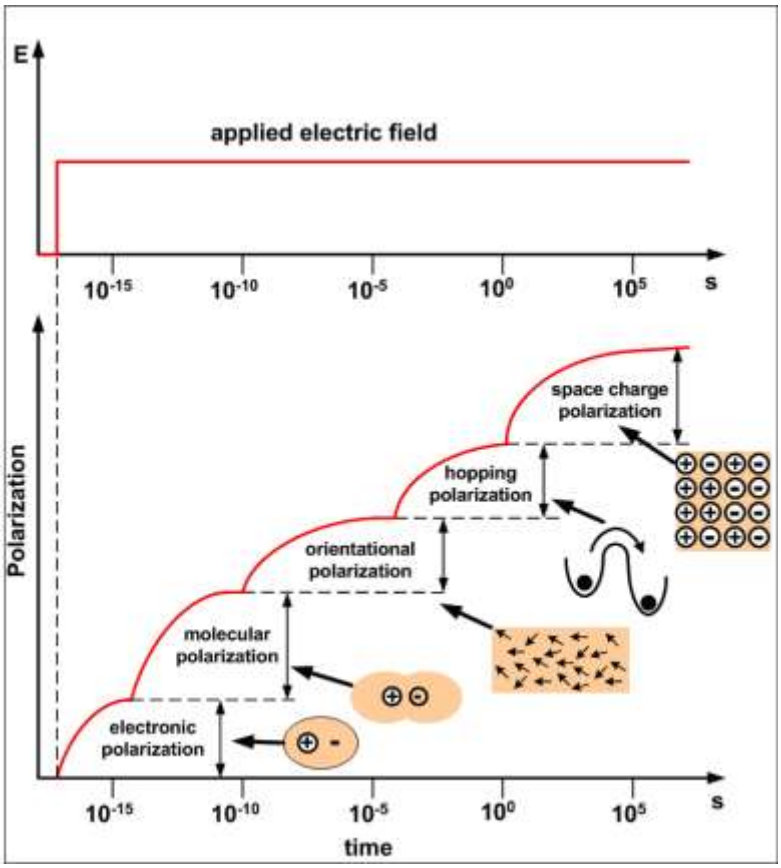

Figure 5 Total polarization time response of a generic material to a step function electric field [modified after *Kao*, 2004]

© 2015 American Geophysical Union. All rights reserved.

Accepted Article

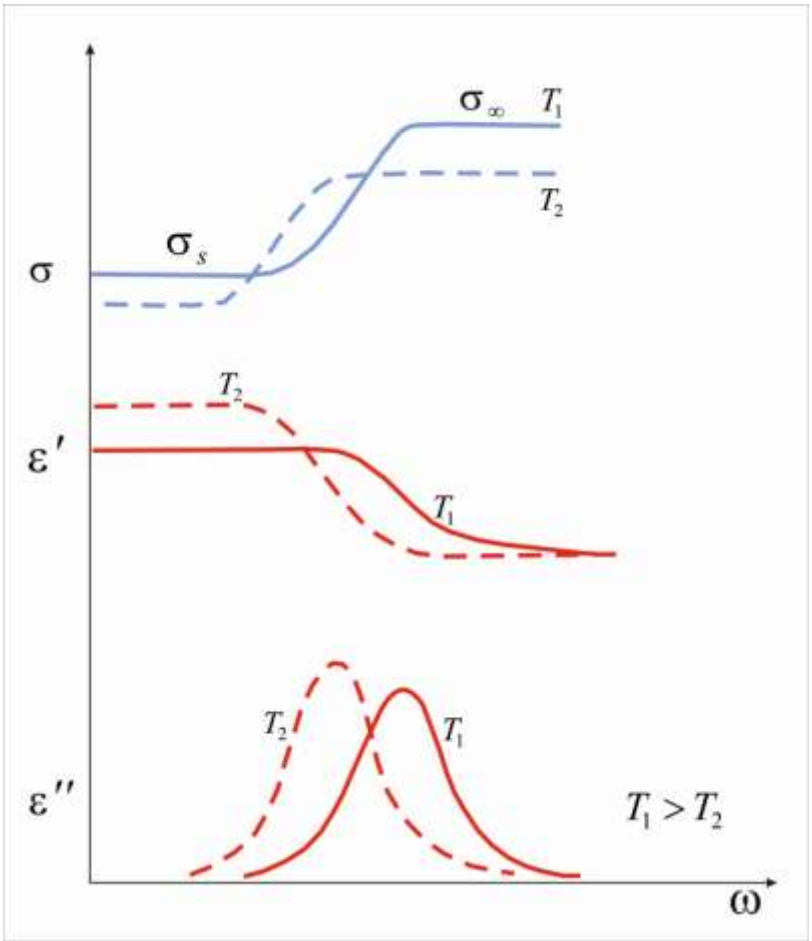

Figure 6 Sketch of the complex permittivity, loss tangent and effective conductivity as a function of frequency for a generic material.

© 2015 American Geophysical Union. All rights reserved.

Accepted Article

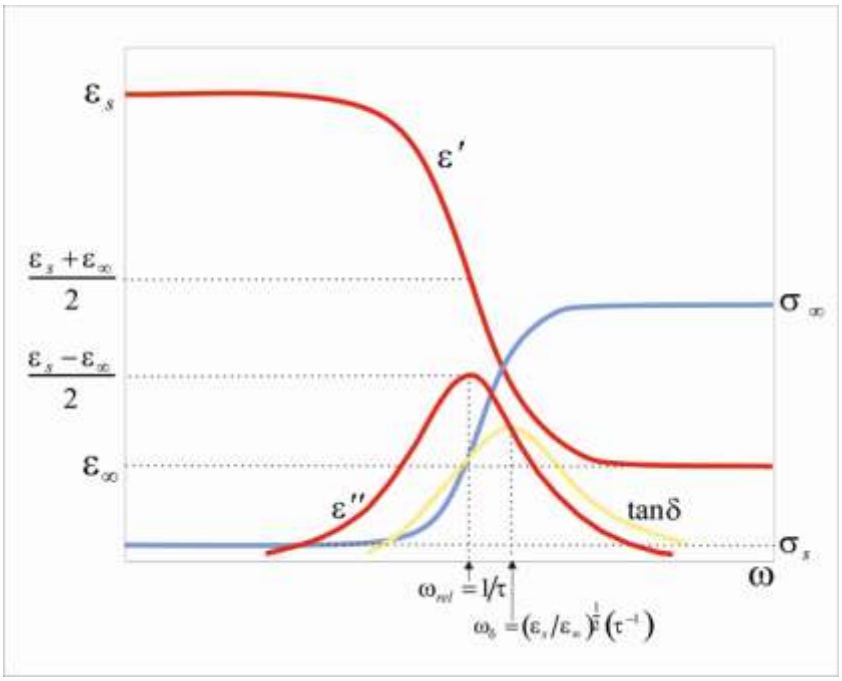

Figure 7 Effect of the temperature on the dielectric behavior of a generic material. For decreasing temperatures the conductivity decreases (top), the real part of permittivity increases (middle), and the peak of the imaginary part shifts towards lower frequencies (bottom).

© 2015 American Geophysical Union. All rights reserved.

Accepted Article

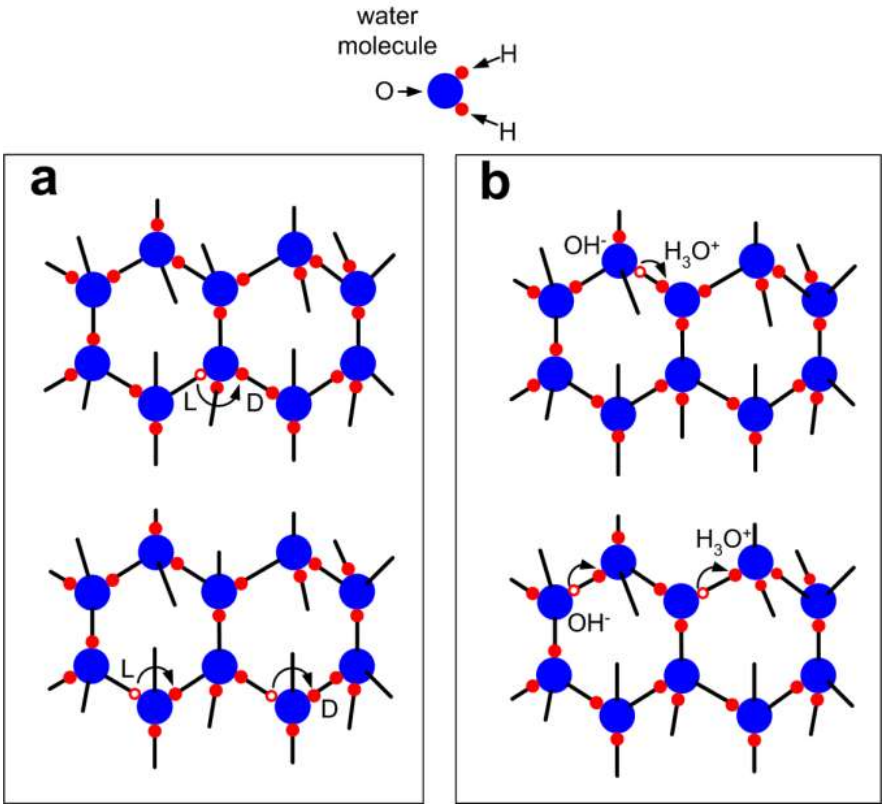

Figure 8 Intrinsic defects and associated protonic motions for L-D defects (a) and ionic defects (b).

© 2015 American Geophysical Union. All rights reserved.

Accepted Article

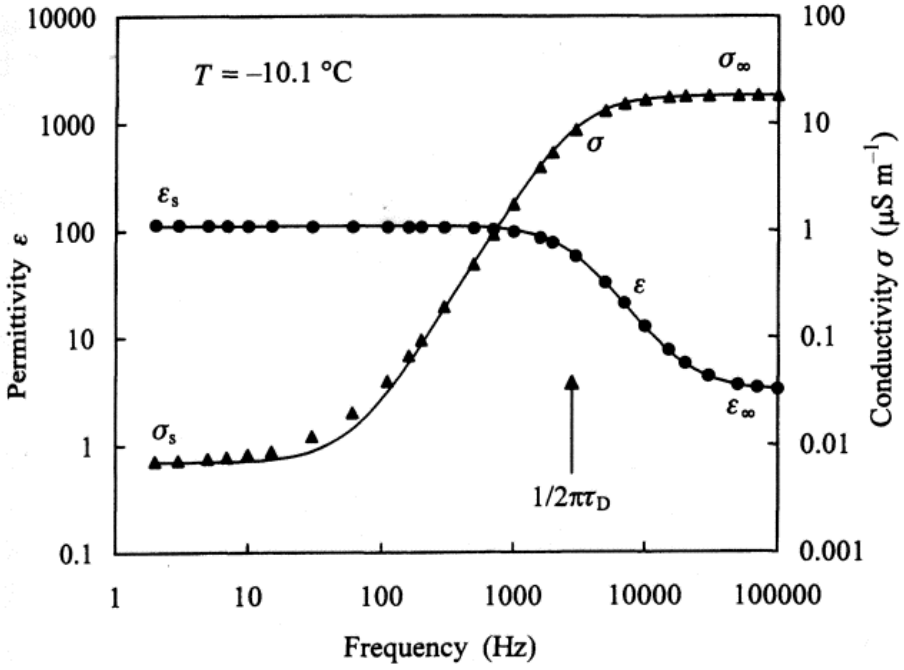

Figure 9 Real part of permittivity and conductivity as a function of frequency (2 Hz-100 kHz) of a single crystal of pure water ice measured at 263 K (*Takei and Maeno* [1997] modified by *Petrenko and Whitworth* [1999]).

© 2015 American Geophysical Union. All rights reserved.

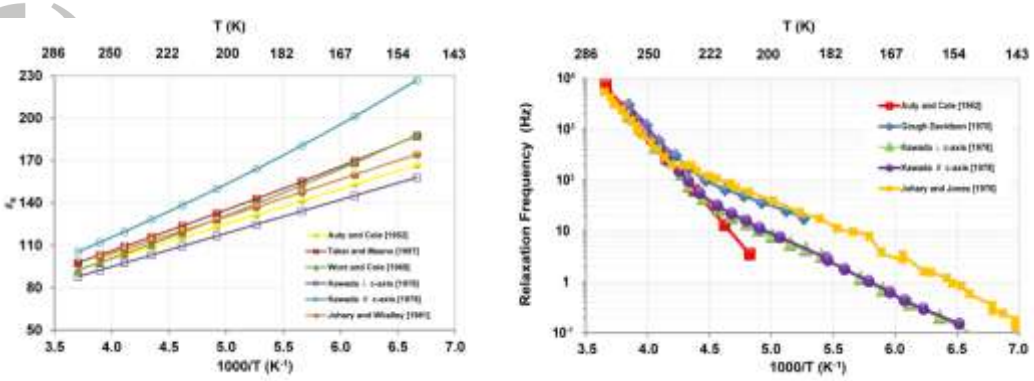

Figure 10 (Left) Trend of ε_s vs. temperature plotted using the parameters estimated by different authors (see legend) to fit their experimental data; (Right) relaxation frequency (ν_{rel}) vs. temperature measured by different authors (see legend). Note that only the Auty and Cole data do not show a change in slope below 230 K. In both panels, the Kawada data refer to measurements performed parallel and normal to the ice c-axis.

Accepted Article

© 2015 American Geophysical Union. All rights reserved.

Accepted Article

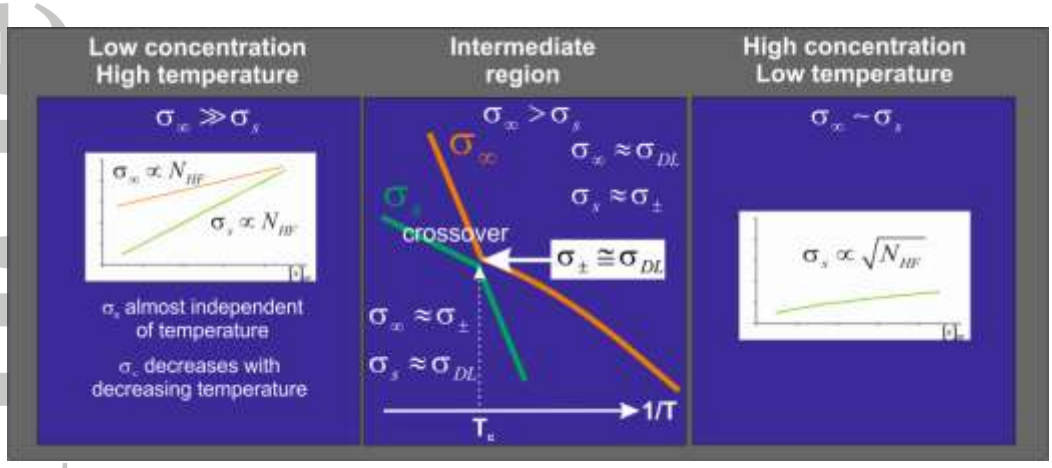

Figure 11 Summary of the dielectric properties of HF doped ice for different concentrations and temperature ranges. The orange curve refers to σ_∞ and the green curve to σ_s. In the low concentration and high temperature range (left panel) the high frequency conductivity is much larger than the static conductivity; in the intermediate region (central panel) σ_∞ is still larger than σ_s, except at the crossover temperature, where $\varepsilon_s - \varepsilon_\infty = 0$ ($\sigma_{DL} \cong \sigma_\pm$), and the ice behaves as a pure conductor. In the high concentration and low temperature regime (right panel) the high and low frequency conductivity are of the same order of magnitude and the trend of σ_s vs concentration becomes non-linear.

© 2015 American Geophysical Union. All rights reserved.

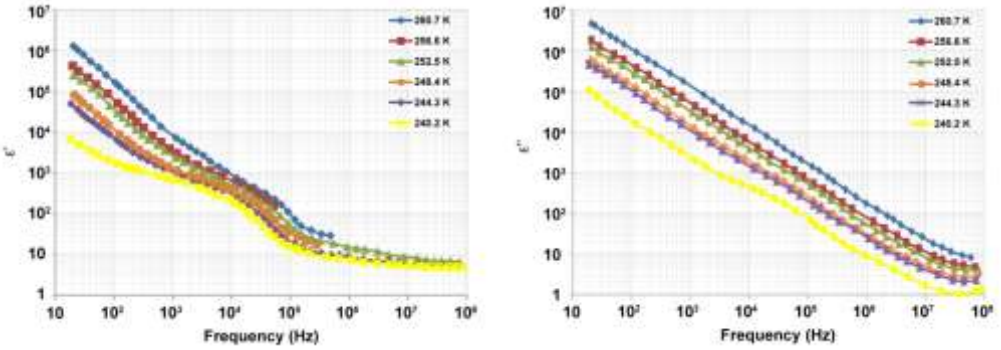

Figure 12 Real (left panel) and imaginary (right panel) parts of the dielectric permittivity of artificial sea ice (salinity $5.12‰$) as a function of frequency, from about 260 K to 240 K (modified from *Addison* [1969]). In the left panel (ε'), the dispersion due to ion migration is visible below 10 kHz and the Debye relaxation between 10 kHz and 100 kHz. In the right panel (ε'') a third relaxation is recognizable above 10 MHz.

Accepted Article

© 2015 American Geophysical Union. All rights reserved.

Accepted Article

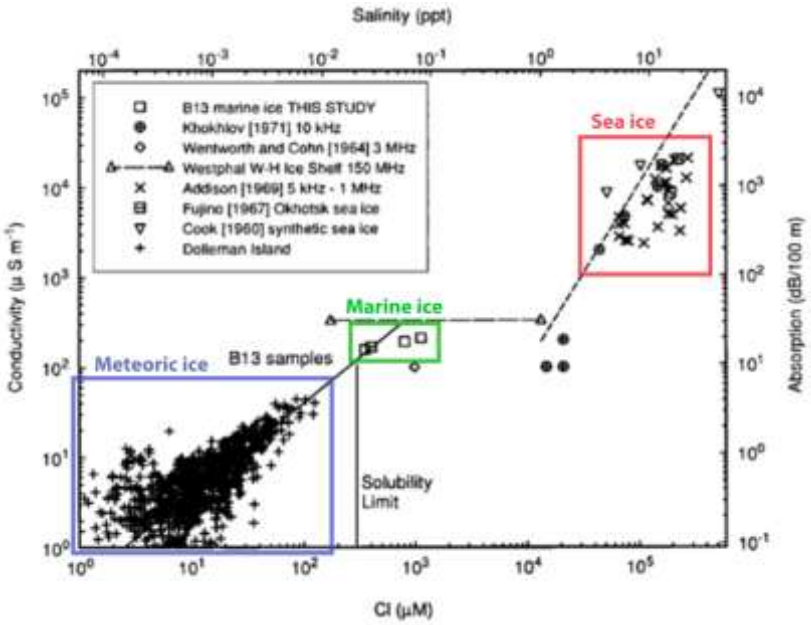

Figure 13 Logarithmic plot of conductivity versus Cl concentration (salinity) at 251 K for samples of meteoric (blue box), marine (green box) and sea ice (red box) (taken from *Moore et al.* [1994]).The figure illustrates that meteoric and sea ice data have different dielectric behaviors, as shown by two distinct linear regressions (solid and dashed lines).

© 2015 American Geophysical Union. All rights reserved.

Accepted Article

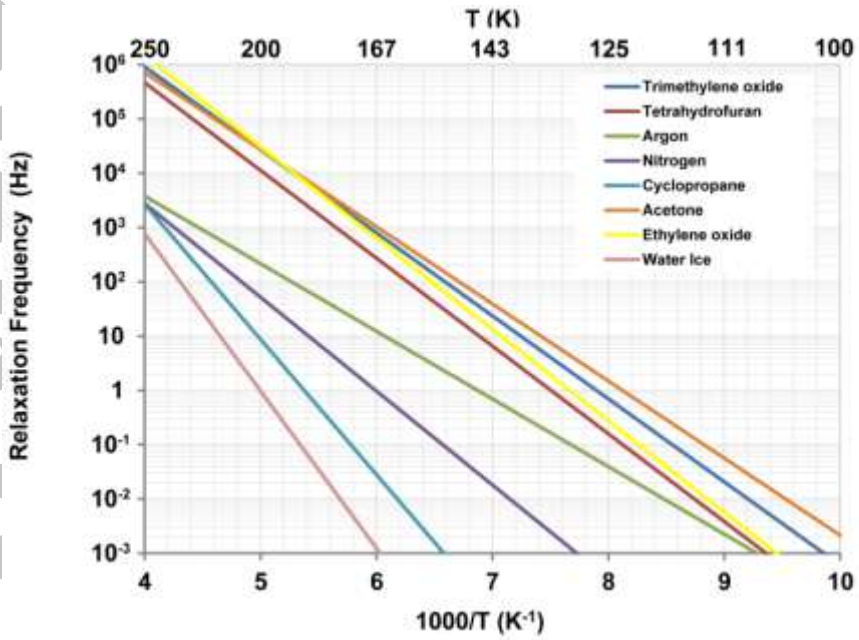

Figure 14 Relaxation frequencies of some clathrate hydrates and pure water ice as a function of temperature, extrapolated from Table 6. The comparison of the various curves shows that the relaxation frequencies of these compounds are always higher than that of pure water ice and that such differences increase with decreasing temperatures. The legend indicates the guest molecules (cf. Table 6).

© 2015 American Geophysical Union. All rights reserved.

Accepted Article

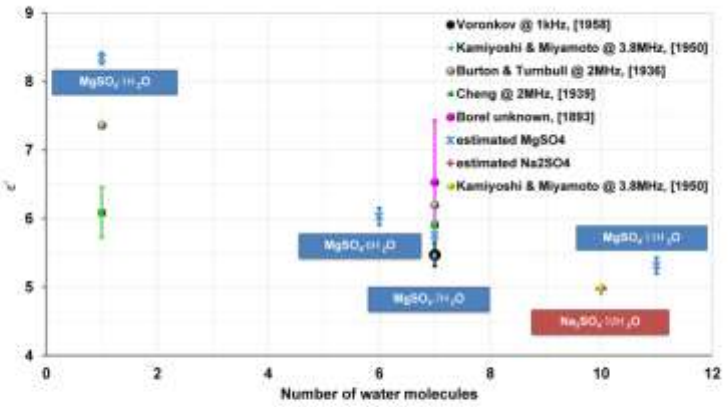

Figure 15 Plot showing the real part of permittivity of different magnesium and sodium sulfate hydrates estimated using Equation (20) (dark blue magnesium, burgundy sodium) together with the experimental values available in the literature. The uncertainties on the predicted data have been calculated using the error propagation formula applied to Equation (20), while those for the experimental data are the values reported (when given) by the authors.

© 2015 American Geophysical Union. All rights reserved.

Accepted Article

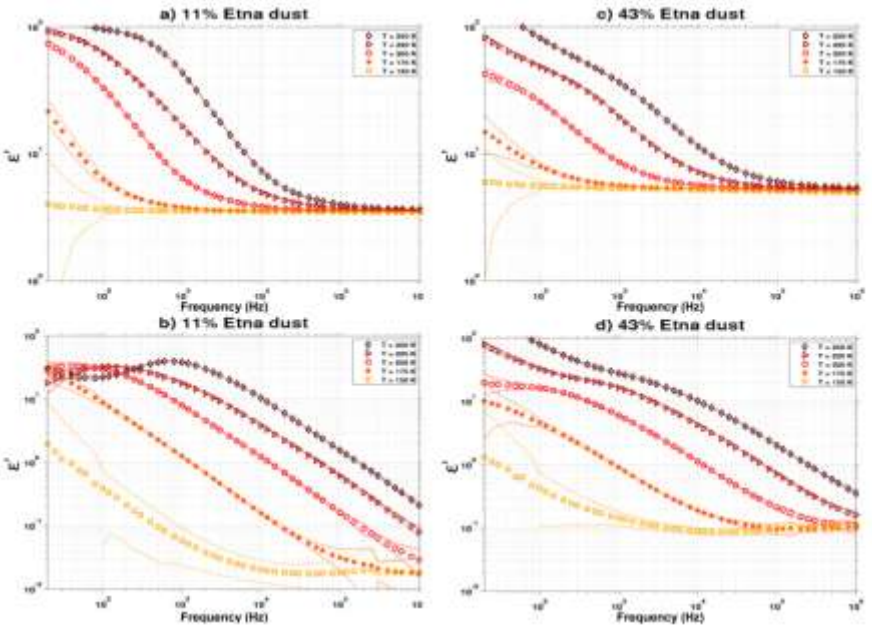

Figure 16 Electromagnetic properties measured on two ice/grains mixtures at different temperatures. Panels a and c show the real part of permittivity and panels b and d the imaginary part of permittivity. The dashed lines represent the data uncertainties indicating the envelope of the error bars. Note that they are only visible if larger than 1% (modified from Mattei et al. 2014).

© 2015 American Geophysical Union. All rights reserved.

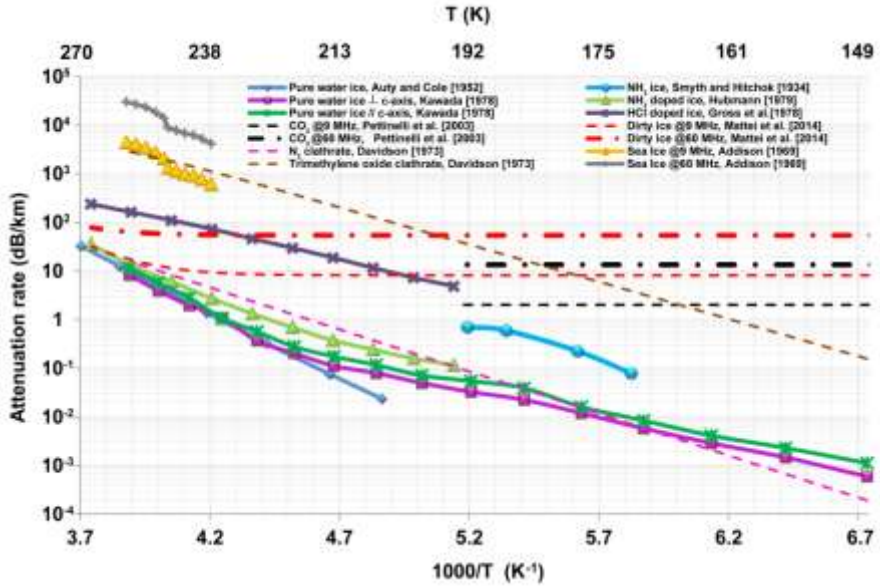

Figure 17 Attenuation rate vs. 1/T estimated at 9 MHz and 60 MHz for different types of ice using Equation 6 and the data available in the literature. If not specifically indicated in the legend, the curves at 9 MHz and 60 MHz coincide.

Accepted Article

© 2015 American Geophysical Union. All rights reserved.

Accepted Article

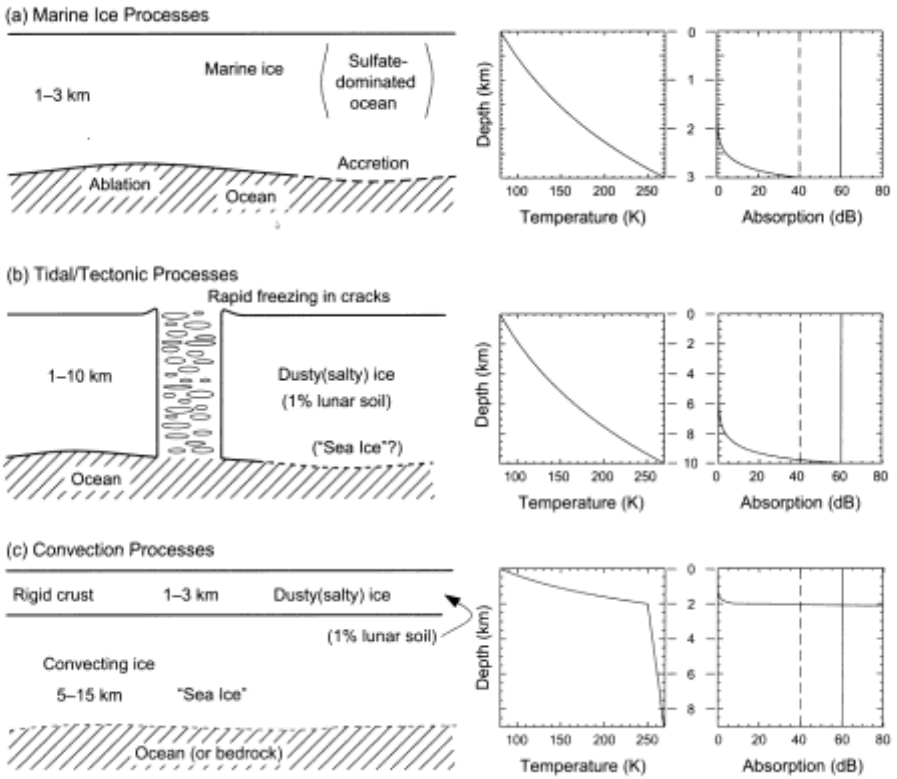

Figure 18 Europa icy crust models proposed by *Moore* [2000] (left) and relevant radar signal absorption vs. depth (right) [taken from *Blankenship et al.*, 2009]. a) Conductive ice shell similar to terrestrial marine ice; b) icy crust subjected to tectonic process with extrusions of molten material; c) convective ice shell below a thin rigid stagnant lid. Dashed and solid lines in right panels represent the expected signal to noise ratio for the jovian and anti-jovian sides.

© 2015 American Geophysical Union. All rights reserved.

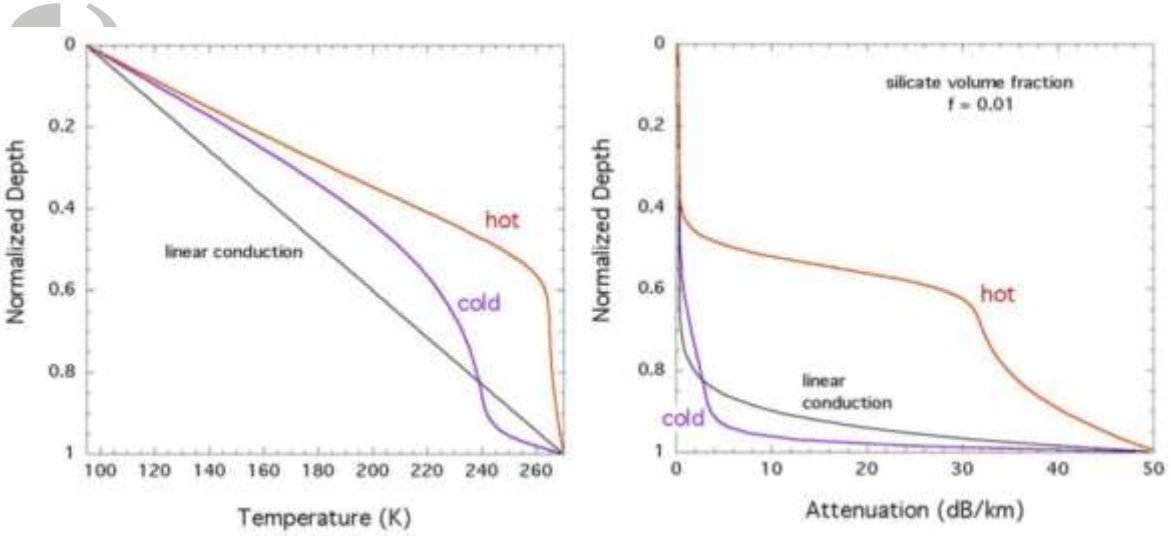

Figure 19 Thermal profiles (left) and radar signal attenuation at 50 MHz (right) in the cold/hot convective plumes for the europan crust (taken from *McKinnon* [2005]).

Accepted Article

© 2015 American Geophysical Union. All rights reserved.

Accepted Article

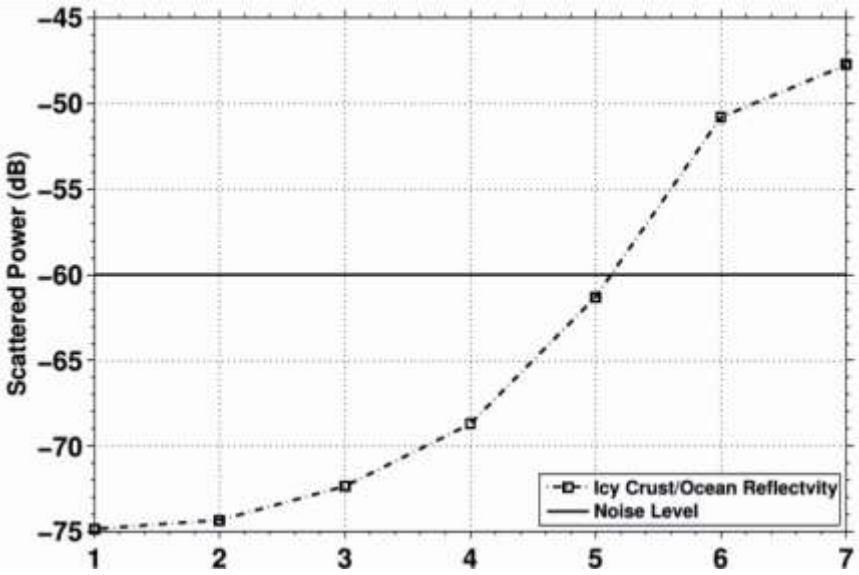

Figure 20 Power reflected by the ice/ocean interface located at 10 km depth in the Europa crust, considering seven different thermal profiles [*Di Paolo et al.*, 2014].

© 2015 American Geophysical Union. All rights reserved.

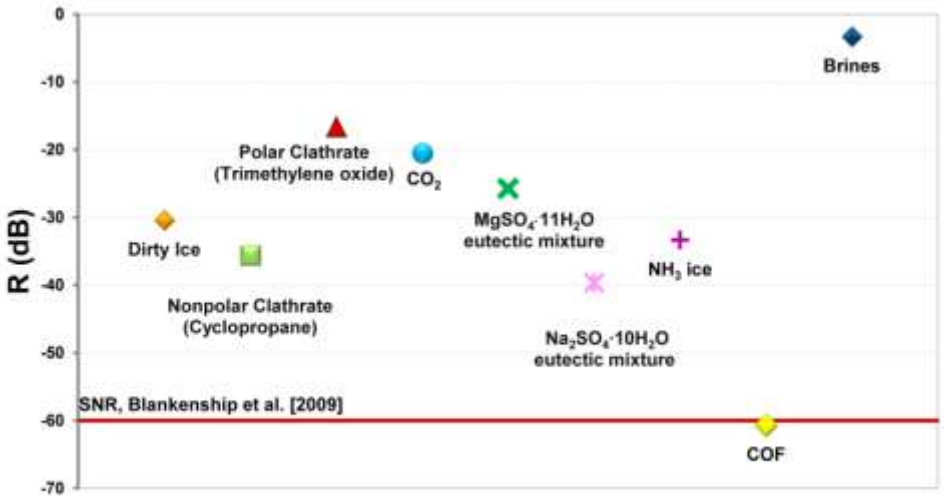

Figure 21 Reflection coefficient, expressed in dB, between pure water ice and different materials supposed to be present on the Galilean icy satellite crusts.

Accepted Article

© 2015 American Geophysical Union. All rights reserved.

Accepted Article

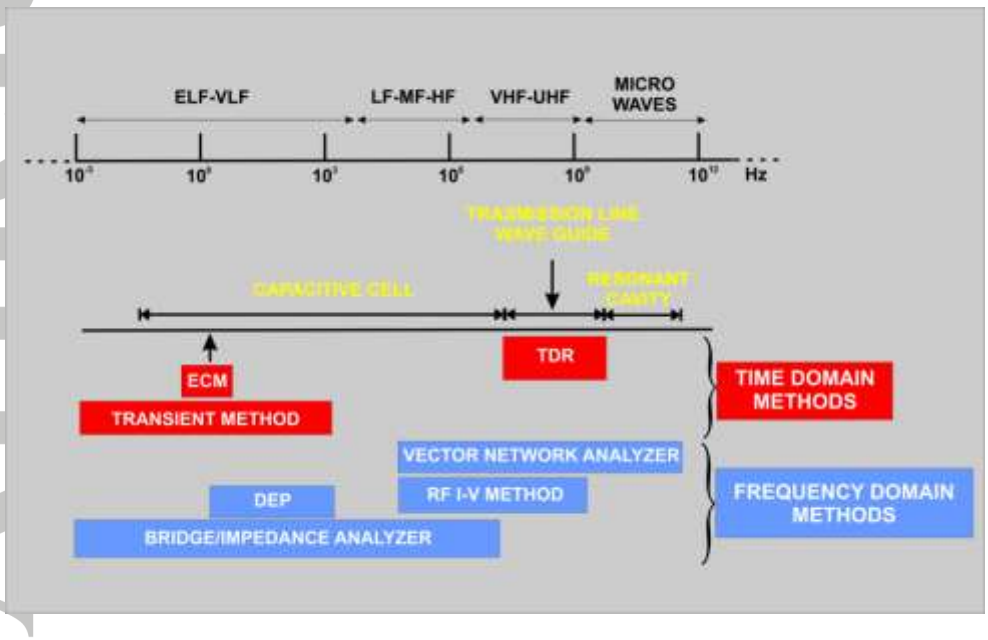

Figure A1

Figure a Dielectric measurement methods in the electromagnetic spectrum (not in scale)

© 2015 American Geophysical Union. All rights reserved.